Data: Author (Year) Title. URI [dataset]

University of Southampton

Faculty of Engineering and Physical Sciences

Optoelectronics Research Centre

Pico- and Nanophotonics of Reconfigurable Metamaterials

by

Jinxiang Li

Thesis for the degree of Doctor of Philosophy

December 2021

University of Southamtpon

Abstract

Faculty of Physical Sciences and Engineering
Optoelectronics Research Centre

Doctor of Philosophy

Pico- and Nanophotonics of Reconfigurable Metamaterials

by
Jinxiang Li

Picophotonics is the emerging science of light-matter interactions at the sub-nanometre scale. In nanomechanical metamaterials (NMs), picometric movements driven by thermal forces can be amplified by optical forces, opening up a novel way to explore their physics and applications. In this work I have:

- Designed and constructed a unique apparatus for investigation of thermal fluctuations and directional asymmetry of optical properties in NMs. This experimental setup is part-fiberized for stability, operating at telecommunications C-band wavelengths.
- For the first time, observed thermal fluctuations in the optical properties of metamaterials. High-frequency time-domain fluctuations of the optical properties of NMs are directly linked to picometre thermal motion of their components and can give information on fundamental mechanical frequencies and damping of mechanical modes. At room temperature the magnitude of metamaterial transmission and reflection fluctuations is of order 0.1% but may exceed 1% at optical resonances.
- Demonstrated, for the first time, that the natural frequencies and thermal fluctuation amplitudes of NMs can be optically controlled at $\mu W/\mu m^2$ intensities. The few - MHz natural frequencies of beams shift up to 3.6% and few tens of pm displacement amplitudes of thermal fluctuations vary up to 4.3% with light intensity of $0.8\mu W/\mu m^2$, providing active control of frequency response and may serve as a basis for bolometric, mass and stress sensing.
- For the first time, reported asymmetric transmission in a nanomechanical metamaterial driven by optical forces. I have experimentally demonstrated in NMs that resonant excitation of optical and mechanical sub-systems can lead to profound light-induced transmission asymmetry reaching 16% at μW power levels, making it suitable for a range of laser technology and fibre telecom applications.
- Shown, for the first time, that a free-standing, homogenous dielectric thin film can exhibit an optical magnetic response, i.e. without metamaterial nanostructuring. Indeed, such a response is an essential feature of homogeneous dielectric films at Fabry–Pérot resonances, which are formed by the interference of electromagnetic multipoles, including the magnetic dipole.

Contents

List of Figures

Declaration of Authorship

I, Jinxiang Li, declare that this thesis entitled, "Pico- and Nanophotonics of Reconfigurable Metamaterials" and the work presented in it are my own and has been generated by me as the result of my own research work.

I confirm that:

1. This work was done wholly or mainly while in candidature for a research degree at this University.
2. Where any part of this thesis has previously been submitted for a degree or any other qualification at this University or any other institution, this has been clearly stated.
3. Where I have consulted the published work of others, this is always clearly attributed.
4. Where I have quoted from the work of others, the source is always given. With the exception of such quotations, this thesis is entirely my own work.
5. I have acknowledged all main sources of help.
6. Where the thesis is based on work done by myself jointly with others, I have made clear exactly what was done by others and what I have contributed myself.
7. Parts of this work have been published as journal and conference contributions listed in the List of Publications.

Signature: ..... Date: .....

Acknowledgements

I am grateful to Prof. N. I. Zheludev and Prof. K. F. MacDonald for their supervision and guidance of my research. Working at Nanophotonics & Metamaterials group gives me an opportunity to understand the modern scientific society. I would like to thank Dr. Jun-Yu Ou, Dr. Behrad Gholipour, Dr. Vassili Savinov for their help on my project. I would also like to thank Dr. Kian S. Kiang and Dr. Libe Arzubiaga for their training in cleanroom and constructive discussions on my samples fabrication procedures. I would like to thank all the members in Nanophotonics & Metamaterials group for the time we shared and particularly Hao, Apostolos, Dimitros, Wei-Yi, Jie, Tongjun and Bruce for many interesting talks in academia and beyond. I would like to especially thank my life partner, Xi, with whom we shared all the happiness and sorrow in our academic journey. My grandfather Xianruo has also a place here. His attitude to life shaped my personality. Finally, I acknowledge the support and patience of my family member, who made the work presented in this thesis possible.

Dedicated to my grandfather Xianruo Liu

List of Abbreviations

ALT	**A**symmetric **L**ight **T**ransmission
ASD	**A**mlitude **S**pectral **D**ensity
CCD	**C**harge-**C**oupled **D**evice
CMOS	**C**omplementary **M**etal-**O**xide-**S**emiconductor
CW	**C**ontinue **W**ave
EBL	**E**lectron-**B**eam **L**ithography
ED	**E**lectric **D**ipole
EO	**E**lectric **O**ctupole
EOM	**E**lectro- **O**ptical **M**odulator
EQ	**E**lectric **Q**uadrupole
FEM	**F**init **E**lement **M**ethod
FIB	**F**ocused **I**on **B**eam
MD	**M**agnetic **D**ipole
MEMS	**M**icro-**E**lectro-**M**echanical **S**ystem
MQ	**M**agnetic **Q**uadrupole
NA	**N**umecial **A**pparatus
NM	**N**anomechanical **M**etamaterial
NMP	**N**-**M**ethyl-2-**P**yrrolidone
PECVD	**P**lasma-**E**nhanced **C**hemical **V**apour **D**eposition
PSD	**P**ower **S**pectral **D**ensity
RMS	**R**oot-**M**eam-**S**quare
SEM	**S**canning **E**lectron **M**icroscopy
TD	**T**oroidal **D**ipole

Chapter 1

Introduction

The growing demand for fast information transmission, efficient signal processing and big data storage is close to surpassing the capacity of current systems. Benefiting from the bandwidth of light, photonic systems are considered as preferable platforms on which information can be transmitted through fibres and waveguides. Electronic systems, in comparison, are superior in data processing and storage as they have achieved a high level of integration and miniaturization[1]. However, the bandwidth limitations of the electronic platforms have almost been reached[2]. One of solutions is using photons as an alternative to process and store information, because they can provide more channels, such as polarization and orbital momentum, to achieve that functionalities[3]. Metamaterials, consisting of sub-wavelength metamolecules, offer a novel playground for manipulating light-matter interaction. A large amount of intriguing properties, such as negative refractive index[4], superlenses[5] and artificial magnetism[6], are allowed to be obtained by engineering the shape and dimensions of metamolecules, making metamaterials eligible candidates for hosting all-optical information processing and optical data storage.

1.1 Reconfigurable metamaterials

Even though metamaterials are capable of showing remarkable properties, practical applications based on metamaterials would significantly benefit from dynamic control of their properties. Several approaches to achieve reconfigurable metamaterials have been investigated, including employing superconductors[7] and phase change materials[8]–[10] to construct metamaterials. Superconducting metamaterials, operating in microwave and sub-THz range, allow the tuning of properties upon temperature changes[7]. Regarding phase change materials, they can also offer a solution in the visible range to dynamically control the refractive index change between different states[8]–[10]. Furthermore, if the operation speed is not the most important aim of the reconfigurable metamaterials, microelectromechanical systems (MEMS) can also be utilized to build tunable metamaterials, which have been demonstrated for THz frequencies[11]–[13], see Fig. 1.1. The change in optical properties of such reconfigurable metamaterial arises from structural displacements and geometry changes within MEMS metamaterials.

Nanomechanical metamaterials with physical dimensions further decreased into sub-micrometre scale could potentially provide faster response speed. The basic

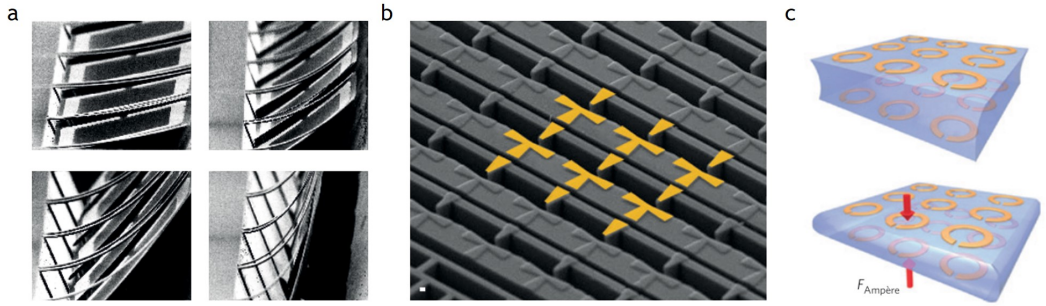

FIGURE 1.1: Tunable MEMS metamaterials for Terahertz (THz) waves. (a) A reconfigurable THz metamaterial that is in response to a thermal stimulus[11]. (b) A THz metamaterial tuned by MEMS actuators[12]. (c) A magnetoelastic microwave metamaterial actuated by Ampere's force[13].

idea behind nanomechanical metamaterials can be described as the realization of balance between electromagnetic forces and elastic forces. Specifically, the electromagnetic forces between constituent elements increase with the decrease of the dimension of nano-objects, while elastic forces drop with the decrease of size[14]. That is to say, nanomechanical metamaterials could provide a platform where electromagnetic Coulomb(Fig. 1.2(b)), Lorentz force(Fig. 1.2(c)) are able to compete with elastic forces and thus be used to reconfigure the shape of individual metamolecules or to change their mutual arrangement. These nanomechanical metamaterial building blocks can move fast, potentially offering modulation at gigahertz frequencies[15]. Furthermore, nanomechanical metamaterials can also be driven by thermal forces (Fig. 1.2(a)) or by optical forces (Fig. 1.2(d)) arising from illuminated metamolecules.

In this thesis, nanomechanical metamaterials are employed as medium, driven by thermal and optical forces, to modulate light for exploring optical induced thermal

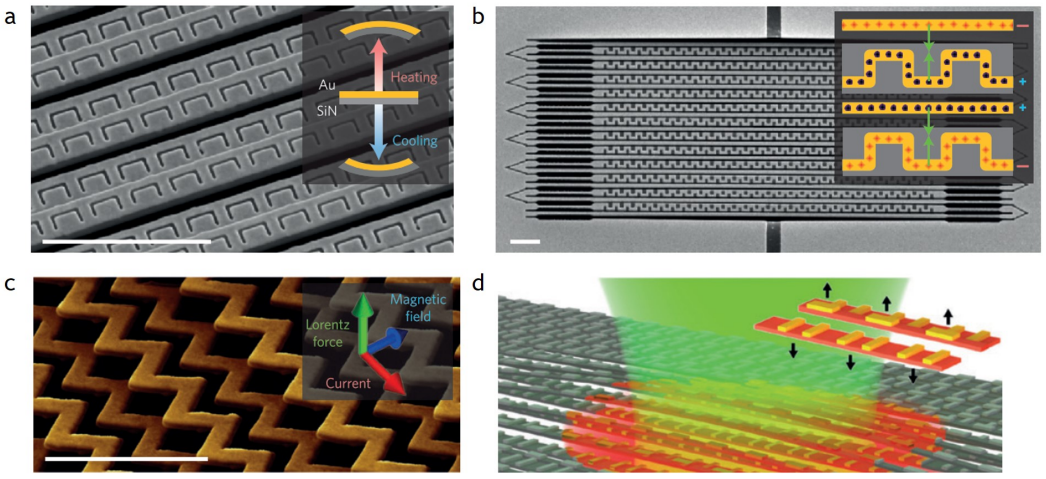

FIGURE 1.2: Nanomechanical metamaterials. (a) A reconfigurable optical metamaterial driven by thermal effects[16]. (b) An electro-optical modulator actuated by electrostatic forces[17]. (c) A magneto-optical modulator driven by Lorentz force[18]. (d) An all-optical modulator actuated by optical force[19].

fluctuations properties and achieving transmission asymmetry functionality.

1.2 Thermal motion

In the experiments showing in Chapter 3 and 4, I have investigated the identification and tuning of the Eigenfrequencies of nanomechanical metamaterials characterized by thermal motion behaviours of the components of nanomechanical metamaterials. Eigenfrequencies of vibration are important as they determine the frequencies at which harmonic oscillation may be driven efficiently, to large amplitudes and to the nonlinear regime. These frequencies increase as objects decrease in size, reaching the mega- to gigahertz range at the nanoscale. Ideally, the constituent elements of nanomechanical metamaterials are driven in synchronous resonant (i.e. large amplitude) oscillatory motion to achieve maximum optical effect. In practice, little is known about the mechanical characteristics of nanomechanical metamaterials. Thermal motion, first observed by Robert Brown in 1827 as erratic motion of pollen grains in water and explained by Albert Einstein in 1905 [24], presents a chance to address this challenge. As weakly-damped nanoscale oscillators possess small enough mass, the random, white-noise thermal motion driving force is sufficient to induce relatively large amplitude oscillations at their mechanical Eigenfrequencies[25]–[27]. Therefore, nanomechanical metamaterials can be expected to transduce picometric scale thermal displacements to fluctuations of their optical properties, providing an opportunity for optical characterization of their mechanical properties. In particular, this applies to highly sensitive photonic metamaterials supported by flexible nanomembrane structures that show giant electro-optical[17],

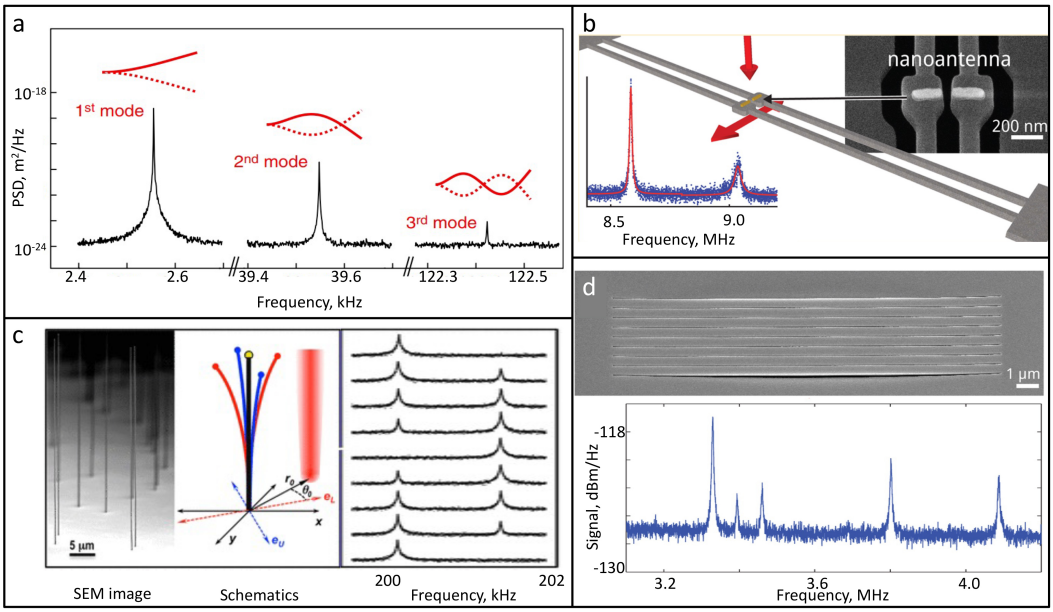

FIGURE 1.3: Thermomechanical transduction observed in a cantilevers(a)[20], single plasmomechanical dimer antenna(b)[21], vertical nanowire resonators(c)[22] and metal-insulator-metal double-clamped beams(d)[23].

magneto-electro-optical[18], phase change[28] and nonlinear optical[19], [29], [30] responses.

Thermomechanical transduction of natural oscillations has been observed in cantilevers[20], [31], single plasmomechanical dimer antenna[21], vertical nanowire resonators[22] and metal-insulator-metal resonators [23] as well as other optomechanical systems[32], and exploited in atomic force microscopy[33]. In a metamaterial, all structural elements of the same type should preferably be mechanically identical (i.e. in terms of natural frequencies and quality factors) to exclude inhomogeneous broadening of the optical response. In practice, due to material and manufacturing imperfections, this is rarely the case and interrogation of the metamaterial ensemble's thermomechanical response can provide insight to the dispersion of mechanical properties (see Chapter 3). Furthermore, optically controlled eigenfrequencies of nanomechanical metamaterials (see Chapter 4)may serves as a basis of practical applications, such as bolometer, mass and micro/nanostructural stress sensor.

1.3 Transmission asymmetry

In my experimental work (Chapter 5), I explored transmission asymmetry features of nanomechanical metamaterials. Hence, it is necessary to give a brief introduction of the concept on transmission asymmetry.

Reciprocity is a fundamental principle in optics, resulting from linearity and time-reversal symmetry. This requires that transmission properties of electromagnetic wave are the same when source and detector are switched. It sets foundational barriers to realize all-optical signal processing, especially to asymmetric devices such as isolators, circulators and non-reciprocal phase shifters (gyrators) which

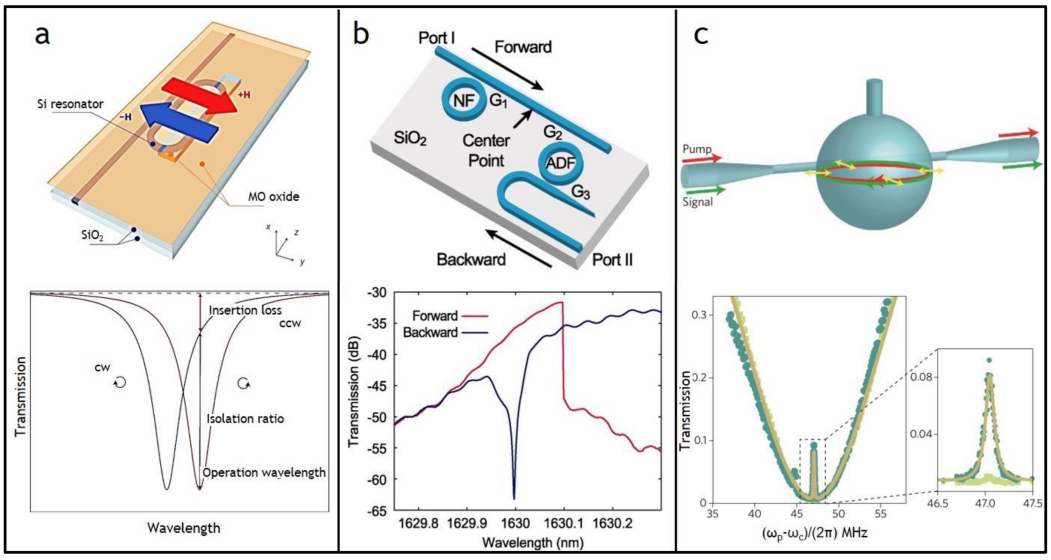

FIGURE 1.4: Asymmetric transmission based on optical non-reciprocity. (a) On-chip optical isolator based on magneto-optical effects[34]. (b) All-silicon passive optical diode based on optical nonlinearity[35]. (c) Cavity-based optomechanical isolator[36].

are commonly used in optical communication. Recently, asymmetric light transmission (ALT) devices have sparked increasing interests due to its potential for breaking these barriers. Generally, an optical device that offers big transmission differences between backward and forward illuminations can be considered as an ALT device.

A typical way to obtain transmission asymmetry is the utilization of optical non-reciprocity [37]. Traditional approaches to break reciprocity involve the interaction between a magnetic field and magneto-optic materials [34], [38], as the precondition of deriving reciprocity theory is based on linear time-invariant materials with symmetric permittivity and permeability tensors, that is not satisfied by magneto-optic materials. However, this method is not appealing to current photonic systems, in which features like compact size, integrability and low cost are preferred. Moreover, the large loss of magneto-optical materials at optical frequencies make them not a good option for low-energy consumption devices. Even though state-of-the-art on-chip implementations have achieved isolation ratios as high as 19.5 dB at telecom wavelengths[34] using this approach (see Fig. 1.4 (a)), it requires non-standard materials and introduces scaling and integration problems. Hence, the search for alternatives to realize non-reciprocity without external magnetic field has recently spawned many novel ways. One of them is the utilization of nonlinear materials [35], [39]–[41], which is not limited by reciprocity principle. Although a forward-backward transmission ratio of up to 25 dB at telecom wavelength(Fig. 1.4(b)) was achieved by Li et al. [35]. This method works only for signals of sufficiently high intensity and incident signal for only one port at a time [37], [41]. In addition, optomechanics offer another opportunities for building non-reciprocal devices [36], [42], [43], as temporal modulations can be induced by mechanical resonances(Fig. 1.4(c)).

Another way to obtain ALT is based on reciprocal systems. A specific asymmetric mode conversion can be obtained via breaking spatial symmetry of structures,

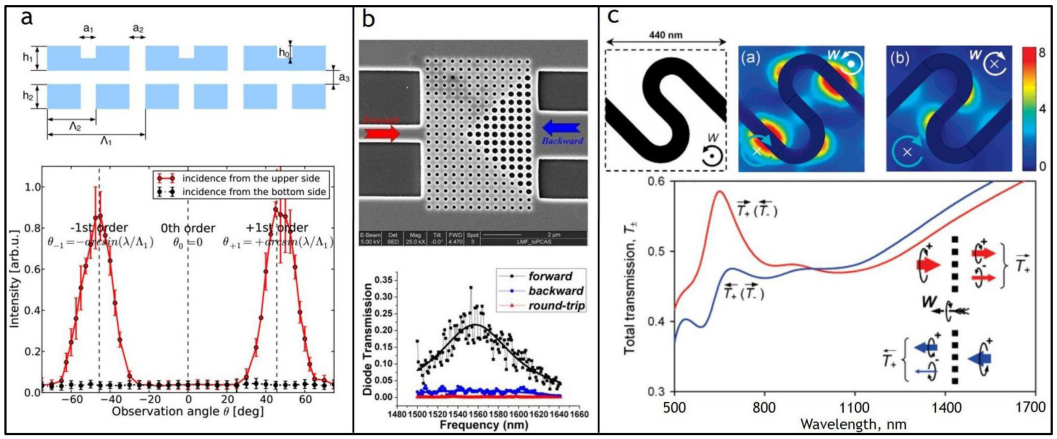

FIGURE 1.5: Asymmetric transmission based on reciprocal system. (a) Asymmetric transmission at terahertz range in a double grating[44]. (b) A optical diode based on photonics crystal[45]. (c) Asymmetric Transmission in chiral metamaterials[46]

leading to light transmission differential between backward and forward illumination directions. ALT devices built via this approach are able to be realized without limitation to certain materials, while some of ALT devices based on non-reciprocity require a specific materials, such as magneto-optic materials or nonlinear medium. So, materials which is compatible with complementary metal-oxide-semiconductor (CMOS) fabrication process can be selected to make devices. So far, a wide range of reciprocal ALT devices have been achieved based on different spatial symmetry breaking, such as asymmetric grating(Fig. 1.5(a)) [44], [47], [48], photonic crystals(Fig. 1.5(b))[49], [50] and chiral metamaterials(Fig. 1.5(c))[46], [51], [52]. They can meet some practical needs for specific applications.

1.4 Thesis synopsis

Driving nanomechanical metamaterials via thermal and optical forces opens up a novel approach to access new optical properties and pursue devices with remarkable functionalities. In this thesis, reconfigurable nanomechanical metamaterials working at telecommunication wavelength range that have nanoscale metamolecules and picometres movement features are developed for exploring thermal fluctuation properties and achieving transmission asymmetry functionality.

Chapter 2 presents manufacture techniques for fabricating nanomechanical metamaterial samples. Experimental apparatus utilized in measuring thermal motions and asymmetric optical responses of nanomechanical metamaterials are also presented in this chapter. Furthermore, basic theories and computational models for analysing mechanical and optical properties of nanomechanical metamaterials are introduced to gain a better understanding of observed experimental phenomena.

Chapter 3 focuses on the first experimental observation on thermal fluctuation of the optical properties of nanomechanical metamaterials. This finding indicates that thermal fluctuations of the optical transmission and reflection spectra of nanomechanical metamaterials are capable of giving information on mechanical frequencies and damping of mechanical modes, setting fundaments to the research in following chapters.

Chapter 4 presents optical control of thermal motions in nanomechanical metamaterials. Both eigenfrequencies and root-mean-square(RMS) displacement of the components of nanomechanical metamaterials can be tuned both by light power (down to a few μW) and light illumination directions.

Chapter 5 reports experimental evidence on asymmetric transmission in nanomechanical metamaterials driven by optical forces. Numerical models are firstly conducted to predict transmission asymmetry induced by optical forces to guide the sample fabrication processes. Moreover, I have experimentally presented in nanomechanical metamaterials that resonant excitation of optical and mechanical subsystems could produce profound light-induced transmission asymmetry at low microwatt power levels.

Chapter 6 demonstrates optical magnetic response in a free-standing dielectric thin film, in which Fabry–Pérot resonances are formed by the interference of electromagnetic multipoles, including the magnetic dipole.

Finally, the works covered in this thesis are concluded in Chapter 7, together with an outlook for potential directions extended from current works.

Chapter 2

Methods

The method for measuring and analysing optomechanical properties of nanomechanical metamaterials will be described in this chapter. Firstly, the fabrication details for creating metamaterials are shown in section 2.1, where two manufacturing approaches, e.g. focus ion beam (FIB) milling (section. 2.1.1) and electron-beam lithography (EBL) (section 2.1.2), were utilized to produce desired samples. In section 2.2, I present the measurement setups, including the vacuum chamber, MEMS switch, optics, electronics, for optical characterization of manufactured samples. In addition to experimental approaches, analytical models and computational methonds are introduced in in section 2.3 and 2.4 to gain better understanding of observed experimental phenomena.

2.1 Sample fabrication

Nanomechanical metamaterials, measured in chapter 3, were manufactured based on low tensile stress (tensile/compress stress σ: the normal force per area that causes an object to increase /decrease in length) silicon nitride (Si_3N_4) membrane (σ <250 MPa), with 250× 250 μm square windows on 5× 5 mm square frames (Norcada, Inc), and the thickness of Si_3N_4 is around 200 nm.The photograph of this type of membrane can be found in Fig. 2.1. While another type of customized Si_3N_4 membrane (Norcada, Inc) with 8 narrow slit windows (length: 400 μm, width vary from 10 to 75 μm) was utilized for manufacturing samples employed in chapter 4 and 5. Fabricated nanomechanical metamaterials can be directly anchored onto frame in this type of customized membrane, making mechanical properties of the samples more stable. To prepare Si_3N_4 / silicon(Si) bilayer film, plasma-enhanced chemical vapour deposition(PECVD) is then utilized, at base pressure of 5×10^{-7} $mbar$, to deposit 115 nm of Sion the front side of Si_3N_4 membrane and deposition temperature was 200 °C.

2.1.1 Fabrication via FIB milling

The membrane with Si_3N_4 / Si bilayer was then structured by FIB milling to define the array of asymmetric nano-bricks in Si layer and parallel supporting beams in the Si_3N_4 layer. A gallium ion(Ga^+) beam with acceleration voltage of 30 Kev and beam current of 48 pA were used in a FIB system (FEI Helios-600). The membrane

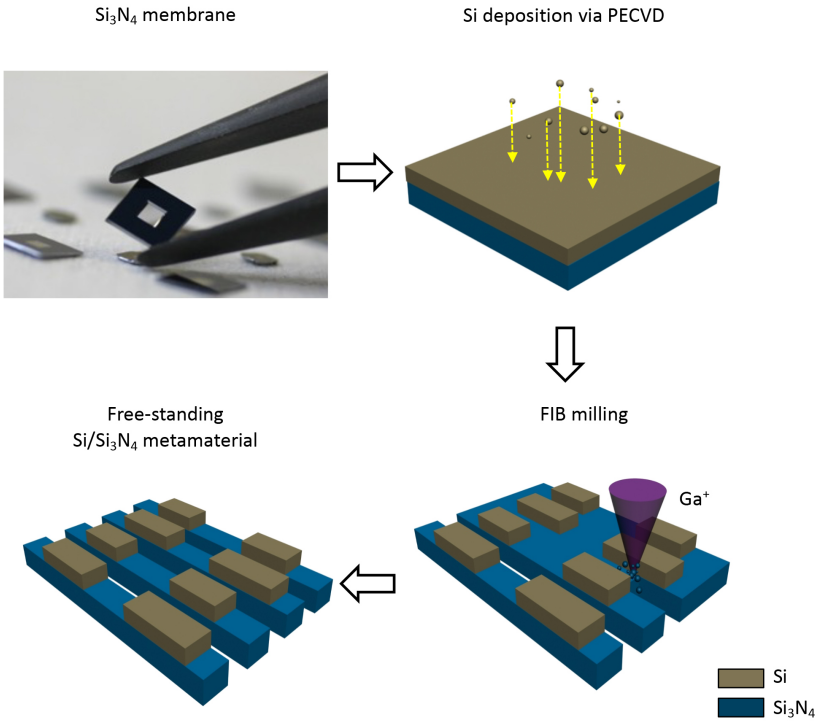

FIGURE 2.1: Flow-chart of FIB milling processes to fabricate nanomechanical metamaterials samples.

was milled from Si side as show in Fig. 2.1, to get Sinanobricks at first, and then Si_3N_4 layer was etched through to obtain free-standing beams. To mill the desired patterns, FIB system was controlled by a nanometer pattern generation system, in which the target shapes and dimensions of nanomechanical metamaterials can be predefined. In order to make the beams easier to be driven either thermally(Chapter 3 and 4)or optically(Chapter 5), I also create tapering parts at two ends of beams (see Fig. 2.2) inspired by Ou's previous work[19].

It is important to prevent neighbouring beams collapsing into each other while fabricating free-standing beams. To do so, the beams were milled in an alternative way. Specifically, a wide beam with width of two beams was firstly milled to release stress in membrane, this wide beam was then cutting through into two beams. This procedure leads to a fact that neighbouring beams tend to owe similar tensile stress, verified by the later measurements in chapter 3.

Fig. 2.2 shows fabrication outcomes of FIB milling process introduced above. Fig. 2.2(a) presents the SEM image of a typical nanomechanical metamaterials sample with 0^o tilt angle. It consist of two parts, the metamaterials part at the centre and connection part, e.g. tapering part as I mentioned, at the end of beams. In terms of metamaterials part, it consists of two types nanobricks (see the inset in Fig. 2.2(a)), one type of bricks has longer length and wider width, while another has shorter length and narrower width. This dimensional asymmetry creates optical Fano resonance and resonant enhanced optical forces. And the tapering part is

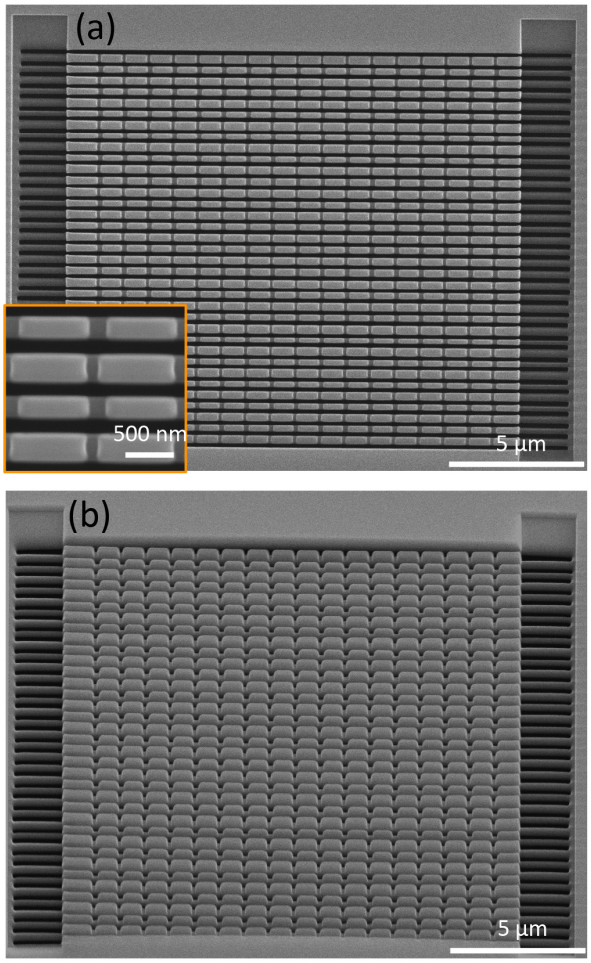

FIGURE 2.2: SEM image of fabricated sample via FIB milling (a) 0^o tilt, (b) 52^o tilt

responsible to enhance the transduction sensitivity. Fig. 2.2(b) gives the SEM image of the metamaterial with 52^o tilt angle, in which one could check side profile of the sample. It can be found that the initial height position of beams are roughly at the same level.

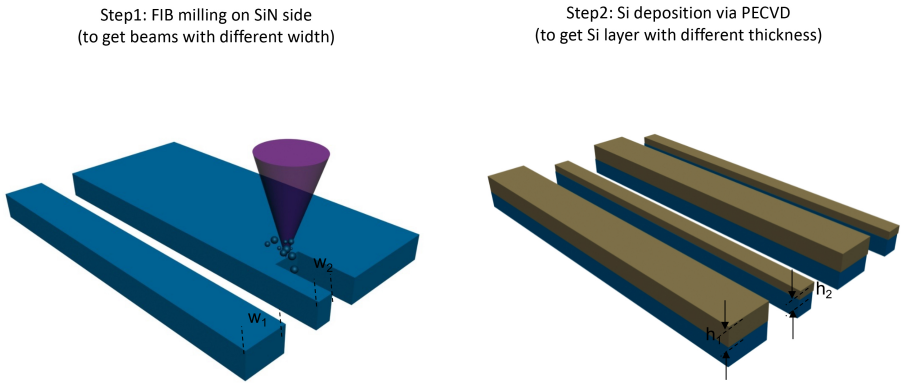

FIGURE 2.3: Flow-chart of fabrication process to produce metamaterials with different height.

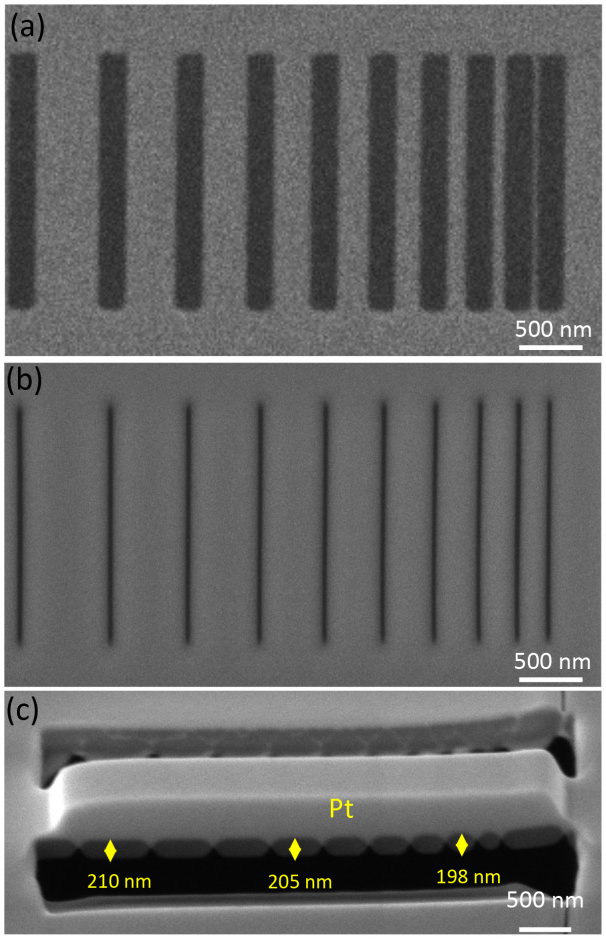

FIGURE 2.4: SEM image of fabricated nanowire sample with different height. FIB fabricated grating (a) before a-Si depositon, (b) after a-Si deposition. (c) Cross section of fabricated sample with 52^o tilt angle.

Apart from utilizing different length and width of nanobricks to achieve asymmetric transmission which is the one of main goals of this project, one could also get good transmission asymmetry by using the thickness dissimilarity of beams (see Chapter 5). Previously, a design of metamaterials with different height proposed[30]. However, there is no resonance observed for the fabricated sample (via FIB) based on this kind of design (see Appendix E) because of severe Ga^+ implantation[53]. In addition to this normal FIB milling process, another option to create different thickness is through PECVD. In this protocol, beams with different width are assumed to have distinct Si deposition rate.

In Fig. 2.3, the flow-chart for fabricating samples with height via this way is given. The FIB procedure is firstly employed to create grating with different width on Si_3N_4 membrane. After that, PECVD is utilized to deposit a-Si on grating with different height. However, there are several potential issues in this protocol. One of issues is non-uniform tensile stress distribution inside of membrane produced by FIB milling, and this stress imbalance could be further increased when doing PECVD process due to high deposition temperature (200 °C), leading to decreasing

rate of success manufacturing. The other issue is side-growth of Si. Fig. 2.4(a) and(b) show the SEM image of a grating with different width before and after a-Si deposition, one could clearly find that the width of beams are also increased after deposition process, which is not desired in the origin design. Then, I checked if the thickness differences created by this protocol meet the expectation. Fig. 2.4(c) depicts the cross-section image of the fabricated sample to measure the thickness difference. Side-growth effects could also be observed in this view, in which the width of grating increased. Moreover, the thickness differences is only around 12 nm for a large width dissimilarity and such a small differences could not meet our requirement for obtaining optical resonances. Hence, the design with asymmetry in length and width of nanobricks will be focused in the following chapters.

2.1.2 Fabrication via electron-beam lithography

As mentioned in the previous section, FIB process is capable of creating our desired patterns. And this process can be simplified as two main steps: materials deposition and FIB milling. There is no solvent-based process involved in this approach. Hence, surface adhesion, such as resist and hard masks, would not be an issue. However, the Ga^+ ion implantation on the surface of samples during fabrication process is inevitable[53] which undermine the optical properties, such as Quality factor (Q-factor: the ratio of stored energy to the energy lost per cycle of oscillation, characterizing the dissipation of nanomechanical metamaterials. It is determined by non-radiation losses of consisted materials, such as the Ohmic loss; and radiation losses, such as scattering loss due to the surface roughness and non-uniformity of the samples) and absorption, of the fabricated nanomechanical metamaterials. Because optical forces that utilized to driven metamaterials in Chapter 5 is sensitive to the Q-factors (see Fig. 5.9), samples with poor Q-factor would require higher input laser power levels for generating sufficient optical forces to drive nanomechanical metamaterials efficiently. In addition, large absorption coefficients induced by Ga^+ implantation make samples fragile to laser powers.

In order to improve the quality of samples, we then developed a new approach based on full EBL to enable Ga^+ contamination-free nanomechanical metamaterial samples with higher Q-factor. This approach includes two round of EBL processes. The first round of EBL process includes a-Si deposition, e-beam exposure, e-beam evaporation of chromium(Cr) as hard mask, metal lift-off and reactive ion etching (RIE) etching steps to obtain Si nanobricks on the Si_3N_4 membrane. While the second round of EBL process is conducted to cut through Si_3N_4 membrane producing free standing beams with nanobricks on them. Fig. 2.5 shows the schematics of these steps.

Regarding the membrane used in this EBL procedures, I used customized low-stress (σ <200 MPa) 200 nm thick silicon nitride membrane (Norcada, Inc.) with two narrow slit window (400 $\mu m \times$(40 & 50) μm). In these slit membranes, the nanomechanical metamaterials can be anchored directly on the frame, making the

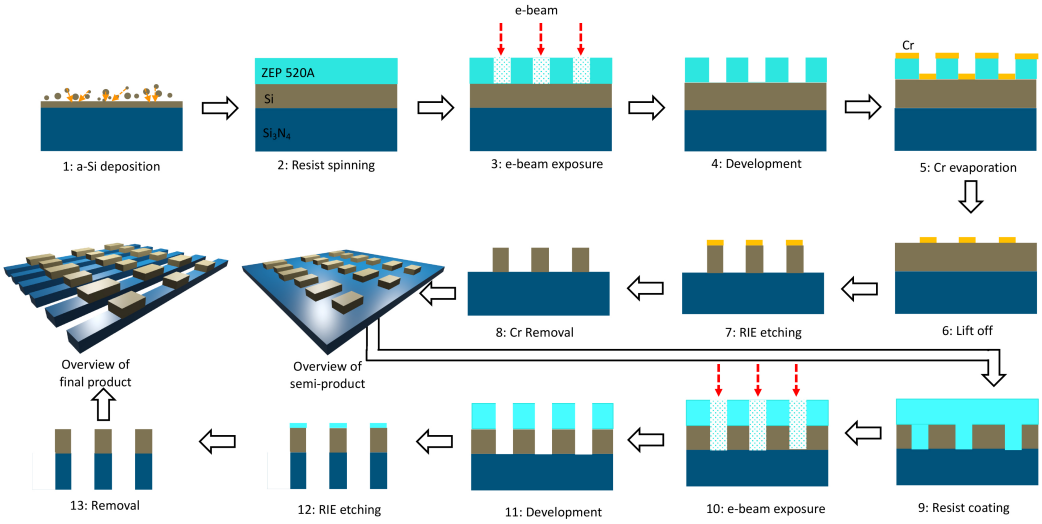

FIGURE 2.5: Flow-chart of EBL process to produce nanomechanical metamaterial samples. (NB: the 3D-sketch images in this flow-chart show semi-product and final product after 1^{st} and 2^{nd} round of EBL process)

mechanical properties of samples more stable as we mentioned before. The larger frame size ($10\times10\ mm$) is utilized in the EBL procedures to make membrane samples compatible with e-beam exposure machine.

Table 2.1 shows the workflow details of these two round of EBL procedures. I firstly clean Si_3N_4 a membrane sample with ashing machine for 5 min to clean dusts on membrane surface. This cleaned membrane is then put into PECVD machine for $130s$ to deposit Si, the deposition temperature is around 200 °C and base pressure is $4.8 \times 10^{-7} mbar$. The positive-tone resist ZEP520a, diluted with anisole, is then employed for e-beam exposure process. Because the frame size is still relative small compared with standard wafer size, and the membrane sample quite fragile, coating a uniform layer of resist can be a challenge task. Here I use a larger silicon chip as substrate and attach our small membrane chips on it with Kapton tapes. This assembly is then put onto spinner to do resist spinning. The spinner first spins slowly to check if the centre of membrane window is well-aligned to the rotation axis of the spinner. After that the resist will be spun on the sample. An e-spacer layer is then coated on the resist to prevent charging issues during e-beam exposure process.

After e-beam exposure, the sample is immersed into developer (ZED-N50) for 90 s and then into IPA for another 30 s to remove the residuals. The developed sample are inspected by a microscope to check if it is well developed. In order to get a good side-wall quality of nanobricks, a layer of hard mask is necessary for RIE process. Here we choose Cr as hard mask material and deposit it onto resist layer via e-beam evaporator. To ensure good pattern could be transferred onto Si/Si_3N_4 membrane via lift-off process, it generally requires at least 5: 1 ratio of resist and metal mask thickness. Hence, we deposit a thin layer (35 nm) of Cr onto resist layer and then doing lift-off process with N-methylpyrrolidone (NMP) solvents for at least 2 hours. In the mean time, a syringe is utilized to aid the lift-off process.

TABLE 2.1: EBL workflow. The step numbers refer to the schematics shown in Fig. 2.5

step	description	details
1	a-Si deposition	plasma ashing,5 min 110 nm a-Si deposition via PECVD
2	resist spinning resist baking e-spacer spining	ZEP520A : anisole=2:1 2370 rpm for 60 s thickness $\approx$ 350 nm 180 °C, 2000 rpm for 90 s
3	e-beam exposure	write field = 100 μm aperture =10 μm, area dose = 100 $\mu C/cm^2$
4	e-spacer removal resist development	DI water, 30s ZED - N50, 2 min IPA, 30 s
5	Cr evaporation	35 nm Cr via e-beam evaporator as hard mask
6	Cr lift-off	N-methyl-2-pyrrolidone (NMP) At least 2 hours, use syringe to aid lift-off Rinse IPA, 30 s
7	a-Si layer etching	RIE etching, 7 min 30 s gas: $CHF_3(18sccm)$, $O_2(2sccm)$ RF power: 75W
8	Cr removal	Cr etchant : 8 min DI water rinse: 1min
9	resist spining resist baking e-spacer spining	ZEP520A : anisole=2:1 2370 rpm for 60 s thickness $\approx$ 500 nm 180 °C, 2000 rpm for 90 s
10	e-beam exposure	write field = 100 μm aperture =10 μm, area dose = 100 $\mu C/cm^2$
11	e-spacer removal resist development	DI water, 30s ZED - N50, 2 min IPA, 30 s
12	Si_3N_4 layer etching	RIE etching, 15min gas: $CHF_3(18sccm)$, $O_2(2sccm)$ RF power: 75W
13	resist removal	RIE etching, 5 min gas: $O_2(10sccm)$ RF power: 50W

The transferred Cr patterns are inspected under SEM to check if the patterns are under good conditions. Once the situation ensured, an etching process is conducted via RIE machine for 7.5 min to produce Si nanobricks on Si_3N_4 membrane. Finally the hard mask layer is removed by Cr etchant for 8 min.

To cut through Si_3N_4 membrane, another round of EBL process is in need. This procedure is quite similar to the first round of EBL but without hard mask deposition

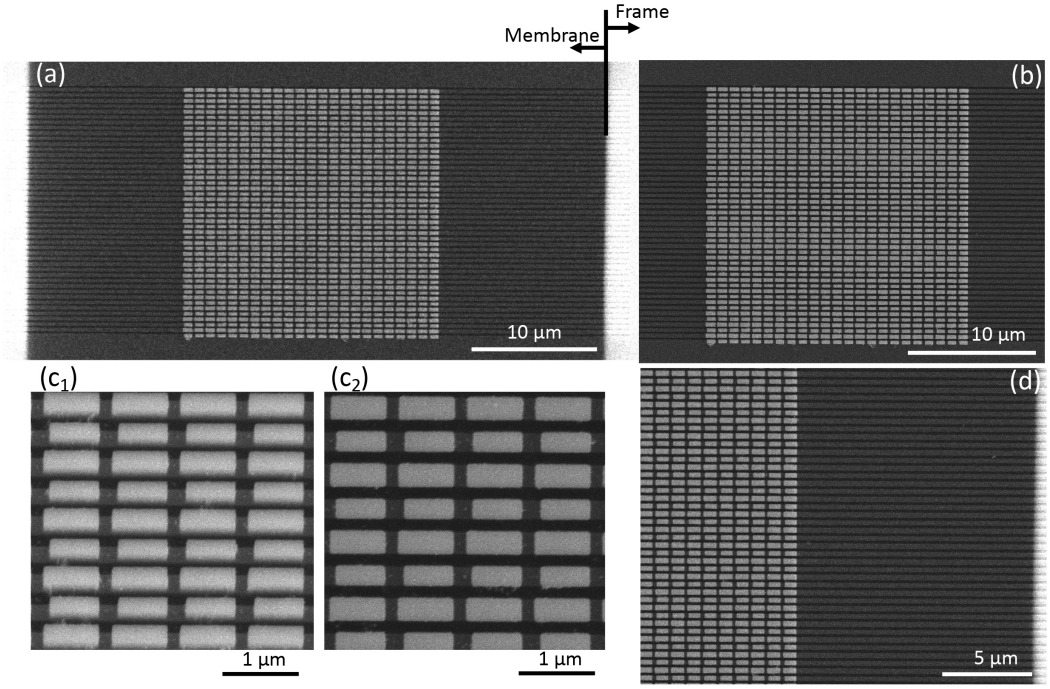

FIGURE 2.6: SEM image of fabricated sample via EBL processes. (a) The over view of whole sample, the frame and membrane area are indicated by annotation in figure; (b) the centra metamaterials part; (c) zoom-in image of central part of nanomechanical metamaterials at 30^o deg (c_1)and 0^o (c_2) tilt angle; (d) the connection part of metamaterials.

and lift off process as main optical properties are determined by Si nanobricks, So the side-wall quality of SiN beams is not that important. Another reason is that once the SiN beams get cutting through, one should avoid any further wet process getting involved in the following steps, because wet process could potentially introduce issues, such as beams collapse and membrane break. However, if the Cr get deposited as hardmask for following lift-off process, it need to be removed via Cr etchant finally and that is a wet process.

Once this second round EBL process is finished, the final fabricated sample obtained as shown in Fig. 2.6. One can see that nanobricks have a very good uniformity and it looks like from Si side that there is no stickiness between neighbouring beams.

Furthermore, I checked the transmission spectra of this sample and compared it with the samples fabricated by FIB milling, shown in Fig. 2.7. It can be seen that the Q-factor of the peak we interested (around 1500-1600 nm) for the samples fabricated by EBL process is higher than that for the samples fabricated by FIB process. However, the spectral position of resonance for the EBL sample is blue-shifted from our targeting spectral range (C-band) due to the etching rate fluctuation after a round of maintenance of cleanroom.

In order to make the best use of this sample, the measurement for detecting thermal fluctuation of this sample is conducted at its resonant wavelength as the procedure described in Chapter 3. However, there is no thermal peaks observed in

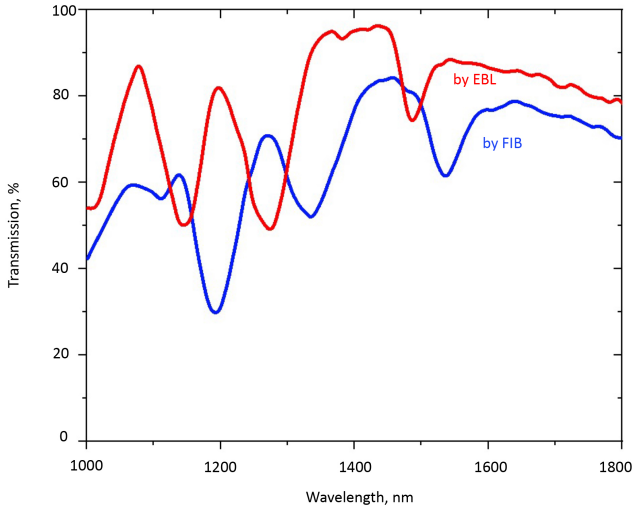

FIGURE 2.7: Comparison of transmission spectra of the samples fabricated by FIB and EBL approach.

this sample, implying that there is no movement within this nanomechanical metamaterial. The reasons could come from either the Si_3N_4 is not cutting through or there is Si residuals (from the first round etching process) connecting the neighbouring beams. Both of these two reason could silent mechanical modes in this sample.

To verify this assumption, I inspect the EBL sample from both Si_3N_4 side and Si side as shown in Fig. 2.8. It can be confirmed from zoom-in image Fig. 2.8(b) and (d) that the Si_3N_4 layer is cutting through. However, a imperfect lift-off process leaves hardmask Cr in between neighbouring bricks, which finally produce the Si residuals in undesired position after RIE process. And this Si residuals bridge neighbouring beams. The positions with connected bridge produced by Si residuals are indicated by coloured arrows in Fig. 2.8 from Si (b) and Si_3N_4 (d) sides. This inspection concludes that a more clean lift-off process is required in the future process to successfully produce nanomechanical sample with high Q-factor via EBL procedure. I think that there are two ways to improve current lift-off process. One of them is the decrease deposition thickness of the hard mask material (e.g. Cr), which makes it easier to be removed during lift-off process. The cost of this approach would be the side-wall quality of fabricated sample. The other method to obtain a clean sample with less Cr residual after lift-off process is doing this procedure under ultrasonic bath. However, as the membrane we are currently using is only 200 nm thick, it would be a challenge task to do ultrasonic bath based lift-off process without breaking membrane. To meet this challenge, one could start with a thicker Si_3N_4 membrane which is capable of keeping itself intact during ultrasonic process. After the first-round of EBL process, RIE could be utilized to etch the Si_3N_4 membrane to desired thickness from Si_3N_4 side.

Due to COVID-19, the access to cleanroom is severely limited. I do not have chance to carry on this EBL processes to produce a functional nanomechanical

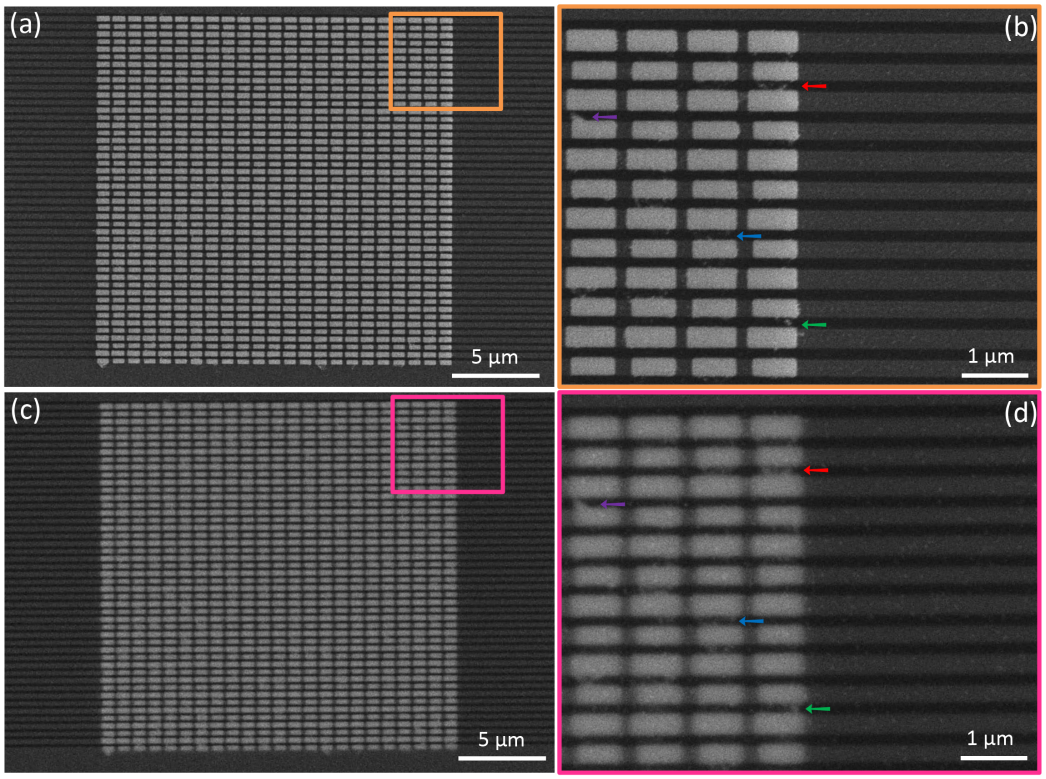

FIGURE 2.8: Comparison of geometry profile of the sample fabricated by EBL from two sides of membrane. (a)(b) SEM image of the sample from Si side for overview (a) and zoom-in (b) perspective, where yellow rectangular area in (a) indicates the zoom-in part in (b). (c)(d) SEM image of the sample from Si_3N_4 side for overview (c) and zoom-in (b) perspective. Arrows in (b) and (d) depicts the connection part between neighbouring beams.

sample. However, I think this experience could be helpful to my colleagues who are interested in exploring fabrication of nanomechanical metamaterials via EBL method.

Even the Q-factor is improved for the sample manufactured by EBL approach, this improvement is not as good as I expected due the residuals. Furthermore, EBL is a time-consuming process, taking 1-2 weeks to obtain a group of samples on one membrane. In comparison, sample can be fabricated by FIB within 4-5 hours. The saved time in FIB process can be spent to optimize sample design and manufacturing parameters for mitigating the adverse influence of Ga^+ contamination. Hence, I will concentrate on the samples which are fabricated by FIB process in the following chapters.

2.2 Experimental apparatus

In this section, the experimental apparatus will be introduced to focus the laser spot on the nanomechanical metamaterial samples and to measure their optomechanical responses. Schematics for three measurement setups employed in chapter 3-5 have been shown in Fig. 2.9. Specifically, Fig. 2.9(a) depicts the setup for measuring thermal fluctuation of a nanomechanical metamaterial sample (Chapter

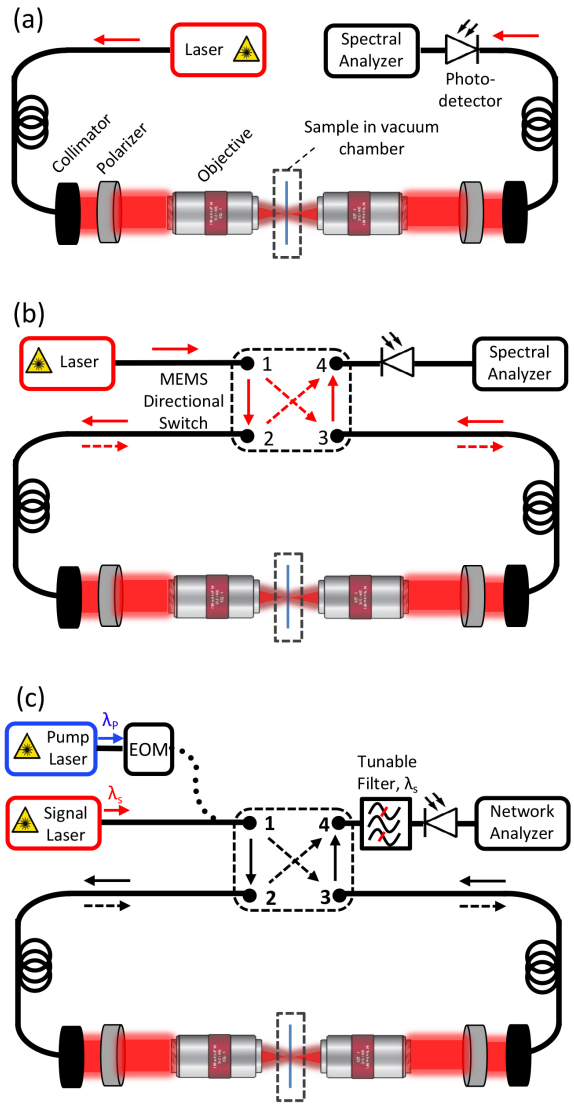

FIGURE 2.9: Schematics of setup for measurement of (a) thermal fluctuation of nanomechanical metamaterials; (b) thermal motion tuning in nanomechanical metamaterials and (c) asymmetric transmission in nanomechanical metamaterials.

3), Fig. 2.9(b) shows the apparatus for optically tuning thermal motions of the nanomechanical metamaterial (Chapter 4) and Fig. 2.9(c) gives the equipment for achieving asymmetric transmission functionality in nanomechanical metamaterials (Chapter 5). In Fig. 2.9(a), a fiber-coupled telecommunication tunable diode laser (ID Photonics CoBrite - DX2) working at C-band wavelength range is utilized as light sources. A home-made column microscope is built with symmetric equipments in the both side of samples (shown in Fig. 2.10) to reduce systematic errors, in which 8 supporting pillars are added in the microscope to stabilize the system and the laser beam is decoupled into free space via a fibre collimator. As the sample is polarization sensitive, a pair of polarisers are added in the microscope (measurements and modelling outcomes to verify the polarization dependence of the sample

can be found in Appendix B). Once the laser passing through the polarizer, it is focused onto the sample by a 20× magnitude, long working distance (20 mm) IR objective (Mitutoyo). The diameter of focused laser beam is around 5 μm. And the sample is placed in a home-made vacuum chamber (see design drawing in Fig. 2.11) evacuated to the pressure of around 4 $\times 10^{-3}$ mbar, and this value is limited

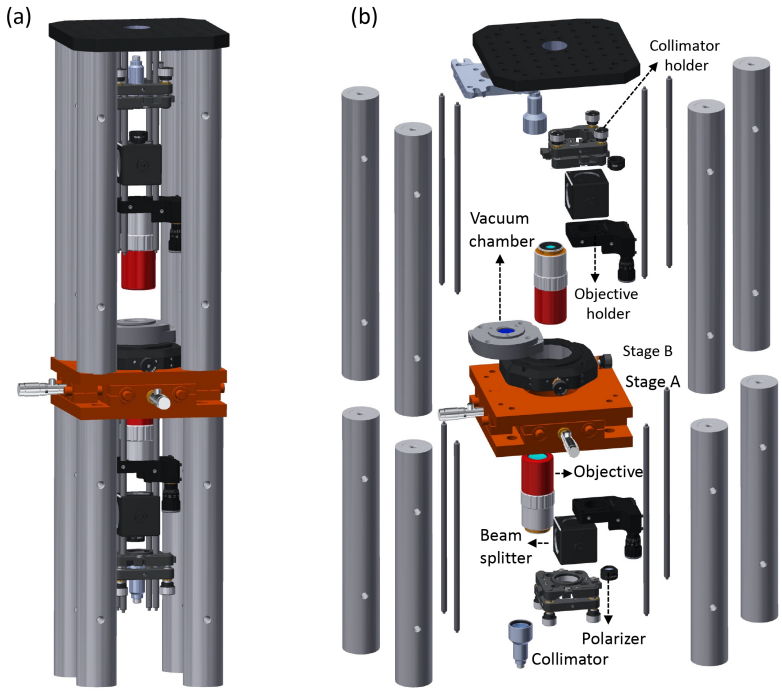

FIGURE 2.10: Design drawing of home-made microscope for measurements. (a) Side view, (b) exploded view.

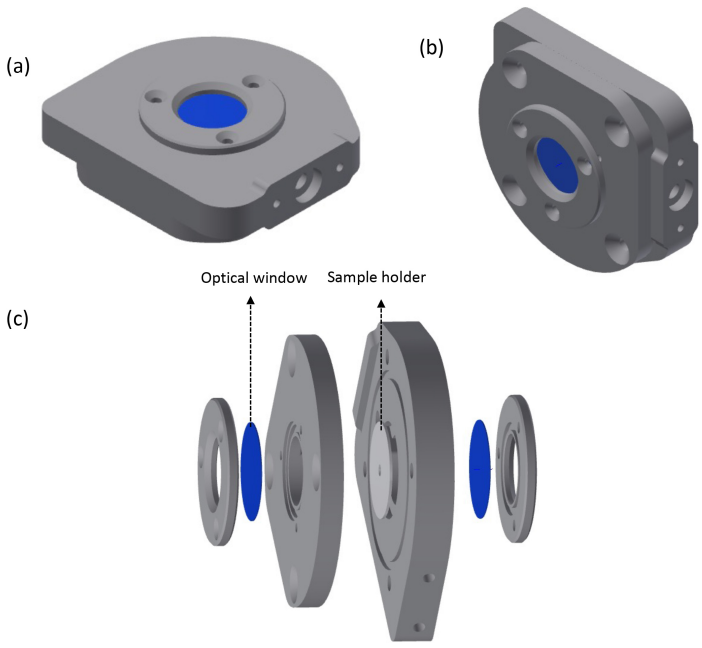

FIGURE 2.11: Design drawing of vacuum chamber (design by Damon Grimsey). (a) Top view, (b) side view, (c) exploded view.

by the outgassing of o-ring between upper and bottom parts, see Fig. 2.11(c). As the motion of mechanical resonator is damped by ambient air pressure (Measurement of oscillators on different air pressures can be found in Appendix C), it is necessary to put sample into a low pressure environment to improve the transducing efficiency). The transmitted laser is collected by a photodetector and the time-resolved signal is then analysed by spectral analyzer (Zurich Instruments-UHFLI) to give the mechanical modes information of nanomechanical metamaterial sample. For the setup in Fig. 2.9(b), a MEMS switch (AGILTRON - MEMS 22522B333) is added onto setup shown in Fig. 2.9(a) for swapping the incident light illumination directions between forward and backward illuminations, as light propagation direction is another dimension to optical control the natural Eigenfrequency and thermal motions of nanomechanical metamaterial sample(Chapter 4). To investigate asymmetric transmission in nanomechanical metamaterials, we upgrade the setup to realize pump-probe experiments, shown in Fig. 2.9(c) by adding a pump laser, an electro-optical modulator (EOM) and a tunable filter (EXFO - XTM50) onto the apparatus shown in Fig. 2.9(b). In the pump laser line, the EOM is employed to modulate pump laser frequency to against the mechanical Eigenfrequency of nanomechanical metamaterials. Pulsed pump and CW probe lasers are then go through the symmetric home-made column microscope(Fig 2.10). The transmitted pump laser is blocked by the tunable filter, and only probe laser that modulated by motion of mechanical oscillators in nanomechanical metamaterials is delivered into

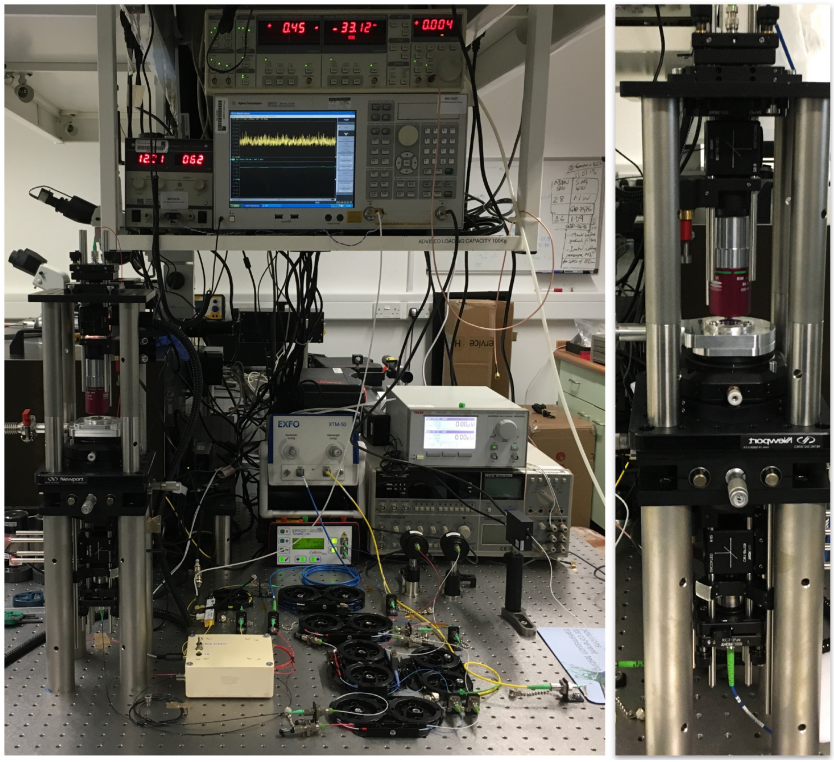

FIGURE 2.12: Photographs for experimental apparatus. Left: image of the entire setup. Right: zoom-in image of the home-made microscope.

InGaAs photodetector(Newport-1811) . The electrical signal is finally then sent to a electric network analyser (AGILENT-E5071C). In terms of the imaging system for optical path alignment, white light is diverted into the microscope by a pellicle beam splitters (Thorlabs, CM1-BP145B3), the sample and laser spot are imaged by a IR camera. A photograph of complete system is shown in Fig. 2.12.

2.3 Analytical descriptions

In this section, the interaction between light and dielectric nanomechanical metamaterials will be analytically modelled to interpret experimentally observed thermal motions behaviours and transmission asymmetry phenomena in fabricated samples.

Firstly, the mechanical properties of the nanomechanical metamaterials are studied, using Euler-Bernoulli theory to derive expressions for the Eigenfrequencies and mode-shapes of the doubly clamped beams, which is similar to the structures utilized in experiments. Then the fluctuation-dissipation theorem is applied to describe the thermal fluctuations of the components of nanomechanical metamaterials, that is relevant to chapter 3, 4 and 5.

Furthermore, the optical features of the nanomechanical metamaterials are investigated, in which temporal coupled mode theory is applied to describe the properties of Fano resonance. Also, the coupling effects between "bright" and "dark" modes are analysed for optimizing sample design processes.

2.3.1 Mechanical modes of doubly clamped beams

The mechanical modes investigated in this thesis are those of Si_3N_4 beams covered by a layer of Si. These beams have a large ratio of thickness in the direction of motion to length. Therefore, the flexural stiffness of the beams need to be taken into account[54], [55]. For the boundary conditions, I assume the beams are doubly clamped. In the following, I will firstly derive eigenfrequencies for beams governed by flexural stiffness in first subsection, and then modifications of eigenfrequencies induced by tensile stress within beams will be described in the second subsection.

Flexual vibrations of beams without axial tensile stress

Following the derivation by Weaver, Timoshenko and Young[55], we start from the equation of motion for a beam:

$$\frac{\partial^2}{\partial x^2}(EI\frac{\partial^2 U}{\partial x^2}) = -\rho A\frac{\partial^2 U}{\partial t^2} \tag{2.1}$$

with displacement $U(x,t)$, Young's modulus E, moment of inertia I, mass density ρ and cross section $A = w \times h$. If the beam is prismatic, i.e. has a constant cross section along its length(see Fig. 2.13), Young's modulus and moment of inertia are independent of x, reducing the equation to:

$$EI\frac{\partial^4 U}{\partial x^4} = -\rho A\frac{\partial^2 U}{\partial t^2} \tag{2.2}$$

If we assume a harmonic time dependence for the displacement, $U(x,t) = u(x)e^{-i\omega t}$, the spatial dependence $u(x)$ must satisfy the differential equation:

$$\frac{d^4 u(x)}{dx^4} = (\frac{\rho A}{EI})\omega^2 u(x) \tag{2.3}$$

Defining $\beta = (\rho A/EI)^{1/4}\omega^{1/2}$, and assuming a spatial dependence of the form $u(x) = exp(\kappa x)$, the general solution will have the form:

$$u(x) = Ae^{i\beta x} + Be^{-i\beta x} + Ce^{\beta x} + De^{-\beta x} \tag{2.4}$$

or in terms of real functions only:

$$u(x) = acos(\beta x) + bsin(\beta x) + ccosh(\beta x) + dsinh(\beta x) \tag{2.5}$$

Now, boundary conditions can be applied to the ends of the beam, which extends from $x = 0$ to $x = l$. Note that, for a given angular frequency ω, the spatial dependence of the displacement $u(x)$ is given by the 4^{th} order equation, so four boundary conditions are required for a unique solution. For doubly clamped beams, the beam displacement and bending at the endpoints are fixed to 0:

$$u(0) = u(l) = 0; \frac{du(z)}{dz(0)} = \frac{du(z)}{dz(l)} = 0 \tag{2.6}$$

The boundary conditions at $x = 0$ imply that $a = -c, b = -d$ and the boundary conditions at $x = l$ gives:

$$a(cos(\beta l) - cosh(\beta l)) + b(sin(\beta l) - sinh(\beta l)) = 0 \tag{2.7}$$

$$a(-sin(\beta l) - sinh(\beta l)) + b(cos(\beta l) - cosh(\beta l)) = 0 \tag{2.8}$$

The determinant of this problem is:

$$cos(\beta l)cosh(\beta l)) - 1 = 0 \tag{2.9}$$

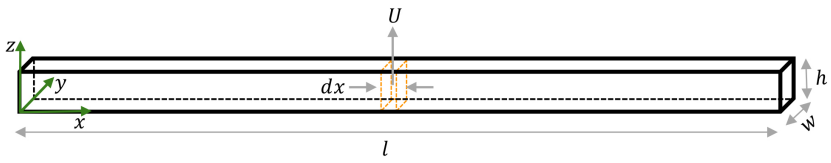

FIGURE 2.13: Sketch of beam geometry with length l and transverse displacement $U(x)$ due to forces along z and torques along y

This function is plotted in Fig. 2.14(a), showing zero-crossing locations, where $\beta_n l = 0, 4.73004, 7.8532, 10.9956, 14.1372...$, the solution $\beta l = 0$ is trivial and we discard it. The displacement is then given by:

$$\begin{aligned} u(x) &= a_n(cos(\beta_n x) - cosh(\beta_n x)) + b_n(sin(\beta_n x) - sinh(\beta_n x) \\ \frac{a_n}{b_n} &= \frac{cos(\beta l) - cosh(\beta l)}{sin(\beta l) - sinh(\beta l)} \end{aligned} \tag{2.10}$$

Therefore, the spatial displacement can be further written as:

$$\begin{aligned} u(x) = a_n[&(cos(\beta_n x) - cosh(\beta_n x)) \\ &+ \frac{sin(\beta_n l) - sinh(\beta_n l)}{cos(\beta l) - cosh(\beta l)}(sin(\beta_n x) - sinh(\beta_n x))] \end{aligned} \tag{2.11}$$

The corresponding eigenfrequency can be then given by:

$$\begin{aligned} \omega_n &= \sqrt{\frac{EI}{\rho A}}\beta_n^2 \\ f_n &= \frac{1}{2\pi}\sqrt{\frac{EI}{\rho A}}\beta_n^2 \end{aligned} \tag{2.12}$$

Where the moment of initial for the in-plane mode is $I_x = \frac{Ah^2}{12}$ and that for the out-of-plane modes is $I_y = \frac{Aw^2}{12}$. By substituting these moment initials into eq. 2.12 with the parameters of Si_3N_4 beams (see in table 2.2), the eigenfrequencies can be obtained. Table 2.3 shows analytical solutions and numerical FEM simulated eigenfrequencies for the first four leading in-plane and out-of-plane modes for comparison. One could see a very small differential (less than 1%) between analytical and FEM simulations on the Eigenfrequencies, verifying the correction of our derivation. Furthermore, these Eigenfrequencies can also be found at the zero crossings

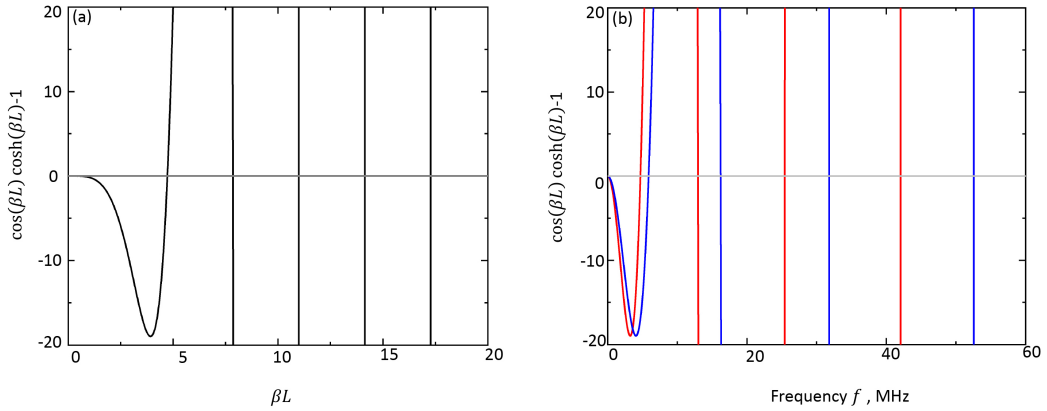

FIGURE 2.14: Searching for Eigenfrequency. (a) The function $cos(\beta l)cosh(\beta l) - 1$, whose zero crossings give the mode Eigenfrequencies for the doubly-clamped beam. (b) Eigenfrequencies of out-of-plane modes (the red curve) and in-plane modes (the blue curve) for a doubly-clamped Si_3N_4 beam with dimensions: $l = 20\mu m, w = 250nm$ and $h = 200nm$.

of red curves for out-of-plane modes and zeros crossings of blue curves for in-plane modes in Fig. 2.14.

TABLE 2.2: Parameters for Si_3N_4 utilized in this section

Properties \ Materials	Si_3N_4
Young's modulus (GPa)	260
$Density(Kg * m^{-3})$	3100
Thickness(nm)	200
Width(nm)	250
Length (μm)	20

TABLE 2.3: Eigenfrequencies of the first four leading in-plane and out-of-plane modes of a doubly clamped flexural Si_3N_4 beam with parameters showing in table 2.2. These Eigenfrequencies are calculated using eq. 2.12 and extracted from FEM simulations.

Properties \ Mode No.	1	2	3	4
$f_{n,out}(MHz)$(Analytical)	4.7069	12.9747	25.4357	42.0467
$f_{n,out}(MHz)$(FEM)	4.7073	12.9654	25.3871	41.9050
$f_{n,in}(MHz)$(Analytical)	5.8836	16.2184	31.7946	52.5584
$f_{n,in}(MHz)$(FEM)	5.8814	16.1910	31.6831	52.2553

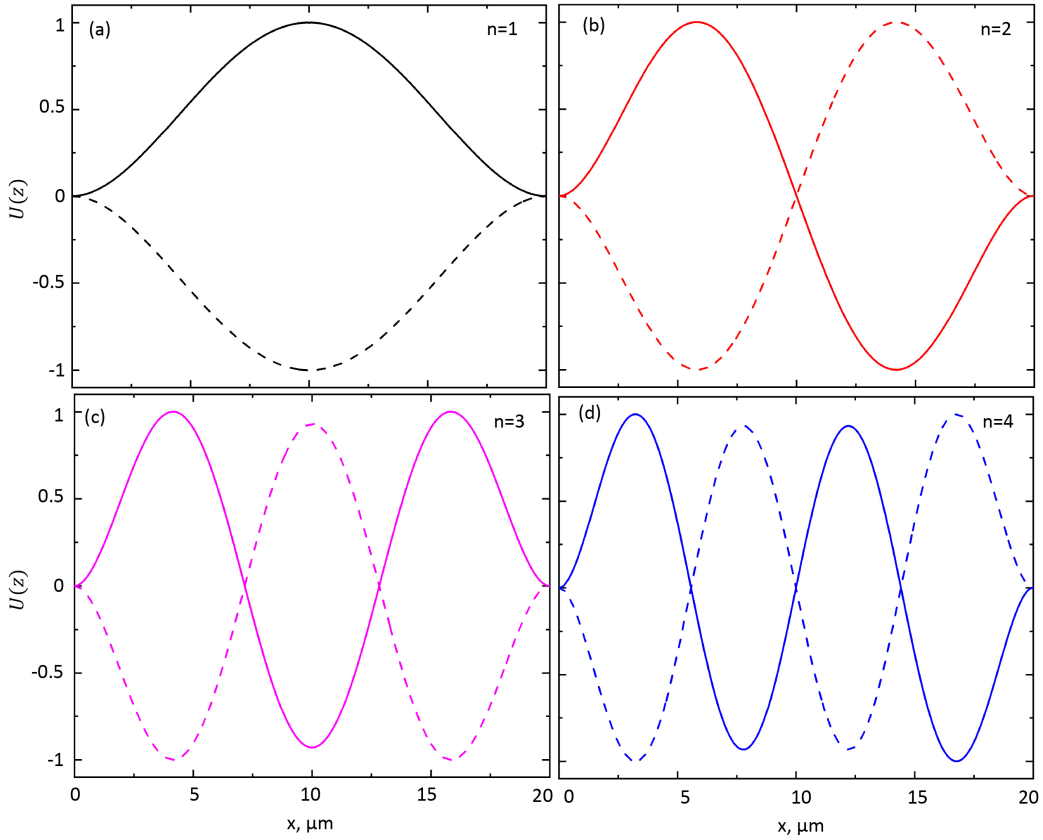

FIGURE 2.15: Mode profiles for the first four Eigenmodes of the doubly clamped beam shown in Fig. 2.14 with the maximum mode amplitude $Max(U_n(x))$ normalized to 1.

The spatial dependence for the lowest four solutions (n=1-4) for the double flexural beam are shown in Fig. 2.15 based on eq. 2.10.

Flexual vibrations of beams under influence of axial tension

So far, only the flexural restoring forces included in the previous section. In fact, as thin films conventionally utilized in nano-fabrication tend to have a process related tensile stress, such as materials deposition. Doubly clamped beams made of such thin films are therefore usually prestressed. A tensile stress σ increases the eigenfrequency and has to be taken into consideration by adding a term for the tensile force $F = \sigma A$ to governing differential equation (eq. 2.3)as follows[56], [57]:

$$\frac{d^4u(x)}{dx^4} - \frac{F}{EI}\frac{d^2u(x)}{dx^2} = (\frac{\rho A}{EI})\omega^2 u(x) \tag{2.13}$$

Which can be solved with doubly clamped boundary conditions at beam ends shown in eq. 2.6. The solved eigenfrequencies of beam can be expressed as:

$$\omega^2 = \frac{EI}{L^4}\left[\frac{\int_0^1(u''(\overline{x}))^2\mathrm{d}\overline{x}}{\int_0^1(u(\overline{x}))\mathrm{d}\overline{x}} + \frac{\sigma AL^2}{EI}\frac{\int_0^1(u'(\overline{x}))^2\mathrm{d}\overline{x}}{\int_0^1(u(\overline{x}))\mathrm{d}\overline{x}}\right] \tag{2.14}$$

Where $\overline{x} = x/L$ is the rescaled position along the beam's length, and the prime($'$) denotes differentiation with variation of $\overline{x}$.

The displacement of fundamental mode with tensile stress can then be written as:

$$\begin{aligned} u(x) =& a_1\big[(cos(\beta_1\overline{x}) - cosh(\beta_1\overline{x})) \\ &+ \frac{sin(\beta_1 l) - sinh(\beta_1 l)}{cos(\beta_1 l) - cosh(\beta_1 l)}(sin(\beta_1\overline{x}) - sinh(\beta_1\overline{x}))\big] \end{aligned} \tag{2.15}$$

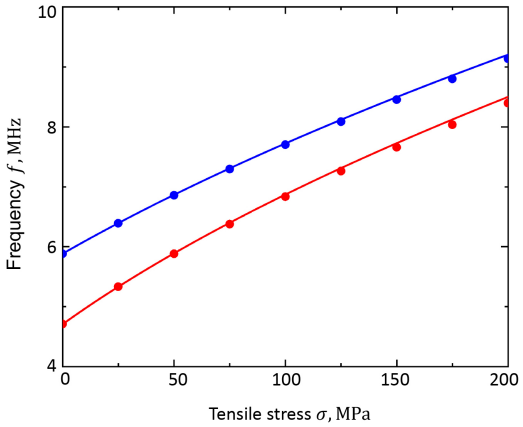

FIGURE 2.16: Eigenfrequencies for fundamental in-plane(blue) and out-of-plane(red) mechanical modes of a Si_3N_4 beam. Dots are value extracted from FEM simulations, lines are analytical calculations using eq. 2.17. Relevant parameters can be found in Table 2.2.

The eigenfrequency of fundamental mode with the influence from tensile stress can be expressed as:

$$f = \frac{\beta_1^2}{2\pi}\sqrt{\frac{EI}{\rho w h} + \frac{12.3\sigma}{\rho\beta_1^2}} \tag{2.16}$$

One can rewrite this as a function of the unstressed fundamental eigenfrequency f_0 to emphasize the contribution from axial stress to the eigenfrequency:

$$\begin{aligned} f &= 1.03\frac{t}{L^2}\sqrt{\frac{E}{\rho}\left(1 + \frac{\sigma L^2}{3.4Et^2}\right)} \\ &= f_0\sqrt{\left(1 + \frac{\sigma L^2}{3.4Et^2}\right)} \end{aligned} \tag{2.17}$$

Fig. 2.16 shows the eigenfrequencies as a function of tensile stress σ for a Si_3N_4 doubly-clamped beam with parameters given in Table 2.2. The tensile stress σ ranges from 0 to 200 MHz, as this range is the stress range of the membrane utilized for fabricating nanomechanical metamaterial samples. By comparing these analytical results based on eq. 2.17 with values extracted from FEM simulations. One can see a good agreement for both fundamental in-plane and out-of-plane modes at this stress range. Eq. 2.17 will be utilized in Chapter 3 and 4 to explain the observed experimental phenomena.

2.3.2 Thermalmechanical calibration

Nano-components, such as beams and cantilevers, of nanomechanical devices are capable of conducting many precise measurements due to their feature of high Q factors and fast operation speed, allowing potential applications in mass [58]–[60] or temperature sensing[61], torque or force transduction[62], [63] and even superconducting qubit observation[64]. Nanomechanical metamaterials can further facilitate the performance of such devices via optical resonances. With the decrease of the size of nanomechanical components, calibration process of the motion of such devices could be a challenge task. However, there is a powerful approach where the motion of these nano-components can be calibrated via observation of their random thermal motion. This method also acknowledged as thermomechanical calibration.

Motions of a nanomechanical resonator

The components of nanomechanical metamaterials are investigated in this thesis are doubly-clamped beams, also known as bridges. So the nanomechanical resonator to be investigated here is a bridge. Generally, the complete, three-dimensional motions described by a displacement function $\vec{R}(\vec{x}, t)$, that can be decomposed into an infinite number of independent modes. Each mode is labelled in n. However, it usually can be reduced to a one-dimensional displacement function $Z(x, t)$ for a nanomechanical

resonator, like the bridge investigated in this thesis. This displacement function $Z(x,t)$ can be expressed as:

$$Z(x,t) = \sum_n Z_n(x,t) = \sum_n z_n(t)u_n(x) \tag{2.18}$$

where $u_n(x)$ is the one-dimensional mode profile of the n^{th} mode of bridge, and that has been analytically derived in the eq. 2.11 in Section 2.3.1. $z_n(t)$ is a function that describes the time dependence of the bridge's thermal motion. Furthermore, we choose to normalize $u_n(x)$ with maximum value of $|u_n(x)|$. So $z_n(t)$ has units of distance and it corresponds to the true physical displacement for measured bridges. And the thermal motion of bridges $z_n(t)$ can be expressed by Langevin equation[54]:

$$\ddot{z} + 2\pi\gamma\dot{z} + \omega_n^2 z = \frac{F_{th}(t)}{m_{eff,n}} \tag{2.19}$$

where $F_{th}(t)$ is the time dependent thermal force experienced by the oscillator related to the dissipation factor γ through fluctuation-dissipation theorem, $m_{eff,n}$ is the effective mass and its general expression will be discussed in the next section. $\omega_n = 2\pi f_n$ is the n^{th} angular eigenfrequency of oscillation(the expression for simple bridge shape can be found in eq. 2.17), f_n is the Eigenfrequency. The resonance Q factor is defined as $Q = f_n/\gamma$ in the limit of small damping.

Effective mass

The effective mass of each mode of a bridge can be determined by its potential energy. For a specific mode, the potential energy $\mathrm{d}E_p$ for a small volume element $\mathrm{d}V$, centering at x with a mass element $\mathrm{d}m = \rho(x)\mathrm{d}V$ can be expressed by[65]:

$$\begin{aligned} \mathrm{d}E_p &= \frac{1}{2}k|U(x,t)|^2 = \frac{1}{2}\omega_n^2 \mathrm{d}m|U(x,t)|^2 \\ &= \frac{1}{2}\omega_n^2|z_n(t)|^2\rho(x)|u_n(x)|^2\mathrm{d}V \end{aligned} \tag{2.20}$$

The total potential energy of the mode can be given by:

$$\begin{aligned} E_p &= \frac{1}{2}\omega_n^2|z_n(t)|^2 \int \rho(x)|u_n(x)|^2\mathrm{d}V \\ &= \frac{1}{2}\omega_n^2|z_n(t)|^2 m_{eff} \end{aligned} \tag{2.21}$$

where we define effective mass m_{eff}[66], [67]:

$$m_{eff} = \int \rho(x)|u_n(x)|^2\mathrm{d}V \tag{2.22}$$

It need to be noticed that in first subsection of section 2.3.2 the time-dependent displacement function $z_n(t)$ is defined as the motion of a device at its point of maximum amplitude by virtue of the normalization condition for $z_n(x)$. Eq. 2.22

corresponds to the effective mass for a point-like measurement taken at this position of maximum displacement. For a point-like measurement at some other position on the bridge, effective mass in Eq. 2.22 need to be modified by dividing by maximum value of $|u_n(x_0)|$. Hence, a more general definition of the effective mass is expressed as:

$$m_{eff} = \frac{\int \rho(x)|u_n(x)|^2 \mathrm{d}V}{|u_n(x_0)|^2} \tag{2.23}$$

where $|u_n(x)|$ have the maximum value at position of x_0. For the fundamental mode of a bridge, the maximum value of $|u_1(x)| = |u_1(L/2)|$. Therefore the effective mass of the bridge at the fundamental mode can be expressed as:

$$m_{eff} = \frac{\int_0^L \rho(x)|u_1(x)|^2 \mathrm{d}V}{|u_1(L/2)|^2} \tag{2.24}$$

one could obtain the effective mass of the bridge utilized in section 2.3.1 at fundamental frequency based on normalized mode profile $u_1(x)$ in Fig. 2.15(a) and the parameters in table 2.2:

$$m_{eff} = 0.4whl\rho = 0.4m_{phys} \tag{2.25}$$

where $m_{phys} = whl\rho$ is the physical mass of the beam.

Power spectral density

In Chapter 3, the measured time-varying signals from the motion of a resonator are transformed into the frequency domain, giving a spectral representation of the bridges' motion, peaked at their resonance frequency. By squaring this spectrum and dividing by the resolution bandwidth of the instrument, experimentally measured one-sided power spectral density (PSD) $S_{zz}(\omega)$ of the signal is produced.

The measured time averaged motion need to be related to its thermal energy to calibrate a mechanical resonator, In order to do so, the equipartition theorem is utilized to express mean-square amplitude for the motion of bridge $< u_n^2(t) >$ in terms of its thermal noise PSD. In this section, a theoretical expression is derived for PSD corresponding to a damped harmonic oscillator experiencing random thermal bath. And it can be applied to calibrate thermal PSD data for any nanomechanical resonators.

Starting with a autocorrelation function $R_{zz}(t)$, which indicates how the measured signal $z_n(t')$ is related to itself later at time of $t' + t$[65], [68]:

$$R_{zz}(t) = \lim_{T_0 \to \infty} \frac{1}{T_0} \int_0^{T_0} z_n(t') z_n(t'+t) \mathrm{d}t' \tag{2.26}$$

The two-sided PSD function $P_{zz}(\omega)$, that span all frequencies both positive and negative, can be obtained from the Fourier transform of the autocorrelation function:

$$P_{zz}(\omega) = \int_{-\infty}^{\infty} R_{zz}(t) e^{i\omega t} \mathrm{d}t \tag{2.27}$$

The autocorrelation function can then be produced via inverse Fourier transform:

$$R_{zz}(t) = \frac{1}{2\pi} \int_{-\infty}^{\infty} P_{zz}(\omega) e^{-i\omega t} \mathrm{d}\omega \tag{2.28}$$

For the real-measured signal, only positive frequencies have physical meaning. Hence, $S_{zz}(\omega)$ is introduced, which is defined on the frequency interval from 0 to ∞, and it produces the power in the signal when integrated over all positive frequencies. $S_{zz}(\omega)$ is related with $P_{zz}(\omega)$ by $S_{zz}(\omega) = 2P_{zz}(\omega)$[69]. This relation allows the total power in the signal to be conserved when each spectral density function is integrated over the frequency interval on which it is defined. In the rest of the derivation, $S_{zz}(\omega)$ will be used, as it provides a theoretical spectral density that can be fit directly to experimental data.

We define the quantity known as the mean-square amplitude of our signal as[68]:

$$< z_n^2(t) >= \frac{1}{T_0} \int_0^{T_0} \left[z_n(t) \right]^2 \mathrm{d}t \tag{2.29}$$

On the other hand, Using eq.2.28, along with the relation between $S_{zz}(\omega)$ and $P_{zz}(\omega)$, $< z_n^2(t) >$ can be expressed in terms of its PSD via:

$$< z_n^2(t) >= \frac{1}{2\pi} \int_0^{\infty} S_{zz}(\omega) \mathrm{d}\omega \tag{2.30}$$

By doing Fourier transformation of eq. 2.19, one can connect $S_{zz}(\omega)$ to $S_{FF}(\omega)$, which is the PSD:

$$S_{zz}(\omega) = |\chi(\omega)|^2 S_{FF}(\omega) \tag{2.31}$$

and susceptibility $\chi(\omega)$ can be expressed as[70]:

$$\chi(\omega) = \frac{1}{m_{eff,n}(\omega_n^2 - \omega^2 - i\omega\omega_n/Q_n)} \tag{2.32}$$

For thermomechanical calibration, $S_{FF}(\omega)$ can be replaced by a constant thermal force noise S_{FF}^{th} and this factor can be determined by combining eqs.2.30–2.32, which results in

$$< z_n^2(t) >= \frac{S_{FF}^{th}}{2\pi m_{eff,n}^2} \int_0^{\infty} \frac{\mathrm{d}\omega}{(\omega^2 - \omega_n^2)^2 + (\omega\omega_n/Q_n)^2} \tag{2.33}$$

Combining the result from eq. 2.33 with the equipartition theorem, in which[71]:

$$\frac{1}{2}m_{eff,n}\omega_n^2 < z_n^2(t) >= \frac{1}{2}\kappa_B T \tag{2.34}$$

one could derive the thermal force noise constant S_{FF}^{th} as:

$$S_{FF}^{th} = \frac{4\kappa_B T\omega_n m_{eff,n}}{Q_n} \tag{2.35}$$

giving the expression of oscillator PSD as :

$$S_{zz}(\omega) = \frac{4\kappa_B T\omega_n}{m_{eff,n}Q[(\omega^2-\omega_n^2)^2 + (\omega\omega_n/Q_n)^2]} \tag{2.36}$$

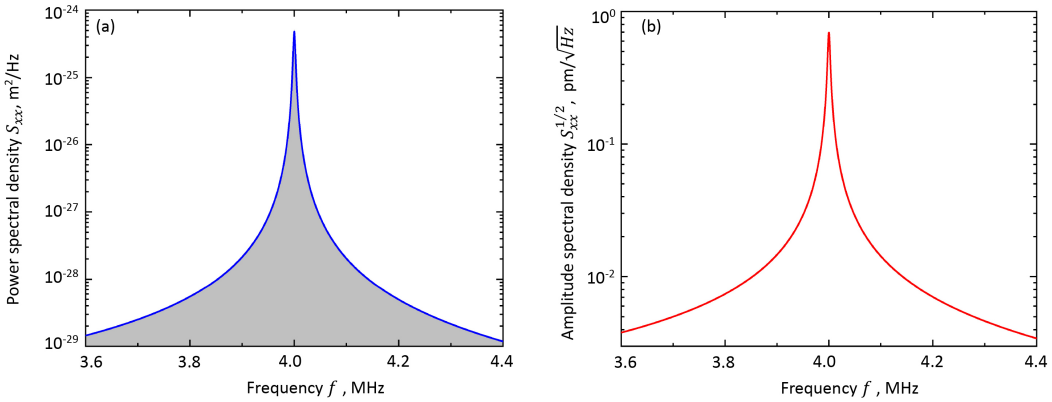

FIGURE 2.17: Power spectral density of a mechanical oscillator with $\omega_n = 2\pi\times 4MHz$, $Q_n = 1000$ and $m_{eff,n} = 2pg$. (a)Power spectral density as a function of frequency. Integration of the power spectral density $S_{zz}(f)$, indicated by the grey shading, gives mean-square amplitude $< z_n^2(t) >= 3.27\times 10^{-21}m^2$. (b)Same data as (a) but plotted as amplitude spectral density(ASD) $s_{zz}(f) = S_{zz}(f)^{1/2}$, as it is a conventional way to present.

Where k_B is the Boltzmann constant, T is temperature, $\omega_n = \sqrt{k/m_{eff,n}}$ is the n^{th} of Eigenfrequency of an oscillator, $m_{eff,n}$ is the effective mass of the bridge, Q_n is the quality factor of the resonant mode.

This equation can be plot in Fig. 2.17 for a group of typical parameter taking from nanomechanical oscillator in Chapter 3: $\omega_1 = 2\pi\times 4\ MHz$, $Q = 1000$ and $m_{eff,1}$ =2 pg.

The mean-square amplitude $< z_n^2(t) >$ can be calculated by integrating S_{xx} in the shadow area of Fig. 2.17(a)based on eq. 2.30, which gives $< z_n^2(t) >= 3.27\times 10^{-21}m^2$ and the root-mean-square (RMS) displacement $< z_n(t) >$ is define as:

$$\begin{aligned} < z_n(t) >= \sqrt{< z_n^2(t) >} &= \sqrt{\frac{1}{2\pi}\int S(\omega)d\omega} \\ &= \sqrt{\frac{1}{2\pi}\int s(\omega)^2 d\omega} \end{aligned} \tag{2.37}$$

$s(\omega)$ shown in eq. 2.37 is defined as amplitude spectra density (ASD), which is a conventional way to present and will be used in the following chapters. And the RMS displacement $< z_n(t) >= 57.1pm$ can be evaluated from eq. 2.37 for the PSD and ASD shown in Fig. 2.17(a) and (b) respectively.

2.3.3 Fano resonances

The mechanical properties of the nano-components of nanomechanical metamaterials are investigated in Section 2.3.1 and 2.3.2, now I turn to the optical aspect of nanomechanical metamaterials. As the nanomechanical metamaterial sample in Chapter 5 is efficiently driven by optical forces, which strongly enhanced by Fano resonances, it is necessary to give a basic concepts on Fano resonance. Analytical descriptions of Fano resonances are given as following.

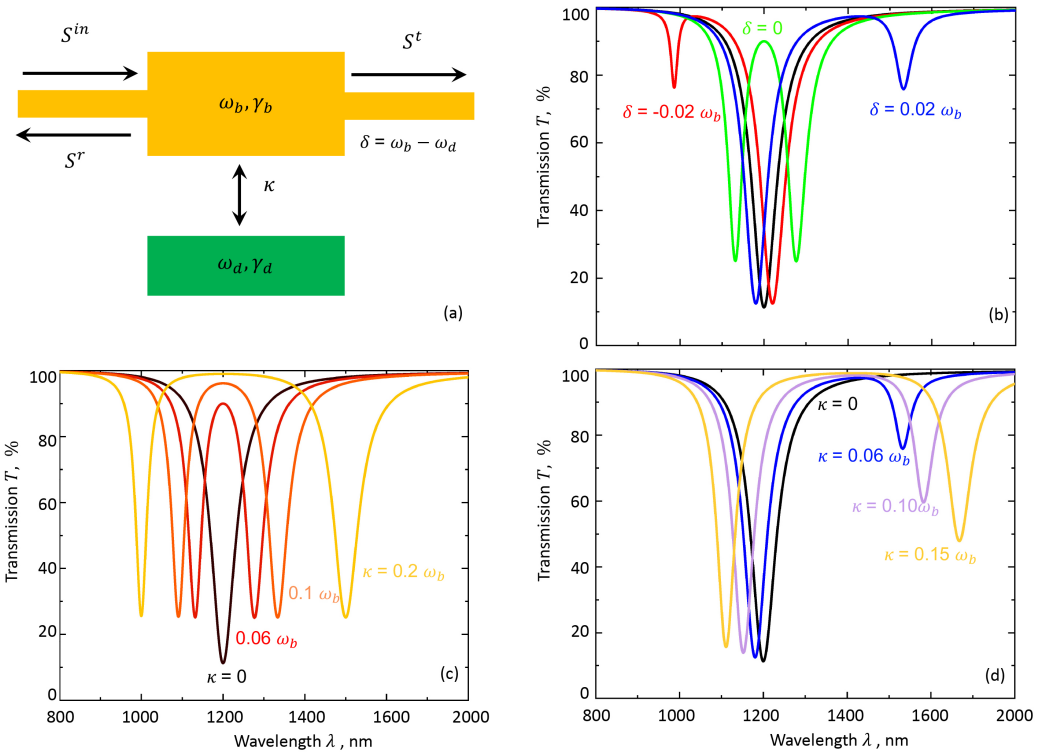

FIGURE 2.18: Fano resonance described by temporal coupled mode theory. (a) Schematics of the simplest Fano resonant system described by eq. 2.38. The two resonators, "bright" and "dark", are coupled to each other with coupling coefficient κ, and the "bright" resonator (orange) is coupled to an input/output port that represents incident, reflected, and transmitted light; (b)Transmission spectra of the Fano-resonant system described by eq. 2.40 with finite Ohmic losses. The curves correspond to the cases of Fano resonance with $\sigma = 0.02\omega_b$(blue curve) and $\sigma = -0.02\omega_b$ (red curve) and electromagnetically induced transparency (EIT) $\sigma = 0, \omega_b = \omega_d$ (green curve) and $\kappa = 0.05\omega_b$ for these three curves; also, $\kappa = 0$ (black curve) indicates the case without coupling and the Eigen-wavelength of "bright" mode: λ=$\omega_b/2\pi = 1200nm$; (c) transmission spectra of EIT type of resonance with different coupling coefficient κ; (d) typical Fano type with different coupling coefficient κ, and this kind of line shape is relevant to our experimental measured spectra of fabricated nano-opto-mechanical metamaterials.

Fano resonance occurs from the interference between a spectrally broad "bright mode" that strongly couples to incident light and a sharp "dark mode" with low radiative loss. This concept of Fano resonances can be described by temporal coupled mode theory[72], [73]. A conceptual schematic can be found in Fig. 2.18(a), where a "bright" resonator with natural angular frequency ω_b is coupled to incident light (S^{in}) directly, while the "dark" resonator with natural angular frequency ω_d indirectly interacts with the light via coupling to the "bright" resonator. Such layout corresponds to metamaterials, in which near-field interactions among neighbouring metamolecules are responsible for the coupling between these two resonances. Since these two resonators are coupled to far-field radiation in a different way, they possess different damping rate $\gamma_b \gg \gamma_d$. The dynamics of these two coupled resonators could be described by the equations of temporal coupled mode theory[72], [73]:

$$\begin{aligned} \dot{b} - j\left(\omega_b + j\gamma_b\right) b + j\kappa d &= \alpha_b S^{in} e^{j\omega t} \\ \dot{d} - j\left(\omega_d + j\gamma_d\right) d + j\kappa b &= 0 \end{aligned} \tag{2.38}$$

where b and d are the field amplitudes in the "bright" and "dark" resonators, respectively, α_b is coupling strength of the "bright" resonator to incident light. S^{in} and ω are amplitude and angular frequency of the incident light, respectively. κ is the coupling strength between the resonators. The reflection(r) and transmission(t) coefficient can be expressed as[72]–[74]:

$$\begin{aligned} r &= \frac{|\alpha_b|^2 j(\omega - \omega_d - j\gamma_d)}{(\omega - \omega_b - j\gamma_b)(\omega - \omega_d - j\gamma_d) - \kappa^2} \\ t &= 1 + r \end{aligned} \tag{2.39}$$

The system reflection and transmittance can be found as following:

$$\begin{aligned} R = |t|^2 &= \left| \frac{|\alpha_b|^2 j(\omega - \omega_d - j\gamma_d)}{(\omega - \omega_b - j\gamma_b)(\omega - \omega_d - j\gamma_d) - \kappa^{\,2}} \right|^2 \\ T = |t|^2 &= \left| 1 + \frac{|\alpha_b|^2 j(\omega - \omega_d - j\gamma_d)}{(\omega - \omega_b - j\gamma_b)(\omega - \omega_d - j\gamma_d) - \kappa^{\,2}} \right|^2 \end{aligned} \tag{2.40}$$

In metamaterials, the intrinsic Ohmic losses and radiation losses need to be taken into consideration. The total losses of the system can be expressed as $\gamma = \gamma^o + \gamma^r$. γ^o is non-radiative decay rate introduced by Ohmic losses, γ^r is radiative decay rate.

Fig. 2.18(b) shows typical transmission spectra of Fano model based on eq. 2.40 for different values of the spectral detuning $\sigma = \omega_b - \omega_d$. The black curve in Fig. 2.18(b) shows the case without coupling ($\kappa = 0$), e.g., the Eigenmode of "bright" resonator. In order to conveniently compare the analytical results to the experimental observation, all of the transmission spectra are plotted in wavelength domain. Here, the Eigen-wavelength λ_b of "bright" resonator is set as λ_b =1200 nm (corresponding angular eigenfrequency $\omega_b = 2\pi c/\lambda_b$). The spectral detuning between "bright" and

"dark" resonator is set as $\sigma = 2\pi c/\delta_\lambda$ and δ_λ =300 nm, 0 nm, 300 nm, showing in blue, green and red curves in Fig. 2.18(b). One could see strong asymmetric line shapes, indicating the Fano interference between these two resonators. In particular, the Fano resonance is referred to as electromagnetically induced transparency(EIT) when $\omega_b = \omega_d$ (green curves). Two dips in the transmission spectra for the case of $\sigma \neq 0$ (red and blue) corresponds to the Eigen-frequency of "bright" and "dark" resonators.

In addition, the influences of coupling efficient κ on transmission spectra for Fano resonances are also investigated in Fig. 2.18(c) and (d) for the EIT and a typical Fano line shape. The transparency window for the EIT case is broaden and the transmittance of this window is also grown with the increase of the coupling coefficient κ. In Fig. 2.18(d), the separation between "bright" and "dark" modes goes up and both Q-factor and transmittance for dark mode decrease with the increase of κ.

The aim of above analytical model is to gain a better understanding of experimental observed transmission spectra, such as the spectra shown in Fig. 2.7. Fig. 2.19(a) shows the sketch of experiment setup. The measured transmission spectrum

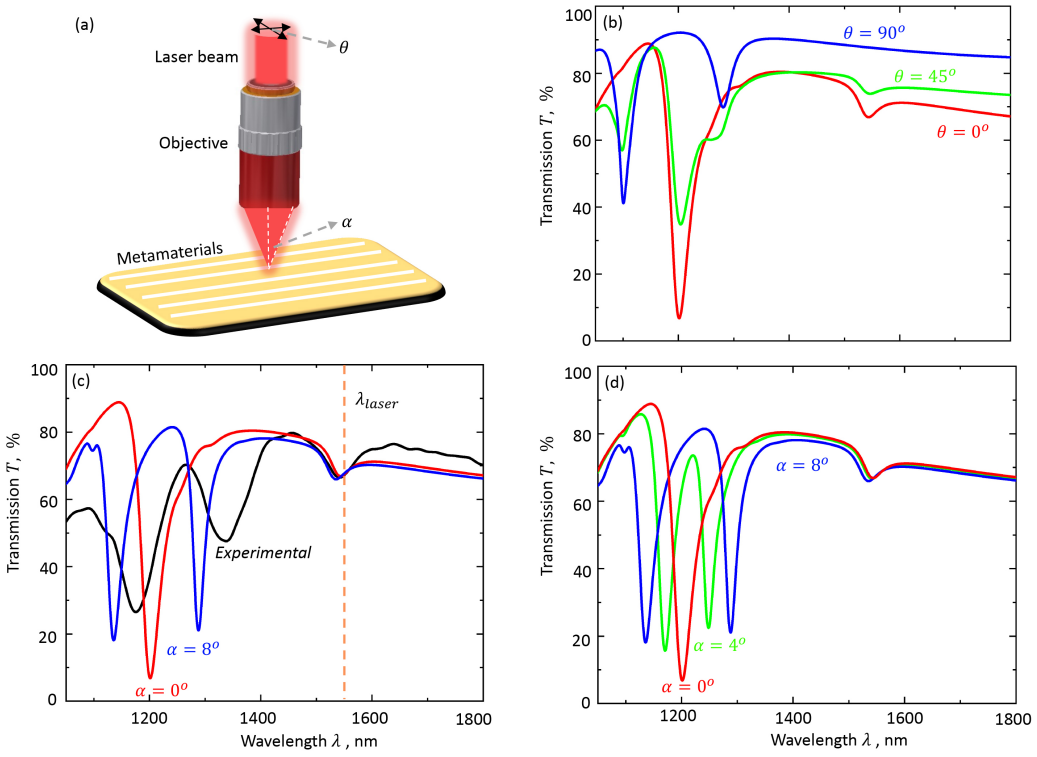

FIGURE 2.19: Investigation the influences from polarization θ and incident angle α of light on transmission spectra. (a) Sketch of experimental setup, $\theta = 0^o$ means the polarization of light parallel to the Si_3N_4 beam. (b) Transmission spectra for different polarization angles $\theta = 0^o, 45^o, 90^o$. (c) Comparison between experimental outcomes (black curve) and analytical solutions, indicating the split for the resonance at short wavelength mainly originating from the oblique incident angle generated by high NA objective. (d) Transmission spectra for different incident angles $\alpha = 0^o, 4^o, 8^o$.

of a nanomechanical metamaterials is plotted in a black curve in Fig. 2.19(c). By comparing it to spectra shown in Fig. 2.18(d), one could confirm that the shallow dip in the long wavelength corresponding to the eigen-wavelength of the "dark" resonator. However, the "bright" mode splits into two dips. The reasons for this observation could potentially come from the misalignment of polarization angle (θ) of incident light or the incident angle (α) induced by high numerical apparatus (NA) objective. The numerical modelling outcomes for investigating the impact from polarization and incident angle of light on transmission spectra shown in Fig. 2.19(b) and (d) correspondingly. It can be seen that the polarization angle could not introduce observable resonance splitting within a small offset of polarization angle introduced during experiments. In contrast, 8^o incident angle (corresponding to the NA =0.28 of the objective utilized) is enough to produce pronounced dip splitting on the "bright" mode. So the splitting of the dip corresponding to "bright" mode observed originates from the incident angle introduce by the objective. It is worth to note that the "dark" mode is not significantly impacted by the incident angle. As the "dark" mode is what the following experimental chapters really focus on and it is insensitive to the incident angle, I will just show part of transmission spectrum corresponding "dark" mode of the metamaterials in Chapter 3, 4 and 5.

2.4 Computational methods

This section described the approaches used to numerically model the optical properties of nanomechanical metamaterials. The electromagnetic response was simulated by solving three dimensional Maxwell equations using finite element method (FEM). The solver applied for conducting FEM simulations was the commercial software COMSOL Multiphysics 5.4.

Fig. 2.20 gives a typical geometry that was used to model the optical properties of nanomechanical metamaterials. This geometry consists of a single unit cell, in which a metamolecule at the origin and the free-space is in the area above and below the metamolecule. Periodical boundaries are applied in the $x-$ and $y-$ directions, indicating that the metamaterial are simulated as being infinitely large. The boundaries at each ends of the simulated area are modelled as scattering boundaries. One of two ports can be utilized to launch the incident electromagnetic wave from one sides of the metamaterials, this port can also record the reflected wave. The other is employed to record the transmitted wave. Perfect matched layers, located in between scattering boundary and ports, can be utilized to absorb the wave passing through the ports without any reflections. The transmission and reflection of the nanomechanical metamaterials was calculated via integrating the Poynting vector over the corresponding ports. Simulated electric, magnetic field and displacement current over the metamolecule can be evaluated for multipole decomposition (see section: 2.4.1)and optical forces (section: 2.4.2) calculation. Different optical response of various materials can be modelled by complex refractive index of refraction.

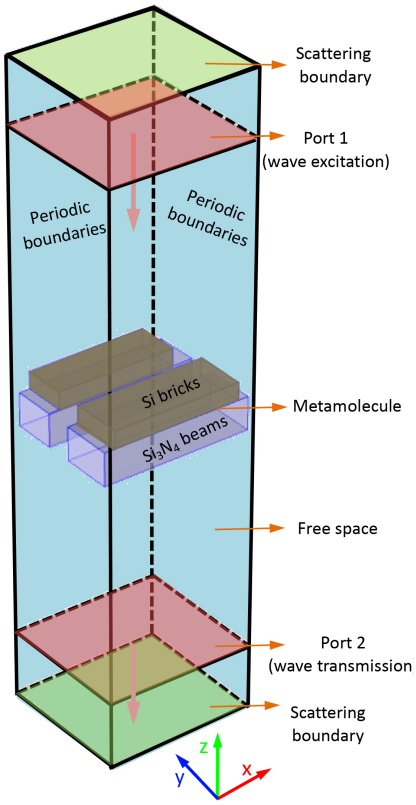

FIGURE 2.20: Numerical modelling of optical response of nanomechanical metamaterials in COMSOL Multiphysics. A typical shape that was utilized to simulated electromagnetic response of nanomechanical metamaterials, the size of the metamaterials was assumed to be infinite, therefore, only the response of a single metamolecule needed to be simulated with periodic boundaries. The simulated shape consist of a long free-space tunnel with a single metamolecule in the middle. Ports conditions is utilized to excite and receive the plane wave at the ends of this tunnel. A pair of perfect matched layer located in between scattering boundary and port are utilized absorb the high-order scattered wave.

The accuracy of simulated solutions can be verified by comparing it with the experiment data and by changing the mesh size (e.g. finite element size). If simulated and experimental data match well or If the decrease of mesh size did not change the optical response of the metamaterials, one could conclude that the numerical solution is near to the ground truth.

2.4.1 Multipole decomposition

The electromagnetic properties of a material are determined by the effective macroscopic parameters, the permittivity and permeability, which build a connection between its macroscopic electromagnetic response and microscopic charge-current excitations induced in the atoms or molecules of materials[75]. This effective medium theory can also be utilized to describe the properties of metamaterials. However, it is a challenge task to obtain the effective materiasl parameters due to their structural inhomogeneity and strong spatial dispersion[76].

Alternatively, multipole decomposition of the charge-current of the unit cell of metamaterials, directly linking to the transmission and reflection of the metamaterials. A similar problem of calculating the scattered radiation from arrays of metallic resonators has been addressed in the past using the fast multipole method[77], [78], and periodic Green's functions for the Helmholtz equation[79]. However, the distinct feature of the method based on Savinov's frame work is that the expressions derived are suitable both for numerical calculations[80](shown in Chapter 5 and 6) and analytical evaluation (shown in Appendix A).

Here, displacement currents $\vec{J}$ inside meta-molecule are evaluated from the FEM simulation, which are then employed in a multipole decomposition based on the methodology presented in [80]. The definition of first six leading multipole moments can be find as following($\alpha, \beta, \gamma = x, y, z$):

$$p_\alpha = \frac{1}{i\omega_0} \int d^3r \; J_\alpha \tag{2.41}$$

$$m_\alpha = \frac{1}{2c} \int d^3r \; \left[\vec{r} \times \vec{J}\right]_\alpha \tag{2.42}$$

$$T_\alpha = \frac{1}{2c} \int d^3r \; \left[\left(\vec{r} \bullet \vec{J}\right) r_\alpha - 2r^2 J_\alpha\right] \tag{2.43}$$

$$Q^{(e)}_{\alpha\beta} = \frac{1}{i2\omega_0} \int d^3r \; \left[r_\alpha J_\beta + r_\beta J_\alpha - \frac{2}{3}\delta_{\alpha,\;\beta}\left(\vec{r} \bullet \vec{J}\right)\right] \tag{2.44}$$

$$Q^{(m)}_{\alpha\beta} = \frac{1}{3c} \int d^3r \; \left[\vec{r} \times \vec{J}\right]_\alpha r_\beta + \{\alpha \leftrightarrow \beta\} \tag{2.45}$$

$$O^{(e)}_{\alpha\beta\gamma} = \frac{1}{i6\omega_0} \int d^3r \left[J_\alpha \left(\frac{r_\beta r_\gamma}{3} - \frac{1}{5} r^2 \delta_{\beta,\;\gamma}\right) + r_\alpha \left(\frac{J_\beta r_\gamma}{3} + \frac{r_\beta J_\gamma}{3} - \frac{2}{5}\left(\vec{r} \bullet \vec{J}\right)\delta_{\beta,\;\gamma}\right)\right] + \{\alpha \leftrightarrow \beta, \gamma\} + \{\alpha \leftrightarrow \gamma, \beta\} \tag{2.46}$$

Where p_α is electric dipole, m_α is magnetic dipole, T_α is toroidal dipole, $Q^{(e)}_{\alpha\beta}$ is electric quadrupole, $Q^{(m)}_{\alpha\beta}$ is magnetic quadrupole and $O^{(e)}_{\alpha\beta\gamma}$ is electric octupole moments, c is the speed of light in vacuum, ω_0 is angular frequency in free-space. A shorthand has been utilized to improve clarity. For example, $\int d^3r \; \left[\vec{r} \times \vec{J}\right]_\alpha r_\beta + \{\alpha \leftrightarrow \beta\} \equiv \int d^3r \; \left[\vec{r} \times \vec{J}\right]_\alpha r_\beta + \int d^3r \; \left[\vec{r} \times \vec{J}\right]_\beta r_\alpha$, i.e., the second term is obtained from the first term, with the exchanged positions of indices α and β. In the case of electric octupole $O^{(e)}_{\alpha\beta\gamma}$, for example, $\{\alpha \leftrightarrow \beta, \gamma\}$ obtained from the first term by exchanging α and β while leaving γ untouched.

2.4.2 Optical forces calculation

Based on classical electrodynamics, the components of total time average force F acting on a metamaterial illuminated with light can be calculated using a surface integral[75]:

$$\langle F_i \rangle = \iint_S \langle T_{ij} \rangle \, n_j \, dS \tag{2.47}$$

Where S is a bounding surface around the metamolecule, n_j is the unit vector pointing out of the surface and T_{ij} is the time-averaged Maxwell stress tensor defined by:

$$\langle T_{ij} \rangle = \frac{1}{2} Re \left[\epsilon\epsilon_0 \Big(E_i E_j^* - \frac{1}{2}\delta_{ij}|E|^2 \Big) + \mu\mu_0 \Big(H_i H_j^* - \frac{1}{2}\delta_{ij}|H|^2 \Big) \right] \tag{2.48}$$

The stress tensor integral eq. 2.48 encompasses both the radiation pressure and near-field gradient force. However, it does not include Casimir forces, which originate vacuum quantum fluctuation and it exists in the absence of illumination[81].

Radiation pressure arises through transfer of momentum between photons and any object. It depends on the reflection R and absorption A coefficients of the surface according to the equation $F_r = (2R + A)P/c$[82], where P is the power of incident light, and assumes a maximum value of $2P/c$ when the reflectivity of a surface is 100%.

In this thesis, forces acting on metamaterial structures are evaluated via the Maxwell stress tensor integral Eq. 2.47 with electric E and magnetic H field distributions obtained from Comsol MultiPhysics 5.4 as mentioned before. Unless there is an additional claim, the refractive index of Si I used in simulations is set as 3.5 with variable extinction coefficient to evaluates the influences from materials losses. Refractive index of Si_3N_4 is set as 2 and the losses are excluded. The normal incidence condition is assumed in all of calculations in the following chapter. The surface integration S was defined as a surface of rectangular enclosing the meta-molecule.

Chapter 3

Thermal fluctuations of the optical properties of nanomechanical photonic metamaterials

In this chapter, the influence from thermal fluctuations on the optical properties of nanomechanical photonic metamaterials will be investigated. The combination of optical and mechanical resonances offers strong hybrid nonlinearities, bistability and the ability to efficiently control the optical response of nanomechanical photonic mechanical metamaterials with electric and magnetic field. While optical resonances can be characterized in routine transmission and reflection experiments, mapping the high frequency mechanical resonances of complex metamaterial structures is challenging. Here we report that high-frequency time-domain fluctuations of the optical transmission and reflection spectra of nano-opto-mechanical metamaterials are directly linked to thermal motion of their components and can give information on the fundamental mechanical frequencies and damping of the mechanical modes. We demonstrate this by analyzing time-resolved fluctuations of the transmission and reflection of dielectric and plasmonic nanomembrane metamaterials at room temperature and low ambient gas pressure. These measurements reveal complex mechanical responses, understanding of which is essential for optimization of these functional photonic materials. At room temperature the magnitude of metamaterial transmission and reflection fluctuations is broadly on the scale of 0.1% but may exceed 1% at optical resonances.

3.1 Introduction

The thermal vibration frequencies of components of nanomechanical devices increase as objects decrease in size and the amplitude of such oscillations becomes increasingly important. In nanomechanical devices, they are of picometric scale in the mega- to gigahertz range and add noise to induced controlled movements that underpin the functionality. For example, thermal vibrations in nanomechanical photonic metamaterials [14] result in small fluctuations of their optical properties and may perturb their switching characteristics. These fluctuations provide an opportunity for the characterization mechanical properties. In particular, this applies to highly sensitive photonic metamaterials formed as periodic arrays of optical resonators supported by flexible nanomembrane structures that show giant electro-optical[17], magneto-electro-optical[18], phase change[28] and nonlinear optical[19], [29], [30]

responses. In this chapter we uexperimentally investigate thermal fluctuations in dielectric and plasmonic nanomechanical photonic metamaterials in the megahertz frequency range and demonstrate how measuring the spectra of thermal fluctuations of optical properties can be used to determine the main frequencies and damping of the nanostructures' natural oscillations, at which they can be efficiently controlled by external stimuli. We will examine thermal fluctuations in widely used optical metamaterials, arrays of metamolecules supported on beams (strings) cut from membranes of nanoscale thickness, as illustrated by Fig. 3.1. It should be noted that this study of thermal fluctuations was conducted in collaboration with Mr. Dimitrios Papas: in separate, parallel studies of different and independently designed and fabricated metamaterials, each using dedicated, independently-developed apparatus, we both observed these fluctuations (in my work - in transmission through an all-dielectric metamaterial; in Dimitrios' in reflection from a plasmonic metamaterial) and optically-induced tuning of nanowire mechanical Eigenfrequencies (Chapter 4).

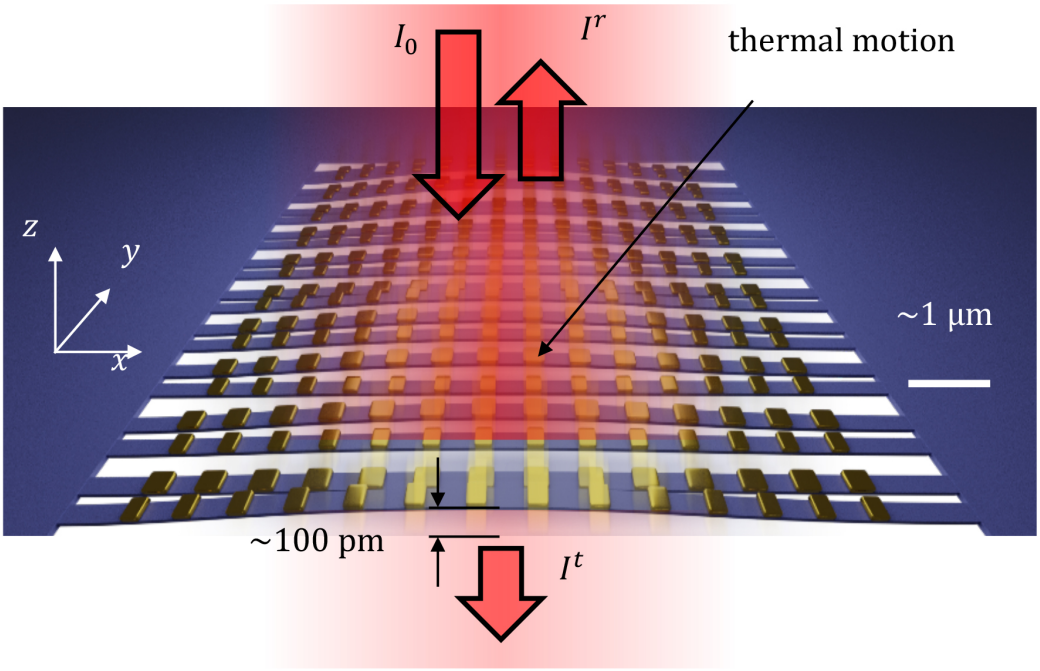

FIGURE 3.1: Thermal fluctuation of optical properties of nanomechanical metamaterials. The metamaterial is an array of beams of nanoscale width and thickness located in the xyplane. The beams, typically a few tens of microns long, support a periodic array of optical resonators of sub-wavelength (nanoscale) dimensions. Optical properties of such arrays can be controlled by actuation driven by external stimuli such as electromagnetic forces, optical and acoustic waves. Picometric thermal displacements of the individual beams also modulate the optical properties of the metamaterials and cause small fluctuations of the transmittance and reflectance of the metamaterial.

3.2 Theory background

Classical Brownian(thermal) motion experiments reveal how a microscopic particle is driven in chaotic motion externally by collisions with molecules of ambient gas or liquid. The majority of nanomechanical photonic metamaterials are constructed from cantilevers- or doubly-clamed beam-like components of microscopic length and nano-scopic cross-section. Here, the thermal motion of a cantilever or beam in vacuum is driven internally, by momentum transfer resulting from the annihilation and creation of phonons in the mode. (The emission and absorption of thermal photons is not important due to the low momentum of such photons.)

Nano-components such as beams and cantilevers can be modelled as damped mechanical oscillators[26], [27], [83].Considering nanomechanical structures located in the xy-plane, and engaged in thermal motion in the z direction, the Langevin equation for the thermal motion of such a component can be written as[54]:

$$\ddot{z} + 2\pi\gamma\dot{z} + \omega_0^2 z = \frac{F_{th}(t)}{m_{eff}} = \sqrt{\frac{4\pi k_B T\gamma}{m_{eff}}}\eta(t) \tag{3.1}$$

where $F_{th}(t)$ is the time dependent thermal force experienced by the oscillator related to the dissipation factor γ through fluctuation-dissipation theorem, $\eta(t)$ is a normalized white noise term, m_{eff} is the effective mass of the object, k_B is the Boltzmann constant, T is the temperature, $\omega_0 = 2\pi f_0 = \sqrt{k/m_{eff}}$ is the natural angular frequency of oscillation, f_0 is the natural frequency and k is the spring constant. The resonance quality factor $Q = \frac{f_0}{\gamma}$ in the limit of small damping, $\gamma \ll f_0$, which we assume here.

The origins of mechanical dissipation have been intensively studied over the last decades[54], [84], [85]. The most relevant loss mechanisms include clamping losses due to propagation of elastic waves into the substrate through the supports of the oscillator, fundamental anharmonic effects such as thermoelastic damping and phonon-phonon interactions, materials-induced losses caused by the relaxation of intrinsic or extrinsic defect states in the bulk or surface of the resonator, and, where applicable, viscous damping caused by interactions with surrounding gas atoms or by compression of thin fluidic layers.

Thermomechanical fluctuations of a component's position $z(t)$ are transduced to fluctuations of intensity of light scattered on the component, $\delta I(t) = \frac{\partial\mu(z,F)}{\partial z} \cdot I_0 \cdot \delta z(t)$, where I_0 and $I = \mu(z, F)I_0$ are the intensities of the incident and scattered light, and $\mu(z, F)$ is, generally, a nonlinear function of the component's displacement z and optical frequency F. As in a stochastic process the power spectral density is equal to the Fourier transform of its autocorrelation function[65], the scattered light amplitude spectral density(ASD) $s(f)$ resulting from small thermomechanical

fluctuations in position $\delta z(t)$ is:

$$\begin{aligned} s\left(f\right) &= \frac{\delta I}{\sqrt{\delta f}} \\ &= \left(\left. \frac{\partial \mu(z,F)}{\partial z} \right|_{z=0} \cdot I_0 \right) \times \sqrt{\frac{k_B T f_0}{2\pi^3 m_{eff} Q \left[\left(f_0^2 - f^2\right)^2 + \left(\frac{f f_0}{Q}\right)^2 \right]}} \end{aligned} \tag{3.2}$$

In a metamaterial, a non-diffracting array of identical oscillating components, the same formula will describe the spectra of fluctuations of the intensity of light reflected I^r and transmitted I^t through the metamaterial, see Figure 1. Fluctuations $s^{r,t}$ of the metamaterial's reflectance/transmittance correspond to the ratio between the amplitudes of fluctuating and non-fluctuating components of the transmitted/reflected light, that is Equation 3.2 divided by the incident intensity I_0 and optical reflectance/transmittance of the metamaterial without displacement, $\mu_0^{r,t}\left(F\right) = \mu^{r,t}\left(0,F\right)$.

$$\begin{aligned} s^{r,t}\left(f\right) &= \frac{\delta I^{r,t}/I^{r,t}}{\sqrt{\delta f}} \\ &= \frac{1}{\mu_0^{r,t}(F)} \times \left. \frac{\partial \mu^{r,t}(z,F)}{\partial z} \right|_{z=0} \times \sqrt{\frac{k_B T f_0}{2\pi^3 m_{eff} Q \left[\left(f_0^2 - f^2\right)^2 + \left(\frac{f f_0}{Q}\right)^2 \right]}} \end{aligned} \tag{3.3}$$

At the mechanical resonance, $f = f_0$, this modulation depth spectral density reaches a peak value of

$$s^{r,t}\left(f_0\right) = \frac{1}{\mu_0^{r,t}(F)} \times \left. \frac{\partial \mu^{r,t}(z,F)}{\partial z} \right|_{z=0} \times \sqrt{\frac{k_B T\ Q}{2\pi^3 m_{eff} f_0^3}} \tag{3.4}$$

Reflectance/transmittance fluctuations over a range of mechanical frequencies can be calculated by integration over the power spectral density of the fluctuations.

$$\begin{aligned} \delta I^{r,t}/I^{r,t} &= \sqrt{\int \left(s^{r,t}\left(f\right)\right)^2 df} \\ &= \frac{1}{\mu_0^{r,t}(F)} \times \left. \frac{\partial \mu^{r,t}(z,F)}{\partial z} \right|_{z=0} \times \sqrt{\frac{k_B T}{2\pi^3 m_{eff}}} \sqrt{\int \frac{\frac{f_0}{Q}}{\left(f_0^2 - f^2\right)^2 + \left(\frac{f f_0}{Q}\right)^2} df} \end{aligned} \tag{3.5}$$

Integration from 0 to ∞, or at least over the whole resonance, gives the root-mean-square (RMS) fluctuations.

$$\delta I_{RMS}^{r,t}/I^{r,t} = \frac{1}{\mu_0^{r,t}(F)} \times \left. \frac{\partial \mu^{r,t}(z,F)}{\partial z} \right|_{z=0} \times \sqrt{\frac{k_B T}{4\pi^2 m_{eff} f_0^2}} \tag{3.6}$$

where the final term corresponds to the RMS beam displacement of

$$\delta z_{RMS} = \sqrt{\frac{k_B T}{4\pi^2 m_{eff} f_0^2}} \tag{3.7}$$

From here is apparent that fluctuations of transmission and reflection will be largest at high temperatures, in metamaterials constructed from very light (low m_{eff}) building blocks, and at optical frequencies where transmission and reflection depend strongly on displacements of building blocks. Largest fluctuations over a narrow spectral range δf will be seen at high quality mechanical resonances [eq. 3.4]. As such, we should expect thermal fluctuations of optical properties to be strongest in highly optically dispersive nanomechanical metamaterials.

Assuming metamaterial beams, such as those shown by Figure 1, with an effective mass m_{eff} =1 pg and mechanical quality factor of Q = 1000 moving at a damped frequency f_0 =2 MHz, and a typical change in optical properties with beam displacement of $\partial\mu/(\mu_0\partial z)$ 1%/nm, one may expect to observe an RMS displacement amplitude of δz_{RMS} =160 pm at the centre of the beams at room temperature, resulting in a 0.16% RMS fluctuation of optical properties. At the mechanical resonance, the corresponding spectral densities of displacement and optical property modulation reach peak values of 3 $pm/\sqrt{Hz}$ and $3 \times 10^{-5}/\sqrt{Hz}$, respectively.

Thus, in nanomechanical metamaterials, thermal fluctuations are transduced to fluctuations of optical properties that determine the functional noise floor and dynamic range of nanomechanical photonic metadevices. At the same time, observation of the spectra of thermal oscillations gives direct access to the resonant frequencies of natural mechanical modes at which the metamaterial will be most responsive to external stimuli. This information on fluctuation and responsivity of the mechanical sub-system can help in the design of highly efficient metadevices[86]. Moreover, nanomechanical metamaterials typically comprise of large arrays of nominally identical elements (e.g. metamolecules, beams, etc.) with physical characteristics affected by fabrication tolerances, which endow them with slightly different natural frequencies, leading to inhomogeneous broadening and in some cases splitting of resonant lines, resulting in the degradation of the optical functionality. Similarly, line splitting can also be caused by coupling between individual responses of different metamolecules and their interactions with the supporting framework. Measurements of the spectra of thermal oscillations can provide insight into the nature of such line broadening and splitting. Previously, optomechanical transduction of natural oscillations has been observed in cantilevers[20], [31], antennas[21]], microresonators[23], other optomechanical systems[32] and exploited in atomic force microscopy[33]. Here we focus on the role of thermal oscillation in forming the optical properties of nanomechanical metamaterials.

3.3 Brownian motion and the optical properties of metamaterials: Experimental observation

Below we examine thermal fluctuations in the optical properties of two common types of metamaterial; plasmonic and all-dielectric nanomechanical metamaterials fabricated on membranes of nanoscale thickness. In both cases, the plasmonic and dielectric metamaterials are supported by arrays of flexible microscale beams cut from a silicon-nitride membrane by FIB milling.

The all-dielectric metamaterial shown in Fig. 3.2(c) was fabricated on a 200 nm thick Si_3N_4 membrane coated with a 115 nm layer of amorphous Si by PECVD, corresponding design criteria was supported by numerical calculations shown in section 5.3.2. This bilayer was then structured by FIB milling to define an array of asymmetric nanobrick pairs in the amorphous silicon layer, on 20.3 μm long Si_3N_4 beams. The structure supports a Fano resonance[87] at a wavelength of 1530 nm, underpinned by the excitation of antiparallel displacement currents in the pair of amorphous silicon nanobricks[88], see Fig. 3.2.

The dielectric and plasmonic metamaterial structures presented in Fig. 3.2 and studied in this work are generic nanomechanical metamaterial designs, which can be reconfigured: a) thermally, by changing the external temperature due to differential thermal expansion of neighbouring beams[16], b) optically, when displacement of

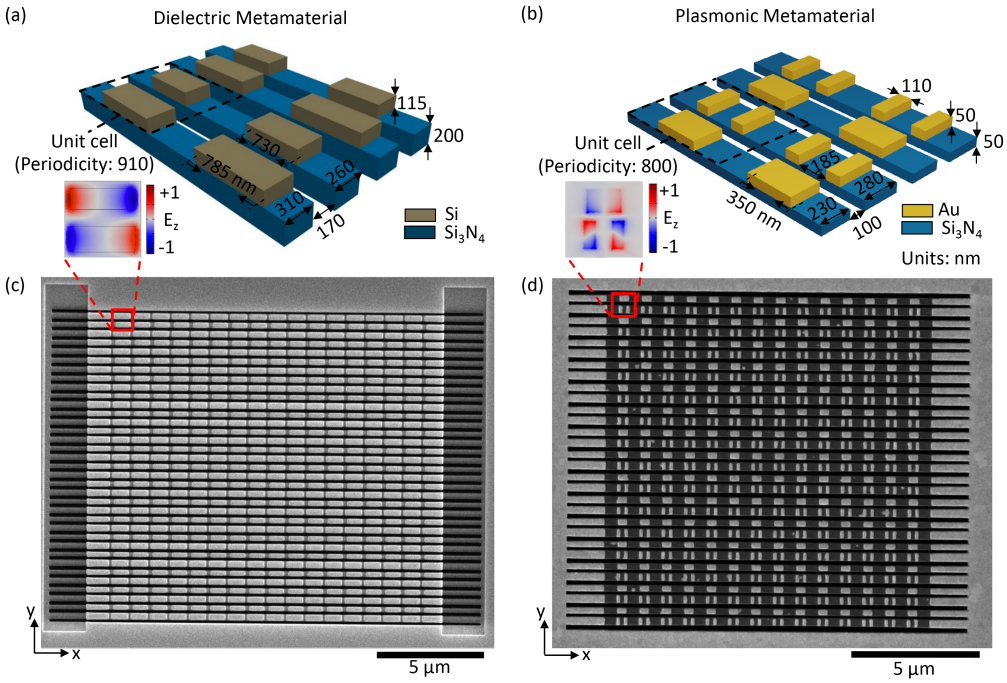

FIGURE 3.2: Nanomechanical metamaterials. Structural schematic and SEM images of dielectric (a, c) and plasmonic (b, d) metamaterials fabricated on silicon nitride membranes. Insets show the resonant field distributions excited by x-polarized incident light at wavelengths of 1550 nm (a) and 1310 nm (b).

neighbouring beams is driven by optical heating and optical forces[19], [30], c) acoustically, by ultrasound vibrations, d) electrostatically, by the Coulomb force between charged neighbouring beams[17] or selected beams and another electrode[89], and e) magnetically, by the Lorentz force acting in a static magnetic field on a current passing through the beams[18]. (In the latter two cases an electrically conductive layer is added to the structure.)

In both types of metamaterial, differential movements between neighbouring

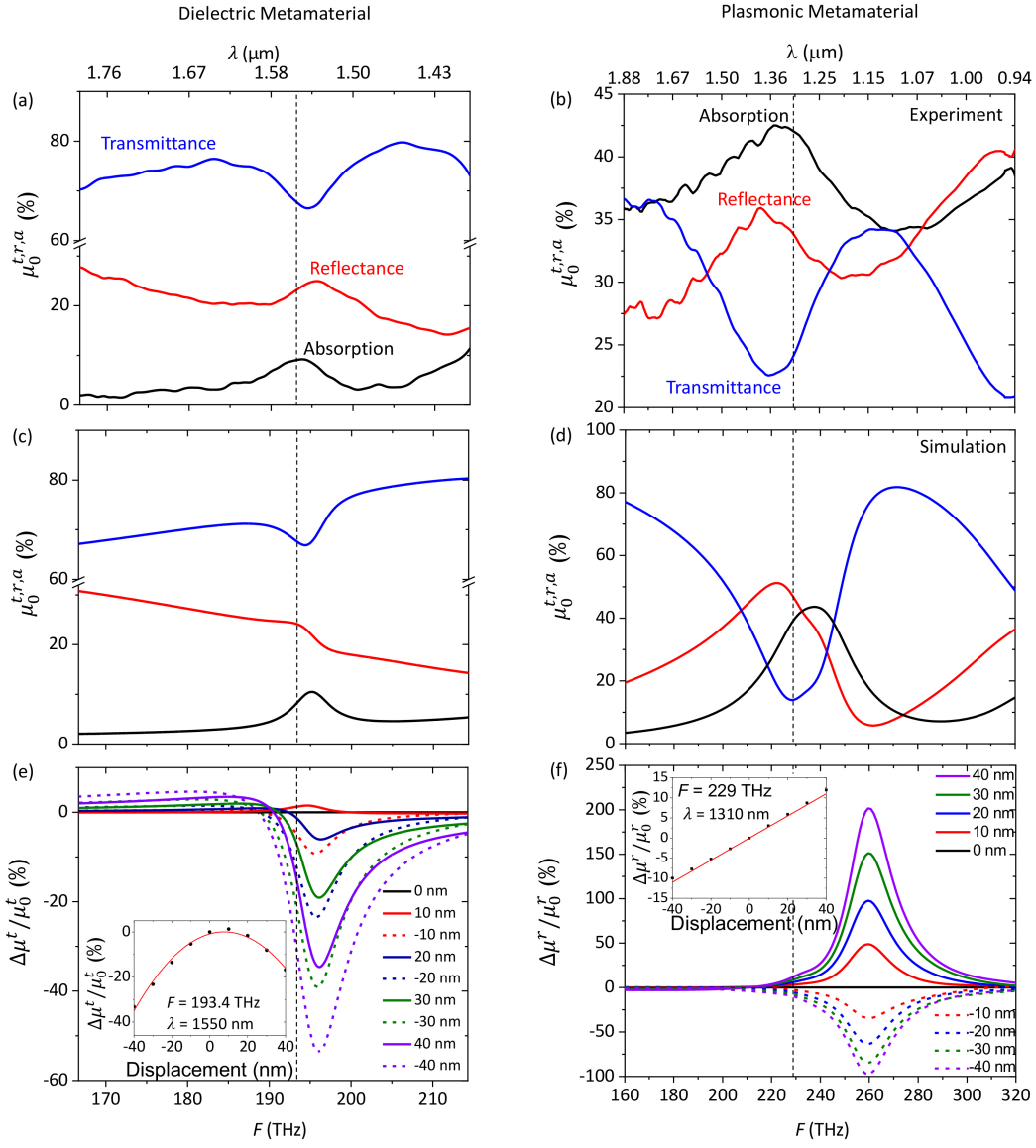

FIGURE 3.3: Optical properties of the dielectric and plasmonic nanomechanical metamaterials. Experimentally measured (a, b) and computed (c, d) optical reflection (μ_0^r), transmission (μ_0^t) and absorption (μ_0^a) spectra of the dielectric and plasmonic metamaterials. Computed values (e, f) of ($\Delta\mu^{t,r}/\mu_0^{t,r}$), a figure of merit of responsivity of the metamaterial's optical properties to relative displacement of neighbouring beams along z at different levels of displacement. The insets show the dependence of ($\Delta\mu^{t,r}/\mu_0^{t,r}$) on displacement at wavelengths of 1550 nm and 1310 nm respectively. Positive displacement corresponds to movement of narrower beams along $+z$ relative to wider beams; all results are for x-polarized light.

beams change the unit cell geometry and thereby the optical properties of the array. In such structures, the frequencies of the fundamental mechanical oscillatory modes f_0 of the beams lie in the megahertz range. At the same time the optical properties of the metamaterials are most sensitive to the beam movements when the optical frequency F is near either a plasmonic or dielectric resonance, where the value of $\frac{\partial \mu^{r,t}(z,F)}{\partial z}\Big|_{z=0}$ (see eq. 3.3 - 3.6)can be much higher than off-resonance. Here, the variation of optical properties can be a nonlinear function of beam displacement. This is illustrated by 3D finite element Maxwell solver simulations of the resonant optical properties of the arrays for different levels of mutual displacement between neighbouring beams, Fig. 3.3(e)-(f). For instance, the reflectivity of the plasmonic metamaterial changes linearly with displacement at 1310 nm (Fig. 3.3 (f)), while transmission of the dielectric metamaterial changes approximately parabolically with displacement at 1550 nm (Fig. 3.3(e)).

The thermal fluctuation of the optical properties of the dielectric and plasmonic nanomechanical metamaterials were studied at wavelengths of 1550 nm (transmission mode, 19.6 μW incident power) and 1310 nm (reflection mode, 48.2 μW power and) respectively with x-polarized CW laser light and ≈ 5 μm spot size. The metamaterial samples were mounted in a vacuum chamber at a pressure of $4 - 5 \mu bar$ to reduce air damping of the mechanical modes. The intensity of light transmitted and reflected from the samples was monitored with a photodetector and a radio frequency spectrum analyser.

As expected from Equation 3.3, in the spectra of transmitted and reflected light we observe a range of sharp peaks linked to the frequencies of thermal movements of the Si_3N_4 beams at their natural frequencies in the megahertz range, Fig. 3.4(a)(b). Here, the peaks are observed against a flat background of the photodetector noise. The average quality factor of the observed mechanical resonances for the dielectric metamaterial is 1.6×10^3, slightly higher than the quality factor of 1.6×10^3 for the plasmonic metamaterial.

In both cases we see an isolated group of several peaks related to the different beams within the structures. Here, variations between the resonance frequencies of individual, nominally identical beams are most likely caused by disparities in beam tension across the sample resulting from the non-uniformity of intrinsic stress in the membrane, rather than variations of their physical dimensions. These variation in tensile stress across the metamaterials, leading to the spread of individual peak frequencies, can be evaluated from Euler-Bernoulli beam theory[65], [90], which gives the stress-dependent fundamental frequency of a doubly clamped beam of rectangular cross-section as:

$$f_0 = 1.03 \frac{t}{L^2} \sqrt{\frac{E}{\rho} \left(1 + \frac{\sigma L^2}{3.4 E t^2}\right)} \tag{3.8}$$

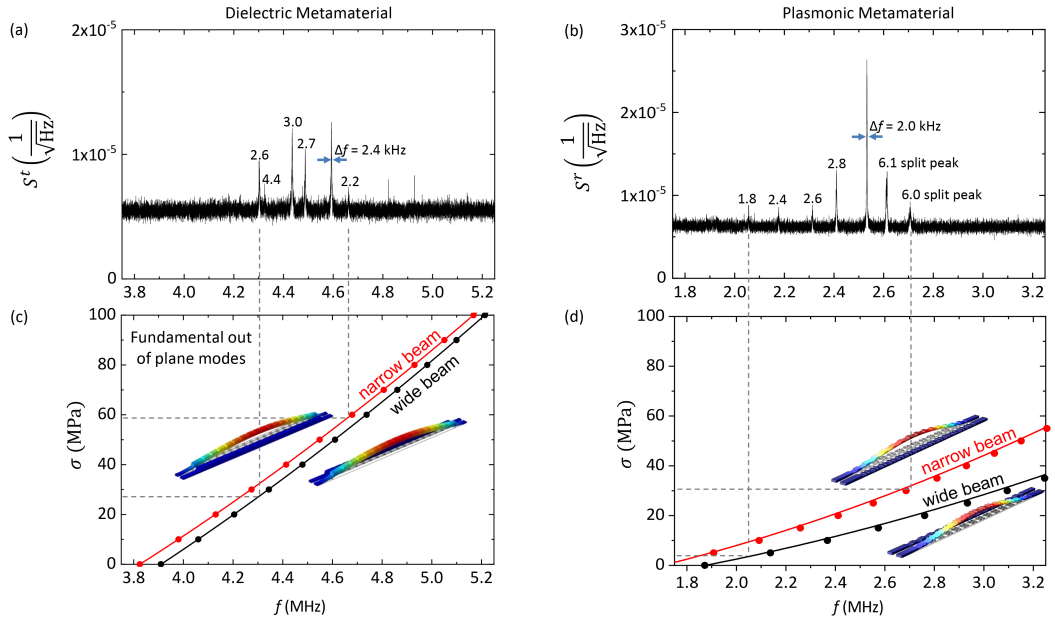

FIGURE 3.4: Thermal fluctuation of the optical properties of nanomechanical metamaterials. Measured spectral density of transmission modulation s^t (a) and reflectance modulation s^r (b) by dielectric and plasmonic metamaterials, respectively. Resonant peak widths δf are labelled in kHz. Frequencies of the fundamental out-of-plane resonances of the dielectric (c) and plasmonic (d) metamaterial beams for different levels of tensile stress σ. Simulated resonance frequencies of the nanostructured beams (data points) are shown with a fit according to eq. 3.8 (lines).

where t is the beam thickness, E is the Young's modulus, ρ is the density of the material and σ is the tensile stress along the beam length.

Fig. 3.4(c),(d), illustrating the relationship between stress and fundamental frequency, shows that for both the plasmonic and dielectric metamaterials, the observed variation of the fundamental mechanical resonance frequencies of beams are explainable by tensile stress variations from beam to beam of $\approx 30\ MPa$. This is not a surprizing number as stresses of between several hundred megapascals and a gigapascal are common in unstructured silicon nitride membranes, resulting in significant post FIB-fabrication stress variations across metamaterial arrays.

Inhomogeneous illumination of several beams within the optical spot profile can also contribute to inhomogeneous shifts of beam frequencies through thermal expansion of the beam length, which reduces stress: $\sigma = \sigma_0 - \alpha E \Delta T$, where σ_0 is the initial tensile stress, α the thermal expansion coefficient of the material and ΔT the temperature change. Considering conductive cooling, in our experiments, the laser-induced temperature increases reach $\approx 10\ K$ in the plasmonic metamaterial and $\approx 1\ K$ in the dielectric metamaterial. For a silicon nitride beam with an initial stress of 30 MPa such a temperature increase translates to around 20% stress reduction in the plasmonic metamaterial (2% for the dielectric metamaterial). In the present cases this translates to a 6%(2%) decrease in resonance frequency, see Fig. 3.3 (c),(d). We observe a significantly larger spread of resonance frequencies, with the lowest resonance frequency being 24%(7%) smaller than the largest, suggesting

that the observed spread of resonance frequencies is mainly due to intrinsic stress variations of the beams.

The fluctuation of the optical properties of the metamaterial are presented in terms of $S^{r,t}$, the relative spectral density of transmission/reflectance modulation, see Fig. 3.4(a), (b). To evaluate the root-mean-square of relative fluctuation of optical properties $\delta I^{r,t}_{RMS}/I^{r,t}$ resulting from thermomechanical fluctuations we need to integrate, as shown by eq. 3.5, over the entire frequency range. If only fundamental mechanical modes of the metamaterial beams are taken into account, this integral can be approximated as $S_0\sqrt{N\Delta f}$, where N is number of peaks/modes and S_0 and Δf are average amplitude and width of the peaks.

From the data presented in Fig. 3.4(a), (b), we can evaluate that the level of transmission fluctuation as $\frac{\delta I^t_{RMS}}{I^t} = 0.05\%$ for the dielectric metamaterial at 1550 nm, and the level of reflection fluctuation as $\frac{\delta I^r_{RMS}}{I^r} = 0.1\%$ for the plasmonic metamaterial at 1310 nm. These values can increase to about $\frac{\delta I^t_{RMS}}{I^t} = 0.1\%$ and $\frac{\delta I^r_{RMS}}{I^r} = 1.5\%$ at the dielectric and plasmonic resonances, see Fig. 3.3(e)(f).

Finally, we shall note that thermal fluctuations can give rise to nonlinear effects. The nonlinearity of coupling between metamaterial optical properties $\mu^{r,t}(z, F)$ and beam displacements z will result in fluctuations of the optical properties at harmonics of the fundamental mechanical oscillation frequency f_0. Moreover, the mechanical motion itself may be thermally excited into the nonlinear regime. In the case of beams anchored at both ends, the oscillation becomes nonlinear when the amplitude of oscillation becomes comparable to the beam thickness t divided by the square root of the beam's mechanical quality factor[56]Q: a beam with length L, width w and thickness t enters the nonlinear regime of thermal motion for

$$L > 2.6 \left(\frac{Ewt^5}{Qk_BT} \right)^{1/3} \tag{3.9}$$

As an example, at room temperature, a silicon nitride beam of rectangular 100 $\times$ 100 nm cross-section and quality factor Q = 1000 will enter the nonlinear regime of Brownian motion at $L > 100\mu m$. Such effects though lie beyond the scope of the present study.

3.4 Conclusions

In conclusion, we have observed that the optical properties of dielectric and plasmonic membrane nanomechanical metamaterials at near-infrared (telecoms) wavelengths exhibit thermal fluctuations of order 0.1%, rising potentially to $\approx$ 1% at optical resonances. The spectra of fluctuations enable metamaterial characterization at the level of individual mechanical elements. They provide exact information on the frequencies at which a nanomechanical metamaterial can be efficiently actuated by external stimuli, providing insight to mechanisms of broadening and splitting

of mechanical resonances in metamaterials, and aiding in the optimization of their performance.

Chapter 4

Optical control of nanomechanical eigenfrequencies and Brownian motion in metamaterials

Nanomechanical photonic metamaterials provide a wealth of active switching, nonlinear and enhanced light-matter interaction functionalities by coupling optically and mechanically resonant subsystems. Thermal (Brownian) motion of the nanostructural components of such metamaterials leads to fluctuations in optical properties, which may manifest simply as noise, but which also present opportunity to characterize performance and thereby optimize design at the level of individual nanomechanical elements. In this chapter, I show that Brownian motion in an all-dielectric metamaterial ensemble of Si/Si_3N_4 beams can be controlled by light at sub- $\mu W/\mu m^2$ intensities. Induced changes in beam temperature of just a few Kelvin, dependent upon beam's dimensions, material composition, and the direction of light propagation, yield proportional changes of several percent in the few-MHz Eigenfrequencies and picometric displacement amplitudes of Brownian motion. The tuning mechanism can provide active control of frequency response in photonic metadevices and may serve as a basis for bolometric, mass and micro/nanostructural stress sensing.

4.1 Introduction

By virtue of their low mass and fast (MHz-GHz frequency) response times[14], nanomechanical oscillators actuated [15], [19], [29] and/or interrogated [89], [91] by light are of fundamental and applied interest in numerous applications[92], ranging from mass [58]–[60] and force sensors[62], [63] to photonic data processing[93], [94] and quantum ground state measurements[95]. As the dimensions of such systems decrease their thermal(i.e. Brownian) motion assumes increasing importance. By adding noise to induced/controlled movements that underpin the functionality it can constrain performance, but it also presents opportunity by directly linking observable(far-field optical) properties to geometry, composition and temperature at the nanoscale.

Here, I show that such motion can be optically controlled at $\mu W/\mu m^2$ intensities in nanomechanical photonic metamaterials. In an array of mechanically independent and (by design) alternately dissimilar dielectric beams, which are at the same time of identical bilayer (i.e. asymmetric) material composition and part of an optically

resonant ensemble subject to the fundamental constraint of linear transmission reciprocity, dependences of motion eigenfrequencies and picometric displacement amplitudes on local light-induced temperature changes can be accurately determined.

4.2 Results and discussions

In the current study, I employ an all-dielectric metamaterial comprising pairs of dissimilar (by length L_{Si} and width W) Si nanobricks on a free-standing array of flexible Si_3N_4 beams (Fig. 4.1(a)), corresponding design criteria was supported by numerical calculations shown in section 5.3.2. It is fabricated on a 200 nm thick Si_3N_4 membrane (Norcada, Inc.) coated by PECVD with a 115 nm thick layer of amorphous Si. This bilayer is then structured by FIB milling to define rows of alternately short, narrow (720 nm × 210 nm) and long, wide (780 nm × 300 nm) nano-bricks in the Si layer on parallel 21.05 μm long beams cut through the Si_3N_4 layer, with a gap size between neighbouring beams of 170 nm. Here, I categorise the

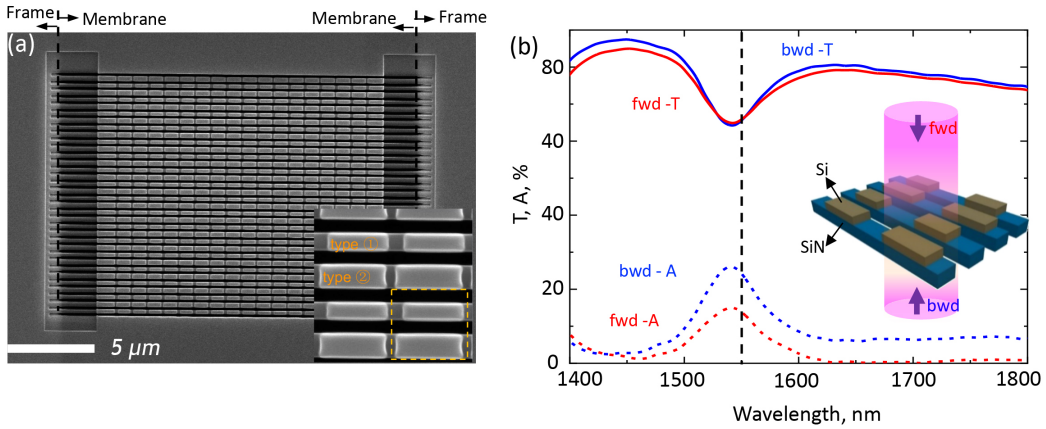

(c)

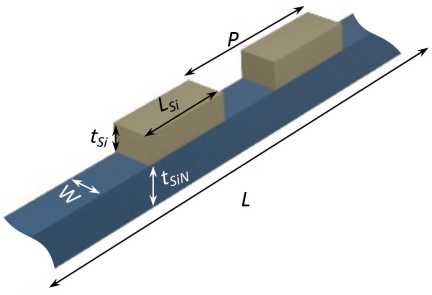

(d)

Dimension	Beam type ①	Beam type ②
Nanowire length *L*, µm	21.05	
Width *W*, nm	210	300
Si_3N_4 thickness t_{SiN}, nm	200	
Si thickness t_{Si}, nm	115	
Si brick length L_{Si}, nm	720	780
Si brick period *P*, nm	910	

FIGURE 4.1: Dielectric nanomechanical metamaterial sample and its linear optical properties. (a) SEM image of the metamaterial, fabricated on a 21.05 μm wide free-standing Si_3N_4 membrane. The inset enlarged section shows detail of the supported Si nano-bricks – the dashed line denotes a metamolecule of the metamaterials. (b)Measured transmission [T] and absorption[A] spectrum of the fabricated structure, and the dashed rectangular area indicates wavelength of laser that will be employed to investigate the thermal properties of the metamaterials, the inset shows the designation of forward (fwd) and backward (bwd) illumination directions. (c) Dimensional schematic of a section of a nanomechanical metamaterial beam element. (d) Dimensional details of the beam elements.

beams into two group: beams type ① with short and narrow bricks on Si_3N_4 beams and beams type ② with short and wide bricks on beams for the convenience of later investigation. These two group of beams have also been labelled on the zoom-in SEM image of sample in the inset of Fig. 4.1(a); relevant dimensional details of these two types of beam can be found in Fig. 4.1(c) and (d). The metamolecule of photonic metamaterials I studied here is indicated by a yellow dashed rectangular in the inset of Fig. 4.1(a) with periodicity of 910 nm and 850 nm along and perpendicular to the nano wire directions.

This metamaterial structure supports a near-infrared closed mode optical resonance (e.g. Fano resonance)[87]at a wavelength of 1542 nm underpinned by the excitation of antiparallel displacement currents in adjacent dissimilar silicon nanobricks by incident light polarized parallel to the long axis of the bricks. The measured transmission and absorption spectra for forward and backward illumination of this structure is shown in Fig. 4.1(b), where the forward (fwd) direction of light propagation is designated as that for which light is incident on the Si side of the sample; backward (bwd) the Si_3N_4 side (see the inset in Fig. 4.1(b)). Ideally, the transmission spectra for backward and forward illumination should be identical as it is a linear reciprocal system. However, there are small differentials in the measured transmission spectra in Fig. 4.1(b). These differentials is because I conduct this forward and backward measurement by flipping over the sample. And this process inevitably introduce systematic errors, such as position and polarization misalignment. Different absorption spectra in Fig. 4.1(b) (dashed lines) show different absorption cross sections of the sample when send light from different sides of the sample, which provide another new channel to control thermal motions in nanomechanical metamaterials. In the vicinity of this optical resonance, thermal (Brownian) motion of the beams – mutual positional fluctuations of pico- to nanometric amplitude – translate to fluctuations of metamaterial transmission (of order 0.1%) at their few-MHz natural mechanical resonance frequencies[96]. These thermomechanical oscillations are detected as peaks in frequency spectra of transmission amplitude spectral density (Fig. 4.2(b)).

In order to make the best use of this new channel to control thermal motions of the sample and introducing the system errors as less as possible, an apparatus based on a MEMS directional switch was built up (see Fig. 4.2(a)). In this setup: the metamaterial is mounted in a vacuum chamber at a pressure of 4×10^{-3} $mbar$ (to exclude air damping of mechanical motion). This is located between a confocal pair of $20\times(N.A. = 0.4)$ microscope objectives, via which incident light at a wavelength of 1550 nm is focused onto the sample (to a spot of diameter ≈ 5 μm) and transmitted light is collected finally by a photodetector and transferred electric signal is then processed in a spectral analyser. This arrangement includes a fiber-optic MEMS switch to enable transmission measurements in both directions through the sample without disturbance of its position/alignment relative to the beam path.

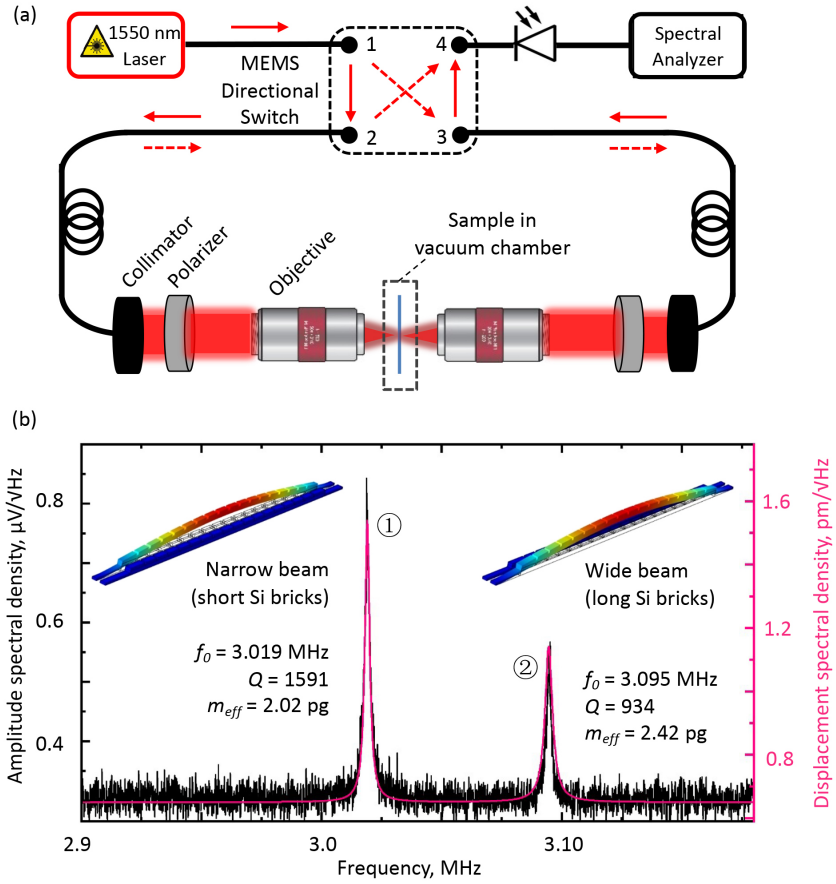

FIGURE 4.2: (a)Schematic of experimental apparatus for recording frequency spectra of metamaterial transmission. Other than between the two collimators, light is carried in polarization-maintaining single-mode optical fiber, with the MEMS switch providing for inversion of the light propagation direction through the sample. (b) Exemplar measurement of optical transmission amplitude spectral density [for light incident on the Si_3N_4 side of the sample at a power level of 15.93 μW], showing a pair of peaks associated with the mechanical resonances of two individual beams within the array: ①/② a narrower/wider wire decorated with shorter/longer Si bricks. The overlaid magenta curve and calibrated displacement spectral density scale [to the right-hand side] are obtained by fitting eq. 4.1 to the experimental data. Derived values of f_0, Q and m_{eff} are shown inset. Numerically simulated mode profile of the out-of-plane mechanical mode of these two types of beam also shown in the inset.

Fig. 4.2(b) shows a representative measurement of optical transmission amplitude spectral density (ASD), in which peaks associated with the fundamental out-of-plane flexural modes of a pair of individual beams – one narrow(type ①) and one wide (type ②) as indicated in the inset of Fig. 4.1(a), decorated respectively with short and long Si nano-bricks – are seen. Attribution to this oscillatory mode is confirmed through computational modelling, where beams mechanical properties are simulated using the structural mechanics module in COMSOL Multiphysics (finite element method). For the ideal rectilinear geometry of Fig. 4.1(c)(d), and densities and Young's moduli of silicon nitride and silicon as in Table 4.1 above, Eigenfrequencies of the fundamental out-of-plane flexural modes are estimated as 3.04 and 3.13 MHz respectively for the type ①(narrower) and type ② (wider) beams. These

TABLE 4.1: Mechanical and thermal properties of Si and Si_3N_4

Materials / Properties	Si	Si_3N_4
Density $\rho, Kg \cdot m^{-3}$	2330	3100
Young's modulus E, Gpa	150	260
Thermal expansion coefficient α, K^{-1}	1.0×10^{-6}	2.8×10^{-6}
Thermal conductivity $\kappa, W \cdot m^{-1} \cdot K^{-1}$	1.5	2

are sufficiently close to the measured frequencies (Fig. 4.2(b)) as to confirm that the Brownian motion peaks observed in experiment are associated with this mode of oscillation – discrepancies being accounted for by manufacturing imperfections and internal stress within the silicon nitride. (For comparison, Eigenfrequencies of the fundamental in-plane flexural modes of type ② (wider) beams are much higher, at around 4.54MHz.) Corresponding simulated mode profile for the fundamental out-of-plane mode of these two type of beams are shown in the inset of Fig. 4.2(b). The beam displacement ASD $s(f)$ can be expressed as[65]:

$$s(f) = \sqrt{S(f)} = \sqrt{\frac{k_B T f_0}{2\pi^3 m_{eff} Q \left[\left(f_0^2 - f^2\right)^2 + \left(f f_0/Q\right)^2 \right]}} \tag{4.1}$$

Where k_B is the Boltzmann constant, T is temperature, and for each mode, m_{eff}, f_0 and Q are respectively the effective mass, natural frequency and quality factor of the oscillator, $S(f)$ is power spectra density. Experimental data can thus be calibrated – the vertical scale in Fig. 4.2(b) converted from signal measured in μV to beam displacement in picometres, by fitting Eq. 4.1 to the data. Specifically, we fit a linear superposition of two instances of the expression, one for each of the spectral peaks with co-optimized values of m_{eff}, f_0 and Q. RMS thermal motion amplitudes can then be evaluated as the square root of an integral of power spectral density $S(f) = s(f)^2$ over frequency:

$$< z >= \sqrt{\int s(f)^2 df} \tag{4.2}$$

These calculations yield amplitudes of 75.5 and 67.1 pm respectively for the lower and higher frequency peaks in Fig. 4.2(b), which compare extremely well with analytical values of 76.0 and 67.6 pm derived from energy equipartition theorem[54].

$$< z >= \sqrt{\frac{K_B T}{4\pi^2 m_{eff} f_0^2}} \tag{4.3}$$

Fig. 4.3 shows how the Brownian motions characteristics of beams, as manifested in the ASD of optical transmission, depend upon (i.e. can be controlled by tuning) incident laser power, and how this dependence differs for the two directions

of incident light propagation. With increasing laser power, mechanical Eigenfrequencies red-shift (Fig. 4.4(a)) and RMS displacement amplitudes increase (Fig. 4.4(b)), both in direct proportion and more rapidly for the backward propagation direction. The behaviours are consistent with a photothermal tuning mechanism, whereby laser-induced heating decreases tensile stress in the beams. The effect is more pronounced for the backward direction of light propagation because, while forward and backward transmission levels are identical (as they must be in a linear, reciprocal medium), reflectivity and absorption are not (Fig. 4.1(b)).

An analytical model for optical control of thermomechanical (Brownian) motion resonances, tightly constrained by the requirement to describe the properties of two independent, similar (related) but not identical oscillators – narrow and wide Si/Si_3N_4 bilayer beams, under two similar (related) but not identical regimes of optical excitation – fwd and bwd directions of illumination, provides for accurate

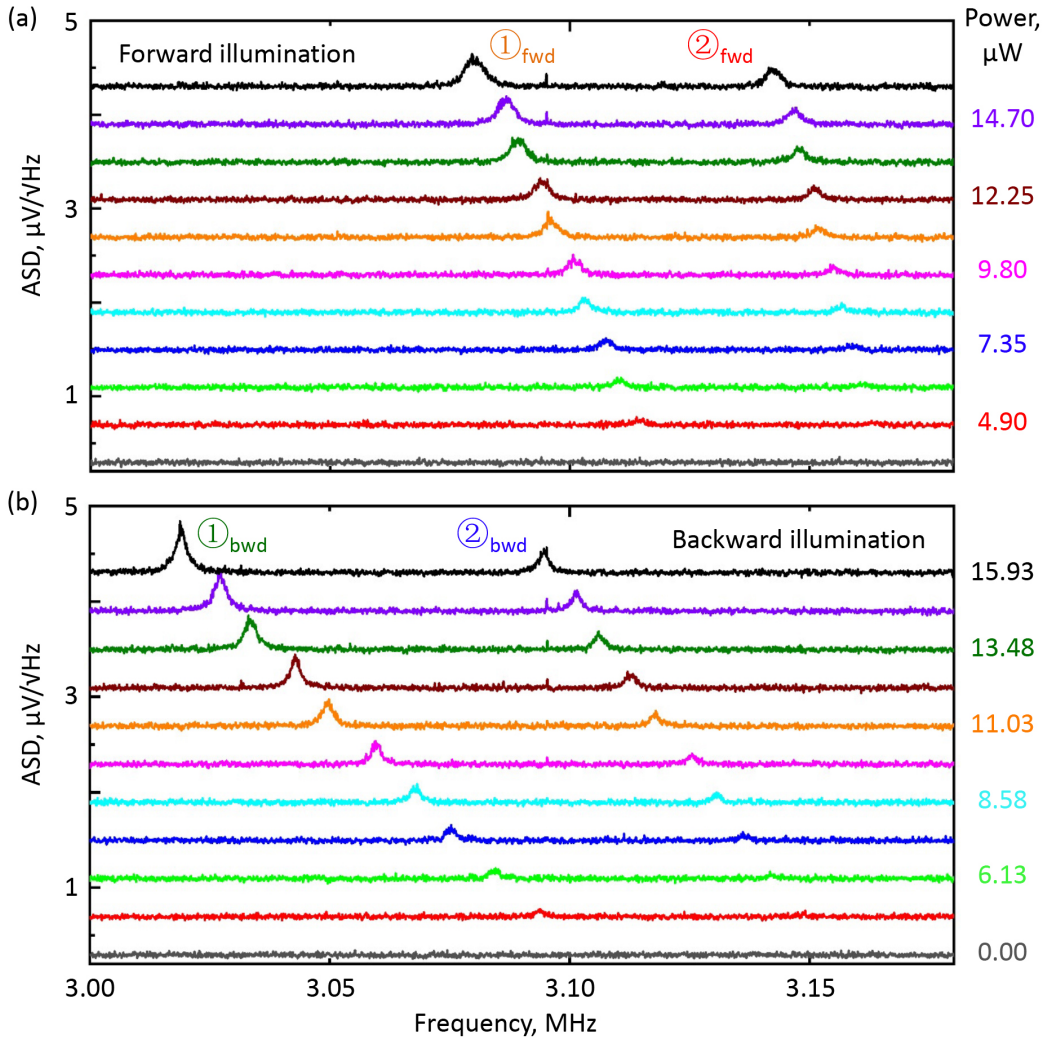

FIGURE 4.3: Optical tuning of Brownian motion. Transmission amplitude spectral density(ASD), showing peaks ① and ② as assigned in Fig. 4.2, for opposing directions of light propagation through the sample – (a) forward and (b) backward [light incident respectively on the silicon and the silicon nitride side], and for a range of laser power levels [as labelled].

quantitative evaluation of light-induced temperature changes in the individual beams and corresponding relationships between their resonance frequencies/amplitudes, illumination conditions and the optical properties of the metamaterial array. From Euler-Bernoulli beam theory[90], the stress-dependent fundamental frequency of a doubly clamped beam of homogenous rectangular cross-section is:

$$f_0 = 1.03\frac{t}{L^2}\sqrt{\frac{E}{\rho}\left(1+\frac{\sigma L^2}{3.4Et^2}\right)} \tag{4.4}$$

where t and L are the thickness and length of the beam, E is Youngs's modulus, ρ is density and σ is tensile stress along the beam length. The temperature-dependence of stress can be expressed in the form[19]:

$$\sigma = \sigma_0 - \alpha E \Delta T \tag{4.5}$$

where σ_0 is the stress at ambient temperature, ΔT is the difference between average beam and ambient temperatures, and α is the beam's thermal expansion coefficient.

For the purpose of applying these expressions to the present case of silicon nitride beams decorated with silicon nano-bricks, we evaluate effective values of E, ρ and α for homogenous rectangular-section beams based upon weighted averages of parameters for the two materials, e.g., Si and Si_3N_4, according to their volume fractions ($V_{Si}$and V_{SiN}) present in a given beam, and

$$X_e = \frac{X_{Si}V_{Si}+X_{SiN}V_{SiN}}{V_{Si}+V_{SiN}} \tag{4.6}$$

where X is density ρ, Young's modulus E, the thermal expansion coefficient α, or thermal conductivity κ showing below. Values of X_{SiN} and X_{Si} are given in Table 4.1, and values of beam effective medium parameters for the present case are given in Table 4.2.

The presence of a heat source is assumed to be uniformly distributed over the rectangular cross-section at the mid-point of the beam, while the two ends are held at ambient temperature ($T_0 = 298K$). At equilibrium, the difference ΔT between average beam and ambient temperatures is then[97]:

$$\Delta T = \frac{P_{abs}L}{8\kappa A} \tag{4.7}$$

Where κ is thermal conductivity, A is the cross-sectional area, and P_{abs} is the absorbed power of the heat source. In the present case, effective values of κ and A are again evaluated for the two types of beam based upon geometry and the material parameters of Si and Si_3N_4(see Supplementary Information), and P_abs is the optical power absorbed by the beam: $P_{abs} = \mu\gamma P_{in}$, where P_{in} is the total power incident on the metamaterial, γ is the absorption coefficient of the metamaterial, and μ is

TABLE 4.2: beams effective medium parameters

Properties \ types	beam type ①	beam type ②
Thickness t_e, nm	139	142
Density $\rho_e, Kg \cdot m^{-3}$	2870	2859
Young's modulus E_e, Gpa	232	230
Thermal expansion coefficient α_e, K^{-1}	2.263×10^{-6}	2.237×10^{-6}
Thermal conductivity $\kappa_e, W \cdot m^{-1} \cdot K^{-1}$	1.851	1.844
Cross section area A_e, nm^2	52760	76945

the 'absorption cross-section' of an individual beam.

By fitting the set of equations 4.4-4.7 simultaneously to all four sets of experimental datapoints in Fig. 4.4(a), for the dependences of Brownian motion Eigenfrequency on laser power, under constraints that:

1. μ must be identical for forward and backward directions of illumination for a given beam (i.e. the same beam will intercept the same fraction of incident light in both directions);

2. γ must be identical for the two beams for a given illumination directions (i.e. as a metamaterial ensemble property, absorption can only have a single value in each direction);

3. σ_0 must take a single fixed value (ensuring degeneracy of nominally forward- and backward-illumination zero-power resonant frequencies for each type of beam);

One could obtain the four solid curves plotted in each panel of Fig. 4.4. The Eigenfrequency fitting (Fig. 4.4(a)) is extremely good and yields zero-power (i.e. ambient temperature) resonant frequencies of 3.176, 3.128 MHz for the wider and narrower beams respectively, giving a value for intrinsic tensile stress of $\sigma_0 \approx 5.55$ MPa. Derived values of $\mu \approx 4.93\%$ and 5.63% respectively for the narrower and wider beams – are consistent, to a first approximation, with their areas of geometric intersection with the $\approx$5 μm diameter incident laser spot. However, they are not in proportion simply to the ratio of beam widths (0.7:1). This is because the near-field distribution of electromagnetic field around the metamaterial at resonance is not homogenous, and the absorption cross section of constituent beams is therefore not expected to be directly proportional to its geometric cross-section. Derived values of $\gamma = 10.55\%$ and 25.82% respectively for the forward and backward directions of light propagation – correspond very well to measured (far-field) values of metamaterial absorption at 1550 nm (Fig. 4.1(b)): 13.5% and 23.7%.

Light-induced changes in beam temperature (Fig. 4.4(c)) depend upon the direction of illumination and beam dimensions – which is to say, upon the strength of optical absorption and the rate at which heat is dissipated (the latter being lower for the beam of smaller cross-section). The narrow beam changes temperature at a rate

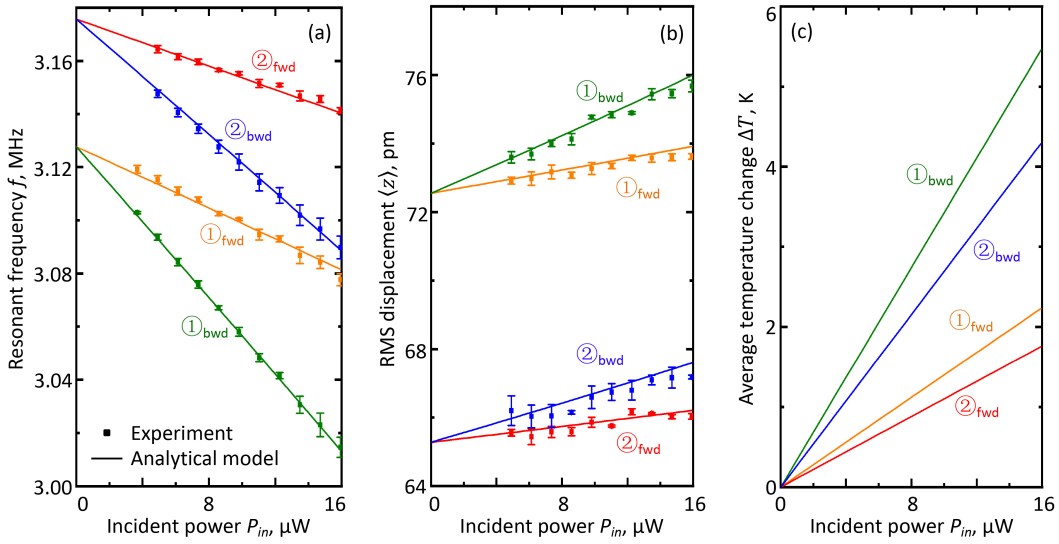

FIGURE 4.4: Photothermal control of beam mechanical resonances. Dependences for peaks ① and ② in Fig. 4.3 [i.e. for narrow and wide beams as identified in Fig. 1c, under nominally forward and backward directions of illumination] of (a) resonance frequency, (b) RMS displacement amplitude, and (c) light-induced beam temperature change on incident laser power [total power incident on the metamaterial sample]. Square symbols are experimental data points, with error bars given by the standard deviation over three repeated measurement cycles. Solid curves are derived from an analytical description of the photo-thermal tuning mechanism via a simultaneous best-fit to the four experimental datasets in (a).

of 26.93 $K/\mu W$ of absorbed power, the wide beam at 18.54 $K/\mu W$. These derived dependences of induced temperature change ΔT on laser power map to the theoretical dependences of RMS Brownian motion amplitude presented in Fig. 4.4(b) via Eq. 4.3, using values of m_{eff} for the two beams established in the above (Fig. 4.2(b)) calibration of displacement spectral density. The picometrically accurate correlation with experimental data points separately derived via integrals of PSD over frequency (via Eq. 4.2) is exceptionally good.

4.3 Conclusions

In summary, this chapter has shown that fluctuations in the resonant optical properties of a photonic metamaterial, which are associated with the mechanically resonant Brownian motion of its constituent elements, can be controlled by light at sub-$\mu W/\mu m^2$ intensities. In an all-dielectric metamaterial ensemble of free-standing Si_3N_4 beams (mechanical oscillators) supporting an array of silicon nano-bricks (optical resonators), the few - MHz natural frequencies of beams shift up to 3.6% and few tens of pm displacement amplitudes of thermal fluctuations vary up to 4.3% with light intensity of $0.8\mu W/\mu m^2$.

An analytical model for the photothermal tuning mechanism, simply but strictly constrained by the requirements of optical transmission reciprocity in a linear medium, links the local, nanoscopic properties and behaviors of individual beams (i.e. at sub-wavelength scale) to the far-field optical properties of the (micro/macroscopic)

metamaterial ensemble. It provides for accurate evaluation of light-induced changes in beam temperature and of ambient condition (zero-illumination) tensile stress and Brownian motion Eigenfrequencies and displacement amplitudes.

The ability to finely tune the nanomechanical resonance characteristics of photonic metamaterials may be beneficial in a variety of metadevice applications where, for example, the frequency of nanostructural oscillation is required to match (or avoid matching) another frequency, such as that of a pulsed laser. The fact that tuning characteristics can (as here) depend strongly upon the direction of light propagation through a metamaterial by simple virtue of bi-layer material composition (leading to different levels of reflection and absorption for light incident on opposing sides) may find application in devices to favor/select a single direction of propagation. The accurately quantifiable sensitivity of optical response to nanomechanical properties in such structures also suggests applications to bolometric sensing and detection of changes in mass (e.g. through adsorption/desorption) or micro/nanostructural stress.

Chapter 5

Asymmetric nonlinear transmission in nano-opto-mechanical metamaterials driven by optical forces

Asymmetric transmission of light through a slab of materials can be achieved in the presence of magnetic field and this is widely used in Faraday optical isolators[98]. It can also be seen with a combination of a nonlinear absorber and intensity attenuator[99], however, this solution found no practical applications due to high level of intensity required. Here we demonstrate in nano-opto-mechanical metamaterials resonant excitation of optical and mechanical sub-systems create profound light-induced transmission asymmetry reaching 16% at low intensities ($\mu W/\mu m^2$), making it suitable for a range of laser technology and fibre telecom applications.

5.1 Introduction

The reciprocity of optical transmission is a fundamental tenet of linear optics - unless a medium is statically magnetized or causes polarization or mode conversion - it must transmit light, of a given wavelength and polarization state, identically in the forward and backward directions. This symmetry can of course be broken in nonlinear media[35] (i.e. at high intensities, as in the very first experimental demonstration of optical nonlinearity[99]), and in devices exploiting Faraday rotation[34], [98] (which are unavoidably bulky due to the necessity of applying a magnetic field over a macroscopic path length). Transmission asymmetry is also possible in (usually chiral, often multilayer, characteristically lossy) metamaterials where propagation is accompanied by polarization or mode conversion[51], [52], [100]–[102]. On the other hand, optomechanics offers a new playground for building non-reciprocal devices, as temporal modulations can be induced by mechanical resonances[36]. The nano-opto-mechanical oscillators build ideal platforms to pursue such devices with remarkable performance and functionalities, due to their low mass and quick response time. The movement of oscillators can be optically transduced to a measurable signal benefitting from low-noise lasers and detections techniques, enabling the realization of asymmetric transmission devices. On the other hand, the optical resonant features of photonic metamaterials could enhance light-matter interaction, providing further improvement the performance of nanomechanical devices[19], [29], [30].

Here, I demonstrate that the optical forces generated within free-standing nano-opto-mechanical metamaterials can be comparable in magnitude to the elastic restoring forces resulting in nanoscale deformation, and they can be utilized to dynamically reconfigure metamolecules in a manner that depends upon the direction of light propagation. In consequence, the structure can manifest strongly nonlinear and directionally asymmetric transmission, determined by the combination of its optical (near-infrared) and mechanical resonances.

5.2 A toy model to demonstrate asymmetric transmission induced by nonlinearity

It would be a helpful exercise to build a toy model giving the mechanism behind asymmetric transmission induced by nonlinearity. Here, a simple toy model for investigating the influence of nonlinearity on asymmetric transmission is damped driven coupled oscillators system. Fig. 5.1(a) shows the schematics of such a system, consisting of two oscillators with different mass m_1 and m_2 as labelled in the figure. The coefficient of friction γ and also the spring constant K for this two oscillators are set as the same. With regard to the coupling term, we considered linear term with coupled coefficient τ and nonlinear term with coefficient α. One of the oscillators is driven by a periodical harmonic force $F(t) = F_0 e^{i\omega t}$ and the oscillation amplitude of

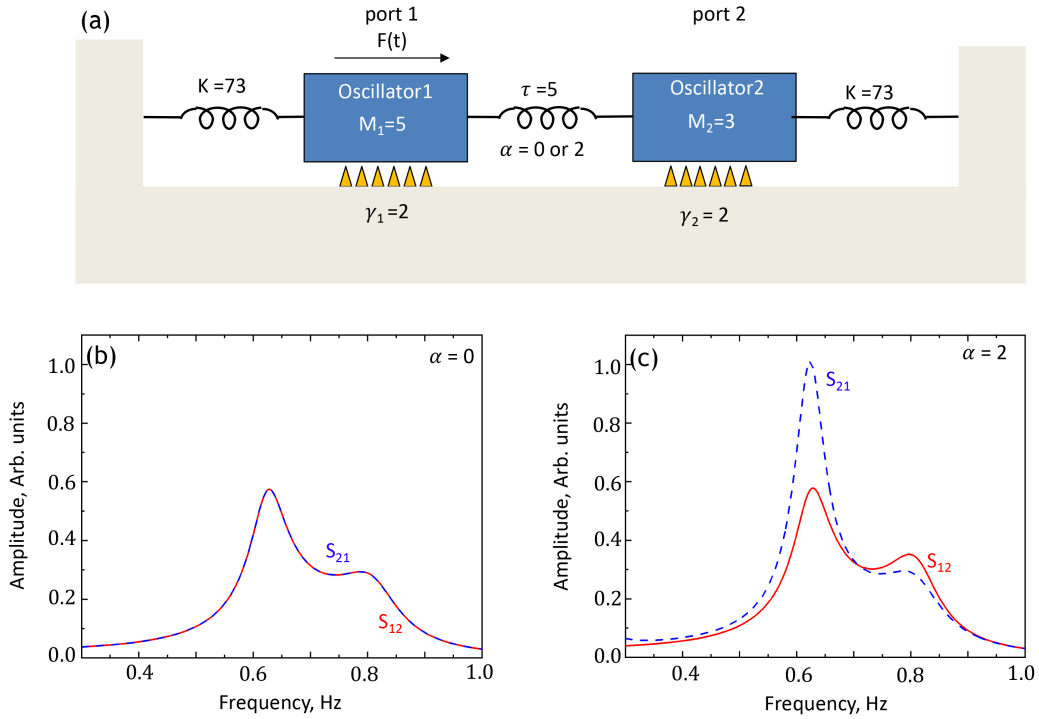

FIGURE 5.1: A toy model on coupled oscillators system to demonstrate the role of nonlinearity on asymmetric transmission. (a) Spring model representing a two coupled masses system excited by a harmonic force $F(t)$. (b) Linear coupled system, in which the transmitted signals are identical for different driven directions. (c) Nonlinear coupled system, the transmitted signals behave differently for different driven directions.

another oscillator is then monitored as transmitted signal. To provide a quantitative description of the system, we write the dynamic equations of the oscillator 1 and 2 in terms of the displacement x_1 and x_2 from their respective equilibrium positions, when oscillaor 1 is driven:

$$\begin{aligned} m_1\ddot{x}_1 + \gamma_1\dot{x}_1 + Kx_1 + \tau\left(x_1 - x_2\right) + \alpha\left(x_1 - x_2\right)^3 &= F_0 e^{i\omega t} \\ m_2\ddot{x}_2 + \gamma_2\dot{x}_2 + Kx_2 + \tau\left(x_2 - x_1\right) + \alpha\left(x_2 - x_1\right)^3 &= 0 \end{aligned} \tag{5.1}$$

when oscillator 2 is driven:

$$\begin{aligned} m_1\ddot{x}_1 + \gamma_1\dot{x}_1 + Kx_1 + \tau\left(x_1 - x_2\right) + \alpha\left(x_1 - x_2\right)^3 &= 0 \\ m_2\ddot{x}_2 + \gamma_2\dot{x}_2 + Kx_2 + \tau\left(x_2 - x_1\right) + \alpha\left(x_2 - x_1\right)^3 &= F_0 e^{i\omega t} \end{aligned} \tag{5.2}$$

These equation system can be numerically solved with the 4^{th} - order Runge-Kutta algorithm. Here, we define transmitted signal from oscillator 1 to oscillator 2 as S_{21}, where oscillator 1 is driven and the motion amplitude of oscillator 2 is monitored; the transmitted signal from oscillator 2 to oscillator 1 is defined as S_{12}. Fig.1(b) and (c) show the transmitted signal of this system for a linear and nonlinear system. One could clearly see that the transmitted signal is identical for two different transmission direction in linear coupled case ($\alpha = 0$) as it is a reciprocal system, shown in Fig. 5.1(b). While S_{21} and S_{12} shows differences with the appearance of nonlinear term ($\alpha = 2$) as shown inFig. 5.1(c) because the reciprocity is broken due to nonlinear coupling term in the system. Two peaks in the spectrum represent the eigenfrequency of oscillator 1 and 2.

This model gives us a clear clue of how nonlinearity impacts on the realization of asymmetric transmission. A high power of light intensity is required to breaking the reciprocity of the system in the conventional nonlinear optical materials due to small nonlinear coefficient. Also for the conventional nonlinear materials, thick object is in need to accumulate significant effects, hindering the miniaturization of optical devices. However, the mechanical nonlinearity can be achieved when the movement of objects is comparable to their thickness[56]. With the advancement of the nano-fabrication technology, the nano-object can be manufactured, which enables the access to mechanical nonlinearity with low power levels.

5.3 Optomechanical asymmetry in all-dielectric metamaterials: Numerical modelling

In this section, two types of nanomechanical metamaterials, consisting with nanowires of dissimilar thickness and nanobricks of dissimilar length, driven by optical forces are introduced to explore the basic principle of realizing optomechanical asymmetry and to find a practical design for the following experimental implementation.

The way to calculate optical forces acting on metamaterial structures can be found in the last section of Chapter 2. As shown in Fig. 2.20, normal incidence

condition with polarization along the beams direction is assumed in all of the following calculations. By modelling a single 'meta-molecule' with periodic boundary conditions, the optical properties of a planar metamaterial array with infinite extent can be obtained.

5.3.1 Nanowires of dissimilar thickness

In this section, a nanomechanical metamaterial consisting with nanowires with different thickness are utilized to produce optomechanical asymmetry. Simulation results reveal that this type nanomechanical metamaterials driven by optical forces are capable of offering a strong nonlinear optical response and delivering high contrast(the absolute transmittance difference between forward and backward illuminations is as high as 52.2%) asymmetric transmission at near-infrared wavelength regime.

Fig. 5.2 (a) and (b) give a schematic and dimensions, respectively, of the nanowires we studied. It is made of an array of 145 nm wide, 10.8 μm long Si strips with thicknesses alternating along y axis between 115 and 150 nm; these strips sit on Si_3N_4 beams with same width and uniform thickness of 100nm. The gaps between each other (along y direction) is 255 nm. Si_3N_4 beams extend, at a thickness of 50 nm, to fixed mounting points which is 15 μm from the edge of Si strips. As for the light source, x-polarized plane wave normally incident (along z direction) on the dielectric nanowires structure within a rectangular area (10.8 $\mu m\times$ 9.6 μm), with a total optical power P_0. Under such illumination, a sharp resonance in transmission spectrum presented at 1550 nm, see Fig. 5.2(b). The inset of this figure present electric distribution at 1550 nm showing anti-phase excitation of two Si strips. That imply the existence of Fano mode. Such mode can effectively suppresses radiation loss, resulting in sharp spectral resonance and large optical force. It can be seen from the inset of Fig. 5.3(a) that relative optical forces applying on a pairs of adjacent thick

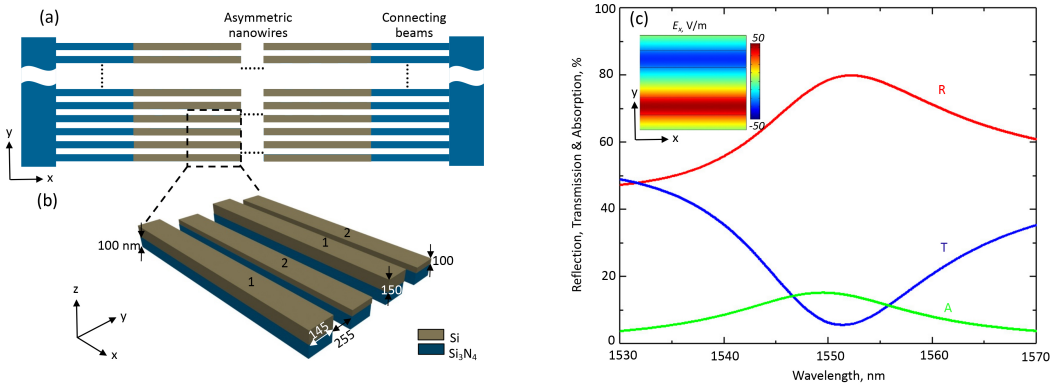

FIGURE 5.2: Linear properties of a nanomechanical metamaterial consisting with nanowires with dissimilar thickness. (a) Schematics and (b) dimensional details of the parallel Si_3N_4 nanowires. (c) Reflection (R), transmission (T) and absorption (A) spectrum under normally incident x-polarized illumination. Electric distribution for a cross-section of the unit cell in xy plane 50 nm above the interface between Si and Si_3N_4 at wavelength λ =1550 nm, showing anti-phase excitation of the two silicon beams underlying Fano resonance.

(150 nm) and thin (115 nm) Si strips for light impinging on the metamaterial in the forward(fwd) and backward(bwd) directions, defined respectively as being incident on the Si strips and supporting Si_3N_4 beams sides of the structure. A significant difference in optical forces dispersion (Fig. 5.3(a)) is found between fwd and bwd illumination conditions. In both cases, the optical forces will drive the supporting beams to move up or down until they are balanced by elastic forces. The equilibrium position between neighboring beams, therefore, will be different when sending light from different sides of the nanomechanical metamaterials as relative optical force show different magnitude and sign, see Fig. 5.3(a). This will finally give birth to optomechanical asymmetry.

Numerical simulations show that out of plane (along z direction) mechanical displacement (Δz) of Si_3N_4 beams is around 63 nm as a 100 pN force (F) is applied

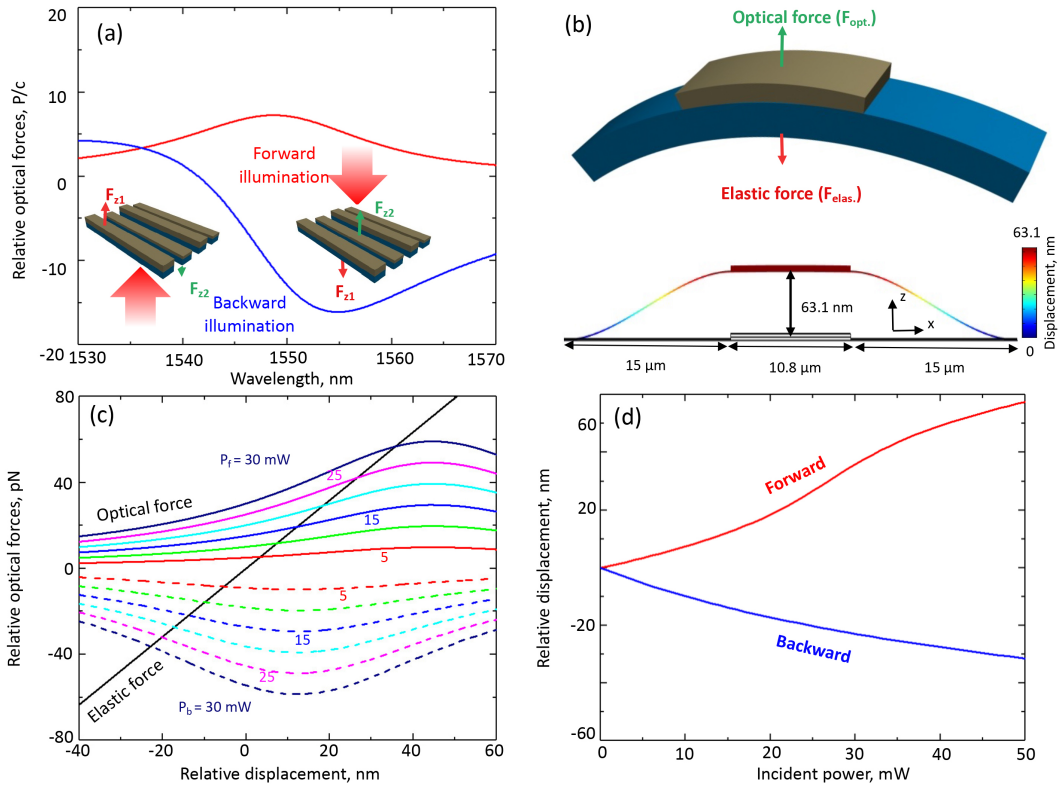

FIGURE 5.3: Asymmetric optomechanical force in a nanomechanical metamaterials consisting with nanowires of dissimilar thickness. (a) Spectral dispersion of the relative optical force ($F_{opt.}^{cell}$) on the two beams of a single unit cell for both forward ($-z$) and backward ($+z$) directions of light propagation. Optical forces are presented in unit of P/c, where $P = P_0/N^2$ is the incident power per unit cell, P_0 is the total power incident on the metamaterial array of N^2 cells, c is the light speed in free space. (b) Elastic deformation of a suspended beam for a force of 100 pN. Top: schematics for suspended beam. Bottom: Calculated elastic displacement. NB: the vertical scale is exaggerated by more than two orders of magnitude. (c) Dependence of the relative optical force ($F_{opt.}^{beam} = 12(F_{opt.}^{cell})$ on the mutual out-of-plane displacement of neighbouring Si_3N_4 beams supporting thick and thin silicon nanowires under 1550 nm forward (solid lines) and backward (dashed lines) illumination at a range of incident power levels P_0 (as labeled). The straight black line indicates to opposing elastic force. (d) The balance positions as a function of a range of total incident powers (p_0) at 1536 nm.

to the central 10.8 μm long nanowire section.(See Fig. 5.3(b)). The mechanical properties of Si and Si_3N_4 used in simulations can be found in Table 4.1. Therefore, the spring constant (κ) associated with two fixed beams is given by:

$$\kappa = \frac{F}{\Delta z} \tag{5.3}$$

The relationship between elastic force ($F_{elas.}$) and mechanical displacement (Δz) then can be obtained once the spring constant(κ) of current designs acquired via eq. 5.3. Here, bending mainly happens within side connecting arms (50 nm thick) and the displacement within central nanowires section (100 nm thick) can be ignored. Hence, It is reasonable to assume the central nanowire section of each beam moves up and down (along z axis) without changing shape.

Equilibrium condition need to be taken into account when calculating final transmission differential. In order to achieve stable equilibrium (assuming the displacement at equilibrium is Z_0), optical force on beam ($F_{opt.}^{beam}|_{Z_0}$) should be equal to elastic force ($F_{elas.}|_{Z_0}$). Apart from this, they also should satisfy the conditions that $F_{opt.}^{beam}|_{Z_0-\Delta Z} > F_{elas.}|_{Z_0-\Delta Z}$ and $F_{opt.}^{beam}|_{Z_0+\Delta Z} < F_{elas.}|_{Z_0+\Delta Z}$. Fig. 5.3(c) shows the relations of relative optical force acting on two neighbouring beams $F_{opt.}^{beam}(= NF_{opt.}^{cell}, N = 12)$ on relative displacement Z in the vertical direction for a group of incident light power at 1550 nm. Balance points can be found at the intersection points between elastic force (black line) and optical force. For example, stable equilibrium can be achieved for forward illumination of light with a power of 30 mW at a relative displacement of 36 nm. While a relative displacement of 23 nm are required for the backward illumination at the same power. This different out-of-plane displacement can be seen in Fig. 5.3(d) unambiguously, where the intersection points in Fig. 5.3(c) are drawn and shown dependence between balance displacement and incident light power for forward and backward light propagation directions.

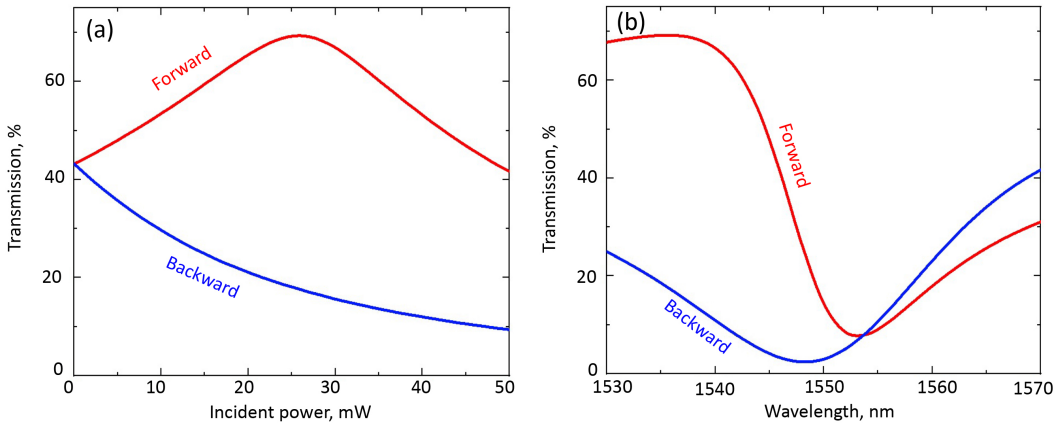

FIGURE 5.4: Asymmetric transmission properties. (a) Optical transmission as a function of total incident powers (P_0) at 1536 nm. (b) Transmission spectral dispersion for forward and backward at incident power of 27 mW.

This asymmetric displacements upon different illumination conditions lead to asymmetric transmission, see Fig. 5.4(a). For the forward propagation, transmission increases from 43.2% to 69.5%at a power of 26 mW and then goes down to 41.7% at 50 mW; In contrast, backward incidence optical transmission keeps dropping from 43.2% to 9.4% at 50 mW, offering a forward: backward absolute transmission difference ($\Delta T = T_{forward} - T_{backward}$) around 52.2% at operating wavelength 1536 nm with power of 27 mW. Fig. 5.4(b) shows the transmission spectra under fwd and bwd illumination at its equilibrium positions, the incident power is fixed at 27 mW. One can see that the resonance get slightly shifted and the amplitude of transmittance is quite difference, which give maximum transmission asymmetry at wavelength of 1536 nm.

Even this type of metamaterials can give us a good transmission asymmetry, it is difficult to manufacture corresponding structures, in which optical resonance with good quality factor can be observed. The most time-saving fabrication way is FIB, however, the Ga^+ implantation in materials gives large losses, which undermine the resonances. Fig. 5.5 shows that the influence from losses on transmission spectra (a) and relative optical forces(b). In Appendix E, a nanowire sample with different thickness fabricated and there is no desired resonance observed in the transmission and reflection spectrum. Previously in our group, Savinov et. al. managed to produce a metamaterials on fibre facet with good quality factor around 300 by pattern grooves on sillica via FIB and then deposit a-Si on it to reduce Ga^+ pollution[103]. Inspired by this idea, we also try to use post material deposition to create our samples, see the last part in Section 2.1.1. However, such small width difference of neighbouring beams is not enough to create desired thickness difference (see Fig. 2.4). Another issue, as I mentioned before, is the non-uniform tensile distribution built inside Si_3N_4 layer during milling process, which makes the membrane very easy to be broken during Si deposition process (200^oC temperature is required for PECVD deposition). In terms of EBL process, the greyscale processes would be

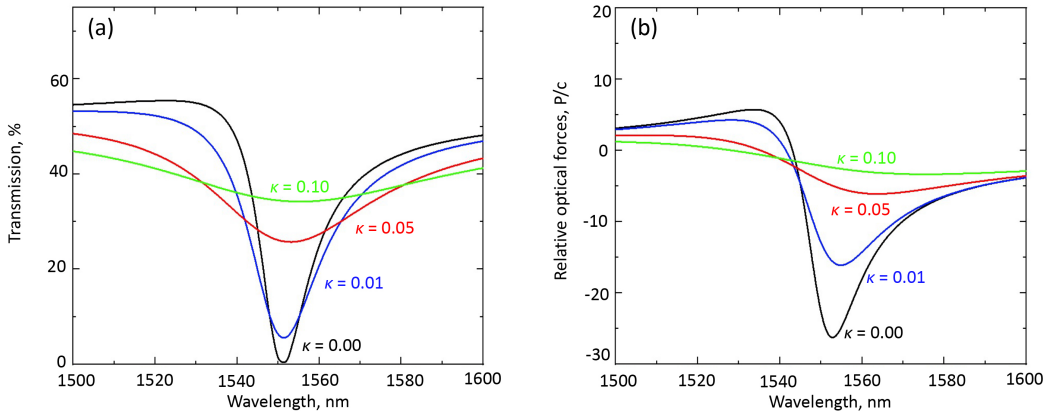

FIGURE 5.5: Influences from materials' losses. (a) Optical transmission spectra for different imaginary part (κ) of refractive index. (b) Corresponding relative optical forces dispersion. Note: Backward illumination is considered and there is no relative displacement between neighbouring beams.

required to generate different thickness, making the manufacturing process quite complex and time-consuming. Therefore, I try to find another type of nanomechanical metamaterials that is easy to be fabricated and possess similar optomechanical asymmetry.

5.3.2 Nanobricks of dissimilar length

In this section, nanomechanical metamaterials consisting with nanobricks as meta-molecules are utilized to realize optomechanical asymmetry. In which the absolute transmittance difference between fwd and bwd illumination is around 61.6%, which is even higher than the previous design(52.2%). Furthermore, this structure, e.g. nanobricks with different length, are easier to be fabricated and more tolerant with losses induced by Ga^+ implantation. All of these merits make this design preferable from experimental aspects.

Fig. 5.6 (a) and (b) give a schematic and dimensions of nanobrick metamaterials under consideration. It is made of a 12 (along x axis)×24(along y axis) array of 250 nm wide, 115 nm thick Si nanobricks with length alternating along y direction between 580 nm and 500 nm; they are supported on Si_3N_4 beams with same width and thickness of 300 nm, the gaps between each other (along x direction) is 200 nm. like previous case, in order to obtain large displacement and remain metamaterials flat, Si_3N_4 beams extend, at a thickness of 50 nm, to fixed mounting points which is 15 μm from outside edge of Si strips. As for the light source, x-polarized plane wave normally incident (along z direction) on the nanobrick structure within a square area (10.8 μm×10.8 μm), with a total optical power P_0. Under illumination, a sharp resonance in transmission spectrum presented at 1550 nm, see Fig. 5.6(c). The inset of this figure present electric distribution at 1550 nm implying this high Q factor resonance from trap mode. Also, only out-of-plane force (along z axis) are taken into consideration.

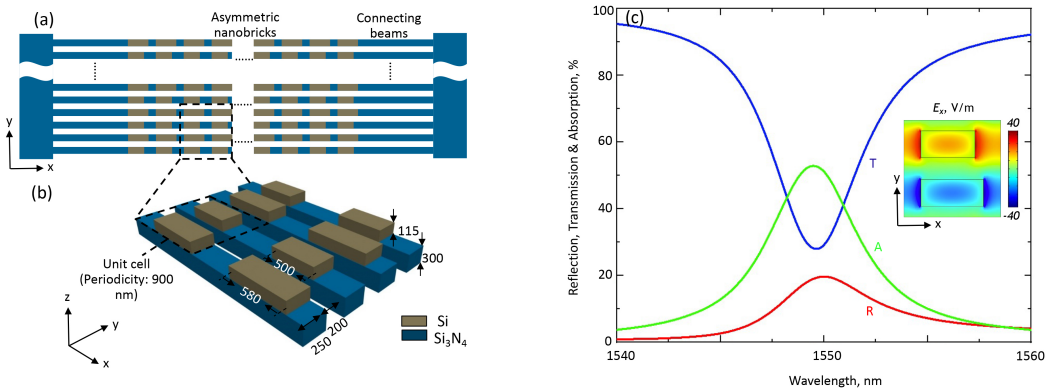

FIGURE 5.6: Linear properties of a dielectric nanobricks metamaterial. (a) Schematics and (b) dimensional details of the parallel Si_3N_4 beams and asymmetric Si nanobricks. (c) Reflection(R), transmission(T) and absorption(A) spectrum under normal incident x-polarized illumination. Electric distribution for a cross-section of the unit cell in xy plane, 50 nm above the interface between Si and Si_3N_4 at wavelength λ =1550 nm, showing anti-phase excitation of the two silicon nanobricks.

Fig. 5.7(a) shows asymmetric relative optical forces applying on a pairs of adjacent long (580 nm) and narrow (500 nm) Si strips when send light from fwd and bwd directions, giving rise to asymmetric transmission. Numerical simulations show that out-of-plane mechanical displacement (Δz)of Si_3N_4 of beams is around 39 nm when a 100 pN force (F) is applied to the central 10.8 μm metamaterials section, see Fig. 5.7(b). The displacement here becomes smaller than previous nanowires case, because the width of beams increase from 115 nm to 250 nm and the thickness of beams goes up to 415 nm in total. The relationship between elastic forces $F_{elas.}$ and out of plane displacements Z then can be derived via eq. 5.3, which can be found in Fig. 5.7(c) [black solid line]. It also shows the dependence of relative optical force acting on two neighbouring beams $F_{opt.}^{beam}(= NF_{opt.}^{cell}, N = 12)$ on relative displacement Z in the vertical direction for a selection of incident light power at 1550 nm. The intersections (equilibration positions) between elastic force and optical force are

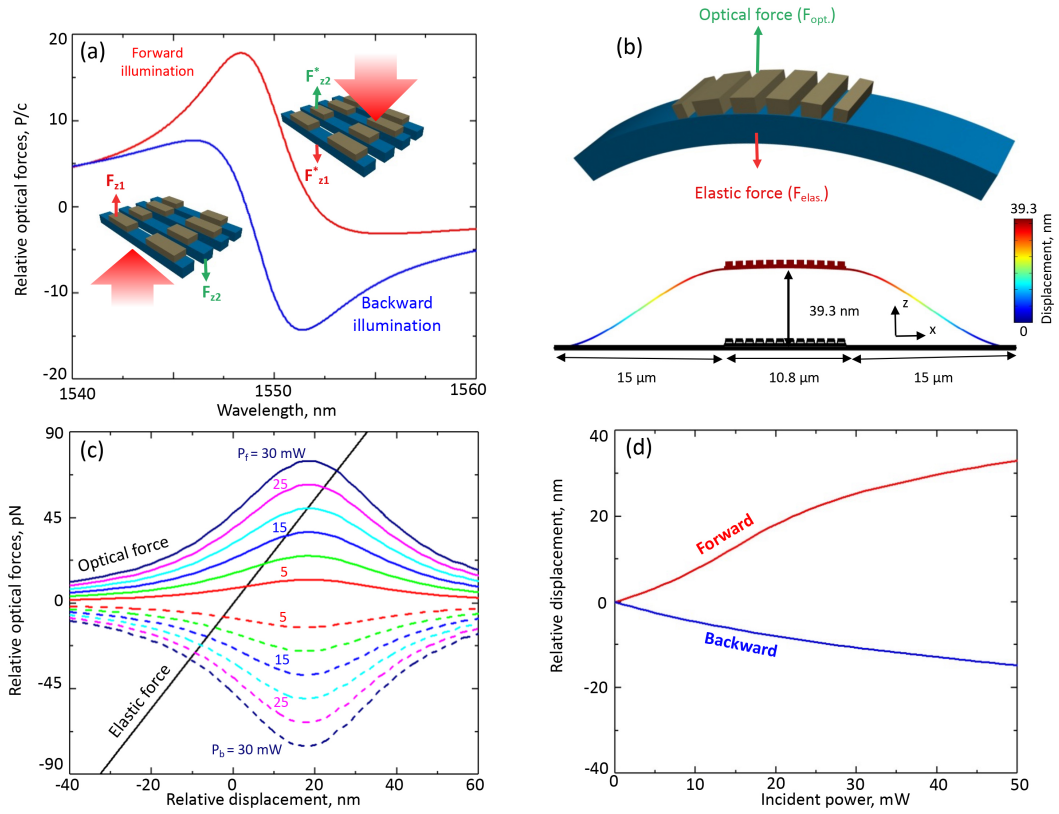

FIGURE 5.7: Asymmetric optomechanical force in a dielectric nanobricks metamaterial. (a) Spectral dispersion of the relative optical force on the two beams of a single unit cell for both forward and backward directions of light propagation. (b) Elastic deformation of a suspended beam for a force of 100 pN. Top: schematics for suspended beam. Bottom: Calculated elastic displacement. NB: the vertical scale is exaggerated by more than two orders of magnitude. (c) Dependence of the relative optical force ($F_{opt.}^{beam} = 12(F_{opt.}^{cell})$ on the mutual out-of-plane displacement of neighbouring Si_3N_4 beams supporting short and long nanobricks under 1550 nm forward (solid lines) and backward (dashed lines) illumination at a range of incident power levels P_0 (as labeled). The straight black line indicates to opposing elastic force. (d) The balance positions as a function of a range of total incident powers (P_0) at 1548 nm.

redrawn in Fig. 5.7(d). A difference in the mechanical displacement with fwd and bwd light propagation can be clearly observed.

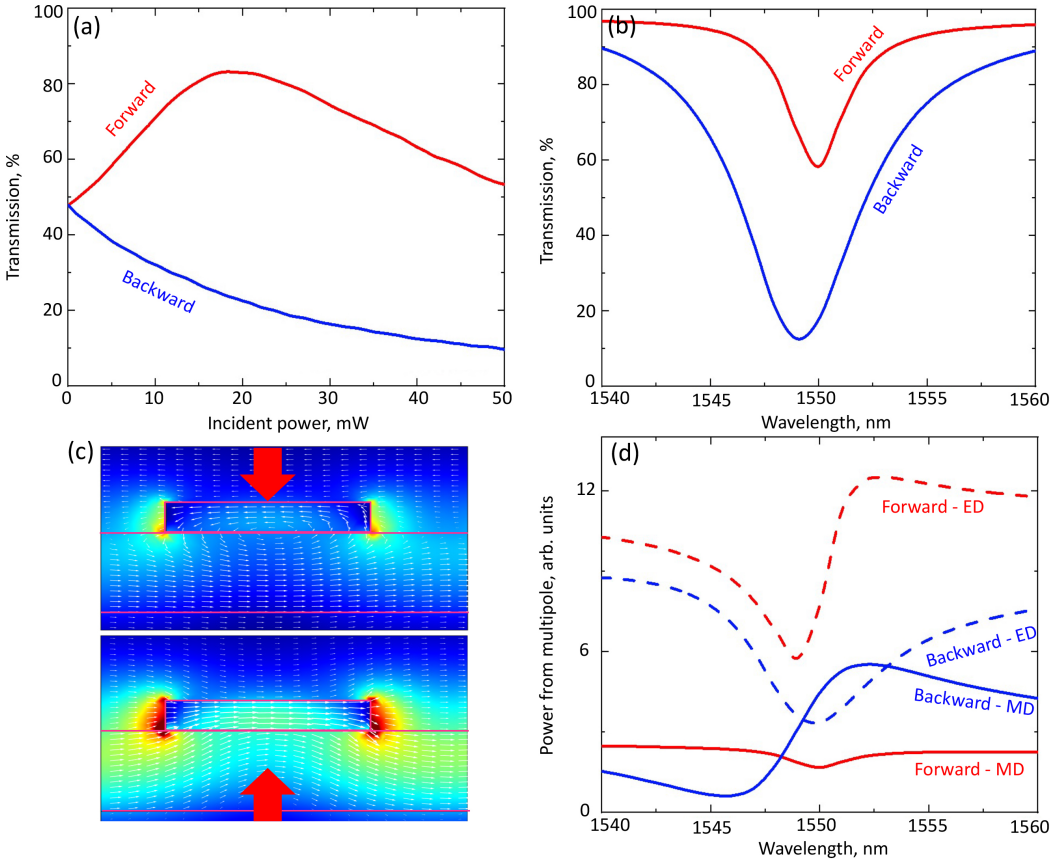

FIGURE 5.8: Asymmetric transmission properties. (a) Optical transmission as a function of total incident powers (P_0) at 1548 nm. (b) Transmission spectral dispersion for forward and backward at incident power of 22 mW. (c) Magnetic field map for forward and backward light illumination, differnt colour shows the magnetic field magnitude and arrows shows magnetic fields. (d) Multipole decomposition for transmission spectra of opposite illumination directions.

As a result of this asymmetric movement, the nanobrick metamaterials alters their optical properties as shown in Fig. 5.8(a). Regarding fwd illumination, transmission increases from 47.9% to 83.3% at a power of 18 mW and then goes down to 53.4% at 50 mW; In contrast, backward incidence optical transmission keeps dropping from 47.9% to 9.7% at 50 mW, offering a maximum forward: backward absolute transmission difference ($\Delta T = T_{forward} - T_{backward}$) around 61.6% at operating wavelength 1548 nm with power of 22 mW. Fig. 5.8(b) shows the transmission spectra under fwd and bwd illumination at its equilibrium positions (25.3 nm for fwd illumination and 10.7 nm for bwd illumination) with power of 22 mW. One can see that the resonance get slightly shifted and there is a distinct difference in the amplitude of transmittance for two opposite illuminations at wavelength of 1548 nm.

In order to gain better understandings of the origin of asymmetric transmission, I conduct multipole decomposition for the spectra shown in Fig. 5.8(b), the details of

mulitpole decomposition can be found in Chapter 2. One could see from Fig. 5.8(d) that for the forward illumination, electric dipole dominates, while for the backward illumination, electric dipole and magnetic dipole shows similar amplitude and they are interfere each other destructively and finally give rise to low transmission in the spectrum. Due to different contributions from multipoles for fwd and bwd illumination, asymmetric transmission can be achieved by tens nanometers movement differences of neighbouring beams. The corresponding magnetic field H_y (shown in different colours) with vector field (shown in white arrows) can be found in Fig. 5.8(c), the shape of nanobricks and beams are outlined with pink solid lines. one could clearly see magnetic circular current for forward illumination, indicating the dominant role of electric dipole.

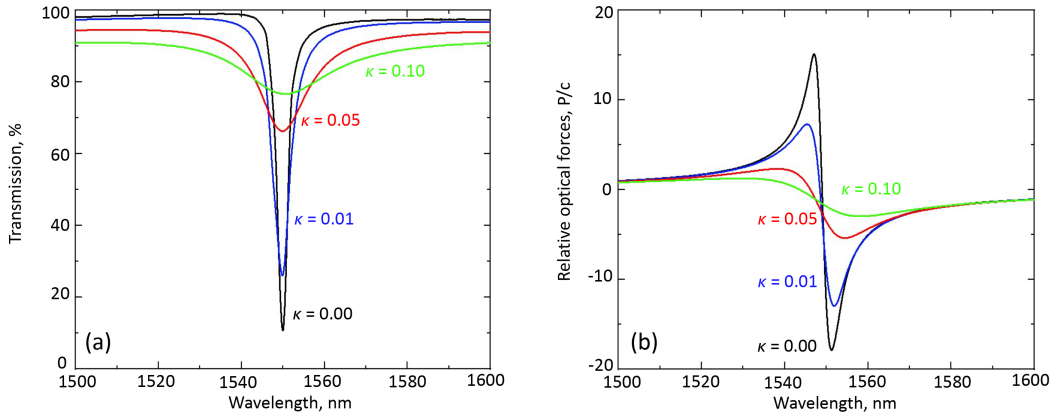

FIGURE 5.9: Influences from Si losses on nanobricks metamaterials. (a) Optical transmission spectra for different imaginary part (κ) of complex refractive index. (b) Corresponding relative optical forces dispersion. Note: Backward illumination is considered and there is no relative displacement between neighbouring beams.

Furthermore, It would be necessary to check if current design would be more tolerant than that with different thickness in previous section to the losses induced by FIB milling process. therefore, we simulated the transmission spectra and relative optical forces spectra for the nanobricks design, see Fig. 5.9. It can be seen from Fig. 5.9(a) that higher quality factor can be observed for a fixed extinction coefficient in comparison with the nanowire design (Fig. 5.5(a)) and the optical forces is also less sensitive to the losses. On the other hand, stand EBL process can handle this nanobricks design, paving a way to further improve the optical response of this kind of nanomechanical metamaterials, see my effort on fabricating this type of nanomechanical sample via EBL process in Section 2.1.2.

A series of parameters of nanobricks metamaterials (including length, and thickness of nanobricks and supporting beams) are swept to find out the optimum conditions for both easy fabrication process and large asymmetric transmission. Here we show the length sweep outcome as an example, one can find the other parameters sweep outcomes in the appendix D.

Here, Fig. 5.10(a) shows the transmission spectra for the nanobricks with a group of short beam length (L_1) under backward illumination. The long beam length is

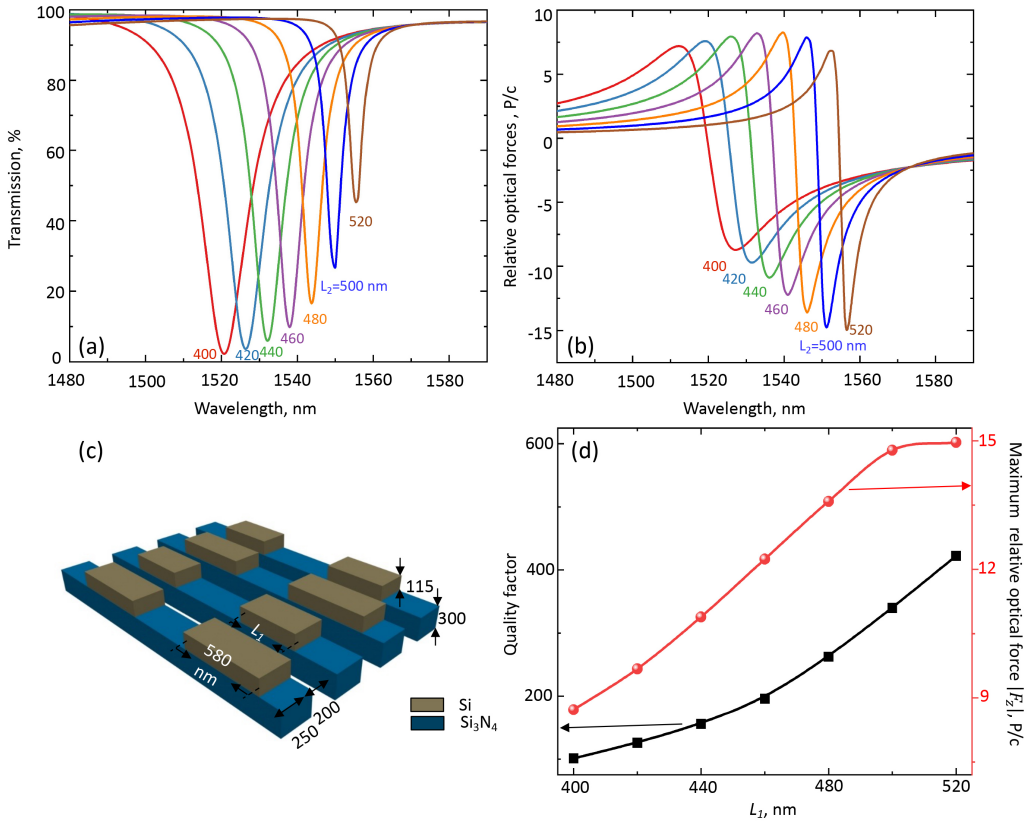

FIGURE 5.10: Influences from length of nanobricks on metamaterials. (a) Optical transmission spectra for different length of nanobricks (L_1). (b) Corresponding relative optical forces dispersion. (c) The schematics of structures, bricks with varible length is annotated by L_1. (d) Evaluated quality factors and maximum relative optical forces. Note: backward illumination is considered here and there is no relative displacement between neighbouring beams.

fixed as 580 nm. One can see that the resonances of nanobricks metamaterials are red-shifted with the growth of short nanobricks' length, that is because the effective index of entire system increase. Corresponding spectral dispersion of relative optical forces are depicted in Fig. 5.10(b). The maximum absolute values of L_1 relative forces between neighbouring beams increase to 14.96 P/c at $L_1 = 520\ nm$. In order to visualize the Q factor trend during the sweeping process of L_1, I use a Fano model to extract the Q-factor [104], [105] of these resonances from the nanobrics metamaterials. The Simulated transmittance is fitted to a Fano line shape given by $T_{Fano} = a + jb + \frac{c}{\omega - \omega_0 + j\gamma}$, where a, b and c are constant real number and ω_0 is the central resonant angular frequency, γ is the overall damping rate of the resonance. The extracted Q-factors for different L_1 are plotted in Fig. 5.10(d) (black curve), where Q-factors go up from 101 to 422 when L_1 varies from 400 to 520 nm, which are consistent with the previous literatures [106], [107]. The maximum absolute value of relative forces is 14.96 P/c at $L_1 = 520\ nm$, corresponding to the resonance wavelength of 1556 nm. As our design targets at wavelength of 1550 nm, the length are slightly adjusted to 500 nm in proposed design to make the resonance locating at targeting wavelength without changing the relative optical

force ($14.78P/c$ at L_1 =500 nm) dramatically. That is to say, the current design is around the optimum conditions. Hence, I can take this design as a reference for the sample fabrication in the following experiment for investigating asymmetric transmission in nanomechanical metamaterials.

5.4 Experimental observations: pump-induced changes in probe transmission

Below we experimentally examine asymmetric transmission features of all-dielectric nano-opto-mechanical metamaterials. The SEM image of metamaterial sample can be found in Fig. 5.11(a) and it was fabricated on a 200 nm thick silicon nitride membrane coated with a 115 nm layer of amorphous Si. This bilayer was then structured by FIB milling to obtain array of asymmetric nanobrick pairs in the si layer, on 15.5 μm long Si_3N_4 beams. The dimensional details can be found in the inset of Fig. 5.11(a). And two types of beams are designated as ①, ② for the wide beam with long nanobricks and the narrow beam with short nanobricks, respectively. This designation is consistent with that in chapter 4. The structure supports a Fano resonance to enhance the optical forces. Fig. 5.11(b) show reflection, transmission and absorption spectrum of this sample for the incident light with polarization along y - direction, in which a resonance near 1535 nm can be observed, meeting our C-band tunable laser wavelength range well. That enables experimental observation of asymmetric transmission in nanomechanical metamaterials because transmission differences will gradually vanish when the operation wavelength move away from metamaterials' resonance, see Fig. 5.8(b) for the static displacement case.

As we aim to study the directional dependent transmission of the metamaterials, this can be done by either flipping over the sample or swapping the light illumination directions. Flipping sample could inevitably introduce systematic errors. An example of this is the slight difference in transmission spectra for fwd and bwd illumination in Fig. 4.1(b). Hence, a MEMS switch is utilized to swap the incident light illumination direction between forward and backward light illuminations without moving or adjusting either the sample or any other component in the beam path(Fig. 5.11(c)). The sample is under low vacuum (down to 4.5×10^{-3} $mbar$ to reduce air damping of nanoscale movement), and the same arrangement of optical components on either side of the sample is arranged to ensure the symmetry of the system. C-band laser is decoupled into free space via a fibre collimator and focused onto the sample by a 20× magnitude with long working distance (20 mm) objective and focused spot size is around 5 μm. Transmission of continuous probe beam is measured while sweeping the modulation frequency of a coincident pump beam across a range encompassing the natural mechanical resonances of the nanostructure. Different pump (λ = 1535 -1560 nm) and probe (λ =1540 nm) wavelengths are selected to facilitate isolation of transmitted probe signal using a tunable bandpass filter and a network analyzer is then exploited to record the transmitted signal.

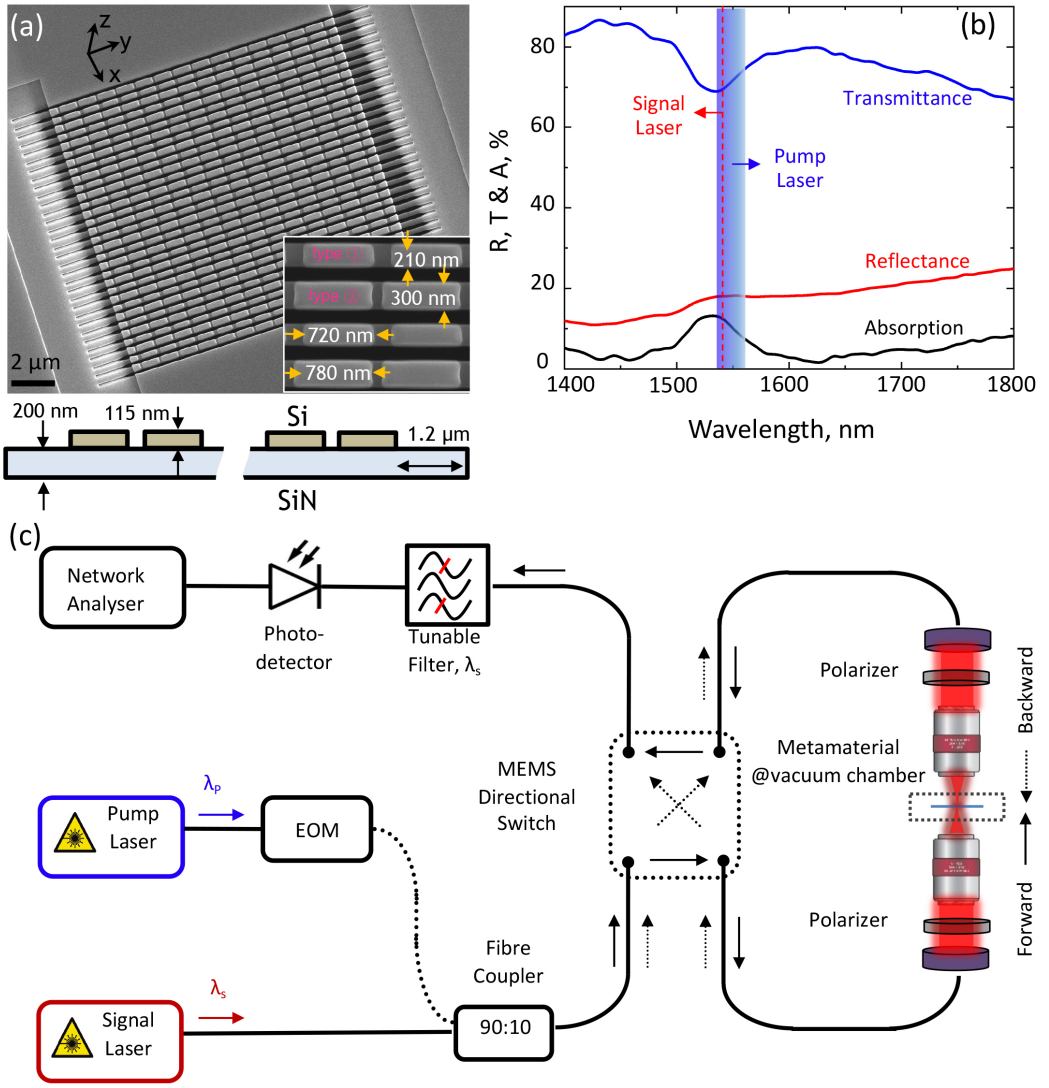

FIGURE 5.11: Characterization of nano-opto-mechancial metamaterials. (a) SEM image of the nanomechanical metamaterials, fabricated on a 15.5 μm wide free-standing Si_3N_4 membrane. The inset shows the zoom-in section, giving the dimensional details along x-y plane of the supported Si nano-bricks; thickness information along z - direction of this sample can be found in a schematic below this figure. Also two types of beam with wide and narrow width labelled as type ① / ② for the convenience of investigation. (b) Reflection, transmission and absorption spectrum of the metamaterials, where a resonance at around 1535 nm can be observed; the signal and pump laser range is indicated with dashed red line and blue shadowed area, respectively. (c) Schematic of apparatus for asymmetric transmission measurement, pump and probe laser are coupled in polarization-maintaining single-mode optical fiber, and a MEMS switch providing for flipping of the laser propagation direction through the sample. The designation of forward(fwd) and backward(bwd) is the same like in chapter 4.

The fundamental out-of-plane mechanical modes of the metamaterial are firstly identified (see Fig. F.1(b) in Appendix F) via the approach utilized in Chapter 3. Furthermore, the power dependence of their Eigenfrequencies are also investigated(Fig. F.1(d),(e)), showing the same trend as in the Chapter 4. Moreover, the eigenfrequencies of beams for fwd and bwd illumination directions gradually

converge to the same frequencies with the decrease laser power (see F.1(f)), indicating a good symmetry and stability of the current measurement setup for opposite illumination conditions.

5.4.1 Nanostructural reconfiguration driven by ponderomotive optical forces

As modulation of transmitted light induced by thermal forces is usually less than 1%[96], external stimulus are required to drive the nano-opto-mechanical metamaterials efficiently. Here, a pulsed pump laser is introduced to provide ponderomotive optical forces for reconfiguring the nanomechanical metamaterial sample shown in Fig. 5.11(a). The setup shown in Fig. 5.11 (c) is utilized to investigate the contribution from thermal forces and optical forces, in which the network analyzer is replaced by a spectral analyzer to record the time-resolved fluctuations of transmission.

The pulsed pump laser frequency is firstly set as a fixed value of 6.385 MHz and the pump laser power is tuned from 0 to 61.25 μW. Tuning of mechanical eigenfrequencies is observed again(see two faint diagonal bands across the amplitude spectral density (ASD) mapping shown in Fig. 5.12(a)) as in Chapter 4, but now with increasing of pump power, indicating the fact that time-averaged heating effect

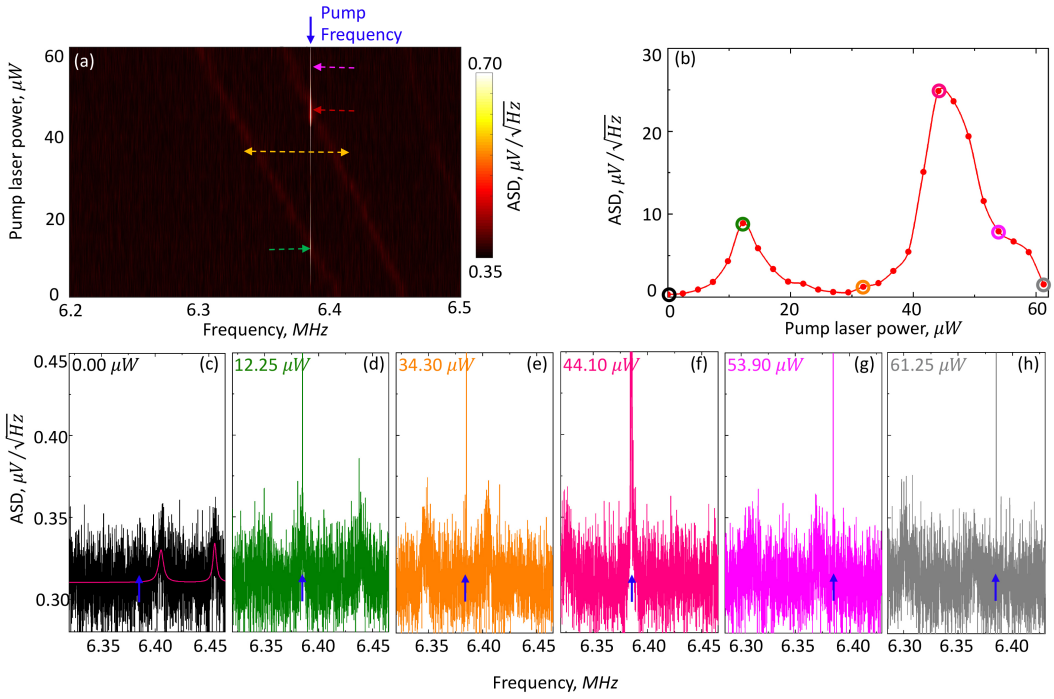

FIGURE 5.12: Nanomechanical metamaterials driven by thermal and optical forces on forward illuminations. (a) ASD of the metamaterials for different pump power with fixed pulsed pump frequency of 6.385 MHz and pump wavelength of 1535 nm, the CW probe wavelength is 1540 nm and probe power is 57.6μW. (b) The magnitude of amplitude spectral density as a function of pump laser power at 6.385 MHz. (c)-(h) Zoom-in ASD at pump power of $0, 12.25, 34.3, 44.1, 53.9$ and 61.25 μW, corresponding power position is indicated in (a) and (b) by arrows and circles, respectively, with different colours. The blue arrows indicating the position of pump frequencies.

of the modulated pump laser with changing peak power here is the same as the effect of CW probe laser with changing power in Chapter 4 experiments.

Optical forces generated by the pulsed pump beam induce out-of-plane displacements of beams, giving rise to a change in transmission for a CW probe beam. This all-optical light-by-light modulation is seen against the backdrop of optically-induced thermal tuning of the beams' natural eigenfrequencies shown in Fig. 5.12(a). Specifically, When two thermal induced peaks meet the pump laser frequency (here, 6.385 MHz indicating by blue arrow in Fig. 5.12(a)), the amplitude dramatically amplified, shown as the sharp spikes in Fig. 5.12(a), by pump-induced ponderomotive optical force. Once the thermal peaks move away from pump frequency, this enhancement gradually disappeared. Fig. 5.12(b) shows amplitude of ASD at pump frequency (6.385 MHz) as a function of pump power, in which two peaks observed, belonging to the fundamental out-of-plane modes of two types of beam ① and ② in nanomechanical metamaterials. One could see that enhanced amplitude contributed from optical forces is around 25 and 126 times larger than that contributed from thermal peaks at pump power of 12.25 μW and 44.1 μW, respectively. That means the mechanical oscillators are driven dominantly by optical forces in the current measurement. On the other hand, the pump modulation frequencies (around 6 MHz) are too high for coherent temperature oscillation, and the dispersion of transmission modulation to low frequencies is confirmed in Fig. G.1 of Appendix G, finding that

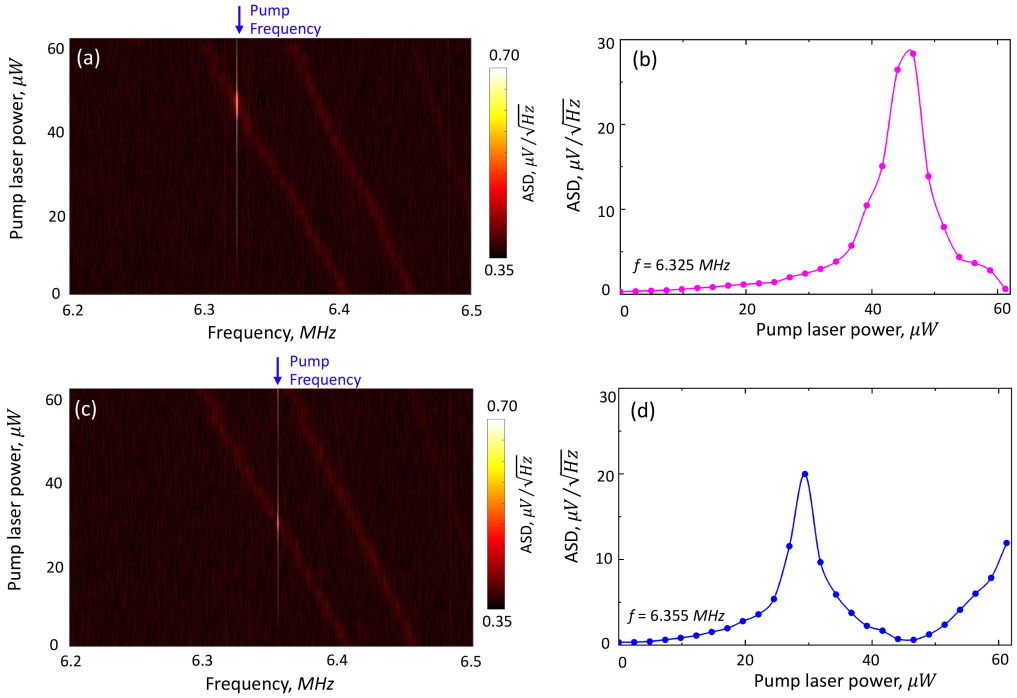

FIGURE 5.13: Comparison of contribution of asymmetric transmission from thermal and optical forces. (a)(c) ASD of the metamaterials for different pump powers with fixed pulsed pump frequency of 6.325 MHz (a) and 6.355 MHz (c), where pump and probe wavelength is 1535 nm and 1540 nm, respectively; probe power is 57.6 μW. (b) (d)The magnitude of ASD as a function of pump laser power at 6.325 MHz (b) and 6.355 MHz (d).

the noise floor at around 6 MHz is 2 orders of magnitude below the magnitude of kHz frequency thermally-driven fluctuations. Fig. 5.12(c)-(h) give the spectral profiles at six typical power levels, in which one could see the evolution of contribution from optical forces to the modulation of transmitted light, setting an essential basis of the observation asymmetric transmission in next section.

The pump frequency are also tuned to 6.325 MHz and 6.355 MHz and the same experiment as shown in Fig. 5.12 is conduct. Relevant experiment results can be found in Fig. 5.13, showing similar enhancement trends for both of these two pump frequencies. However, only one peak observed in Fig. 5.13(b) and (d) due to the relative spectral position of thermal peaks and pump frequencies. Another interesting phenomena observed here is the enhanced amplitude is also related to the average power of pump laser. One could see that the amplitude of enhanced ASD in Fig. 5.13(b) is around 28.3 $\mu V/\sqrt{(Hz)}$ at average pump laser power of 46.55 μW for the beam type ①, while that in Fig. 5.13(d) is around 20 $\mu V/\sqrt{(Hz)}$ at average power of 25.4 μW. This enhanced amplitude is further decreased to 8.91 $\mu V/\sqrt{(Hz)}$ at average power of 12.25 μW in Fig. 5.12(b) for the same beam type ①. The reason behind this observation originates from the fact that magnitude of optical forces is proportional to the input light power as shown in Fig. 5.7(c). Hence, the higher of incident power level, the larger of modulated transmitted light observed. It need to be noted that the amplified ASD amplitudes are not strictly proportional to the incident powers, because of non-uniform offsets between thermal peak frequencies and the fixed pump frequencies for different pump powers.

In conclusion, this experiment demonstrate that resonant ponderomotive optical forces can be utilized to efficiently control the optical response of a nanomechanical metamaterial. Strong optical nonlinearity achieved via coupling of optical and mechanical subsystem of nanomechanical metamaterials offers an opportunity to achieve all-optical transmission modulation at ultra-low power levels.

5.4.2 Transmission asymmetry driven by optical forces

Once the key role of ponderomotive optical forces in modulation of transmitted light is confirmed, another pump-probe experiment is conducted for exploring transmission asymmetry response of the nanomechanical metamaterials based on the setup shown in Fig. 5.11(c). In this experiment, the modulation frequency of pump light is continuously swept with step of 500 Hz and transmitted probe light is recorded by a network analyzer. Fig. 5.14 gives experimental evidence for transmission asymmetry in the nanomechanical metamaterial with two opposite illumination directions, where modulation depth of transmitted probe light is shown for forward (Fig. 5.14(a)) and backward (Fig. 5.14(b)) illumination direction. Here, the pump laser power varies from 0 to 61.25 μW while the probe laser power is fixed at 43.2 μW. Besides, modulation frequency of pump light ranges from 6.2 to 6.5 MHz, covering most of spectral features we observed. In these mappings of the transmitted probe signal, we observe two main peaks at closely-spaced frequencies identifiable as those

of the out-of-plane bending modes of beam type ① and② . In addition to these main peaks, there are also peaks with weak response revealing complex patterns of coupled oscillations underpinned by a combination of, pump and probe power and wavelength dependent, light-induced heating and optical forces. All of these eigenmodes for forward and backward illuminations shifted to lower frequency range with the increase of incident pump power like we observed in both Fig. F.1(d) and (e), Fig. 5.12(a) and Fig. 5.13(a)(c). And also different shifting rate of eigenfrequency for backward and forward illumination is observed like Fig. F.1(d) and (e). on the other hand, with the increase of pump power, the modulation depth for forward grows from 0 to 9.6% and that for backward illumination goes up from 0 to 11.2%. I take a group frequencies corresponding to the peak intensity of two eigenmode for backward illumination, and then draw the absolute value of modulation depth difference for transmitted probe light between forward and backward illumination in Fig. 5.14(c). And there are four peaks appearing at this evolution spectra, which is related to the two eigenmodes in opposite illuminations. And the maximum differences in modulation depth of transmission is 10.84% at frequency of 6.2155 MHz with pump power of 58.8 μW (intensity is 2.99 $\mu W/\mu m^2$).

As we mentioned that the resonant enhanced ponderomotive optical forces play a key role in characterization of asymmetric response of nanomechanical metamaterials. Large modulation depth of transmitted light originates from the interaction between thermal tuned mechanical mode and optical forces as shown in Fig. 5.12(a). Let's consider the case that there is only the contribution from optical forces, then the displacement induced by optical forces for forward illumination is larger than

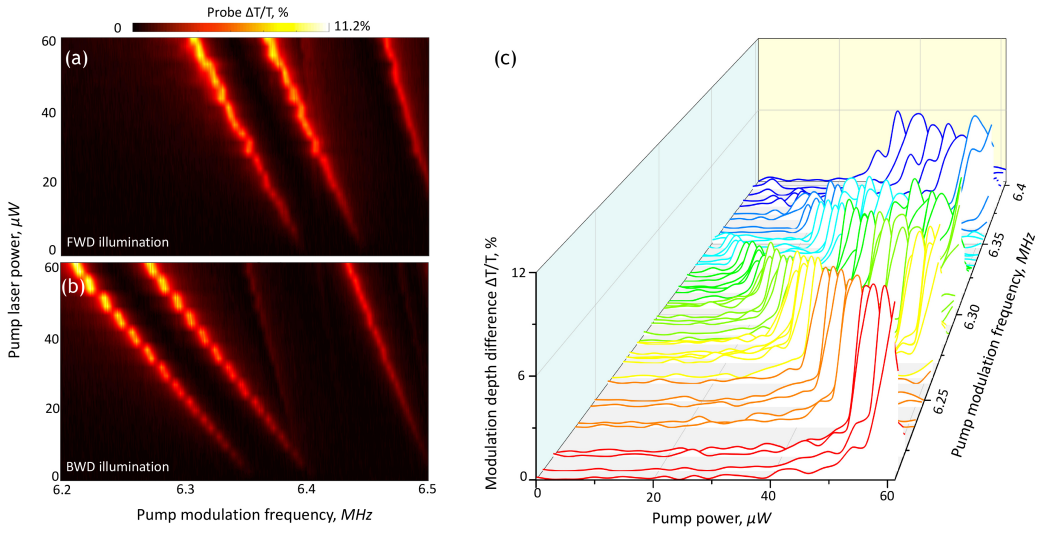

FIGURE 5.14: Experimental observation of asymmetric transmission on nano-opto-mechancial metamaterials. (a)(b)Modulation depth mapping of probe light as a function of pump laser power and pump modulation frequency for the forward (a), backward (b) illumination. (c) A line graph for absolute transmission difference at different pump laser power at a series of pump frequency, where transmission difference maximized at given input powers.

that for backward illumination(Fig. 5.7(a)). Therefore one would expect larger modulation depth for forward illumination in comparison with that for backward illumination. However, observed amplitude of modulation for forward (10.8%) is slightly smaller than that for backward(11.2%) illumination at the wavelength 1535 nm. There are two reasons behind this phenomena, one is that the thermal force induced displacement for forward is less than backward illumination due to different absorption cross section for these two illuminations (see Fig. 5.16(b)); the other is that the optical forces dispersion could also be altered by different dimensions between the initial designed pattern and final fabricated sample. Simulated optical forces based on actual dimension of nanomechanical metamaterials can be found in Fig. 5.16(c).

The change trends for the forward and backward illumination are expected to be different with the change of pump laser wavelength due to distinct optical forces dispersions (see Fig. 5.16(c)) for opposite illumination directions. To verify this assumption, we conduct pump-probe experiment with different pump wavelengths varying from 1535 nm to 1560 nm. Fig. 5.15 shows the modulation depth of transmitted light for forward (a) and backward (b) light illumination at these different pump wavelengths. One can see that the amplitude of modulation depth decrease for both forward and backward illumination with the increase of wavelength. However, the decrease rate of modulation depth belonging to beam type ① for forward is faster than that for backward illumination in Fig. 5.15(c). The maximum modulation depth for forward illumination decrease from 10.8 % (at 1535 nm) to 1.8% (at 1560 nm), while that for backward illumination decrease from 11.2 % to 3.4 %. This different rates can be explained based on simulated absorption and optical forces dispersion. One can see from Fig. 5.16(c) that optical forces dramatically decrease to a

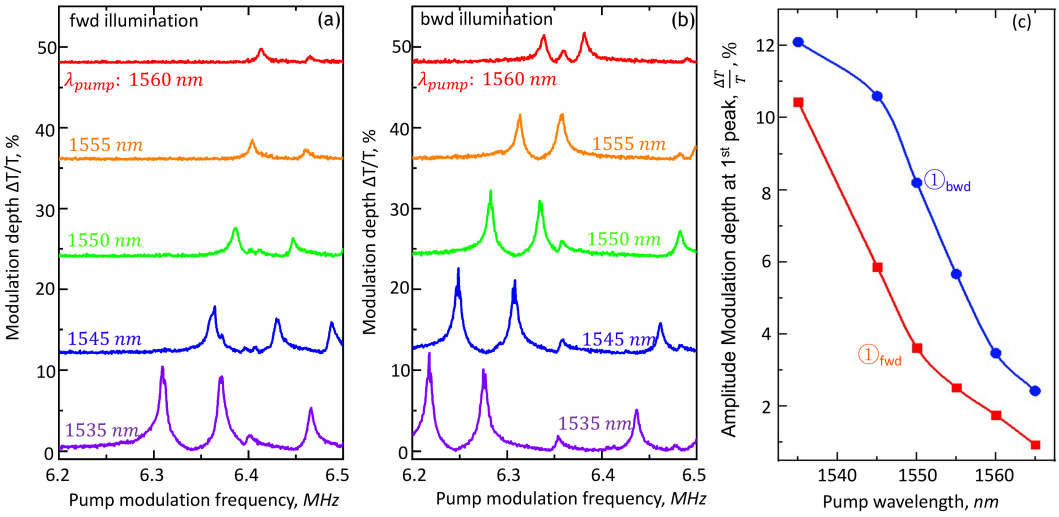

FIGURE 5.15: Modulation depth of transmitted probe light for different pump wavelengths at fixed pump power $P_{pump} = 58.8\mu W$. (a)(b)Modulation depth of transmitted probe light as a function of pump modulation frequency for a group of pump wavelength as labelled for forward (a) and backward (b) illumination. (c)The amplitude of modulation depth at the resonant peaks of beam type ① for forward and backward illumination as a function of pump wavelength.

low level when pump wavelength is moving away from resonant wavelength for the forward illumination. Also the absorption cross section (see Fig. 5.16(b)) drops in the mean time for this illumination direction. The collaboration of these two factors produce a rapid decrease of modulation depth with the increase of pump wavelength. The absorption is also decrease for the backward illumination, however, optical force for this illumination direction may increase a little bit and then decrease (see the blue curve in Fig. 5.16(c)), which gives a slow amplitude decrease rate at the beginning, shown as blue curve in Fig. 5.16(a), when pump laser wavelength is not far away from resonance.

Previously in Fig. 5.12(b) and Fig. 5.12(b)(d), one could see that the enhanced amplitude of ASD for beam type ① increase from 8.9 to 29.3 $\mu V/\sqrt{(Hz)}$ when the average pump power increase from 12.3 to 46.6 μW. However, this enhancement is determined both by average pump power and also relative spectral position between fixed pump frequencies and thermal peaks. To investigate the contribution from pure thermal effects on asymmetric transmission of nano-opto-mechanical metamaterials, I also conduct the pump-probe experiment with different probe power. Fig. 5.17 shows the evolution of spectra for forward (a) and backward (b) illumination directions. One could clearly see that the change of amplitude of modulation depth of beam type ① for both illumination directions increased with a similar trend. The modulation depth vary from 3.6 to 16.7 % for the backward illumination and that for forward illumination increase from 3.4 to 14.2 %. Fig. 5.17(c) gives amplitude

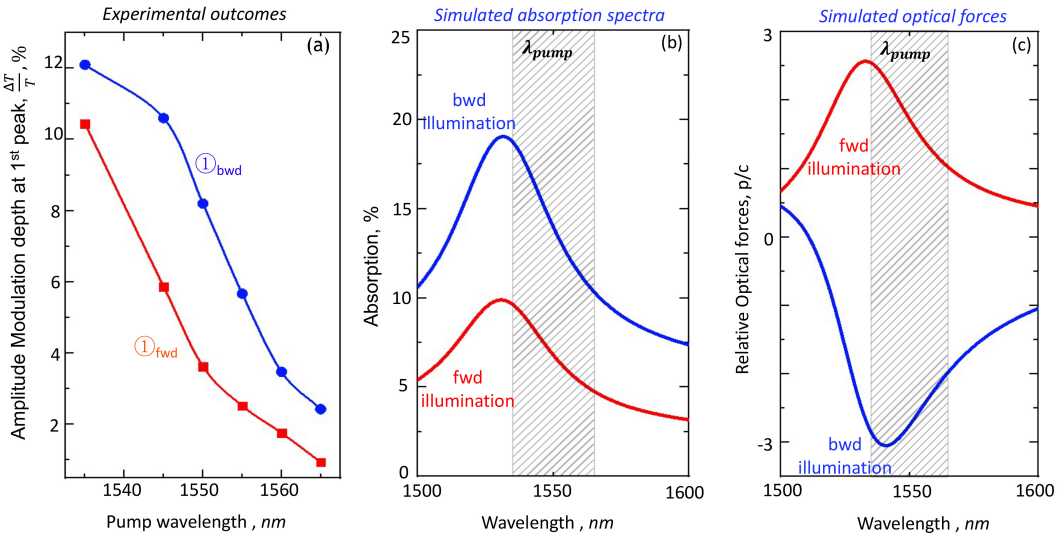

FIGURE 5.16: Qualitative analysis of the contribution from thermal and optical forces based upon simulated outcomes. (a)The amplitude of modulation depth at the resonant peaks of beam type ① for forward and backward illumination as a function of pump wavelength. (b) Simulated absorption spectra for forward and backward illumination, where the wavelength range of pump laser indicated by shadowed area. (c) Simulated optical forces dispersion for these two opposite illuminations and the shadowed area depict the pump laser range. All of these simulations based on the dimensional information of SEM image shown in Fig. 5.11(a).

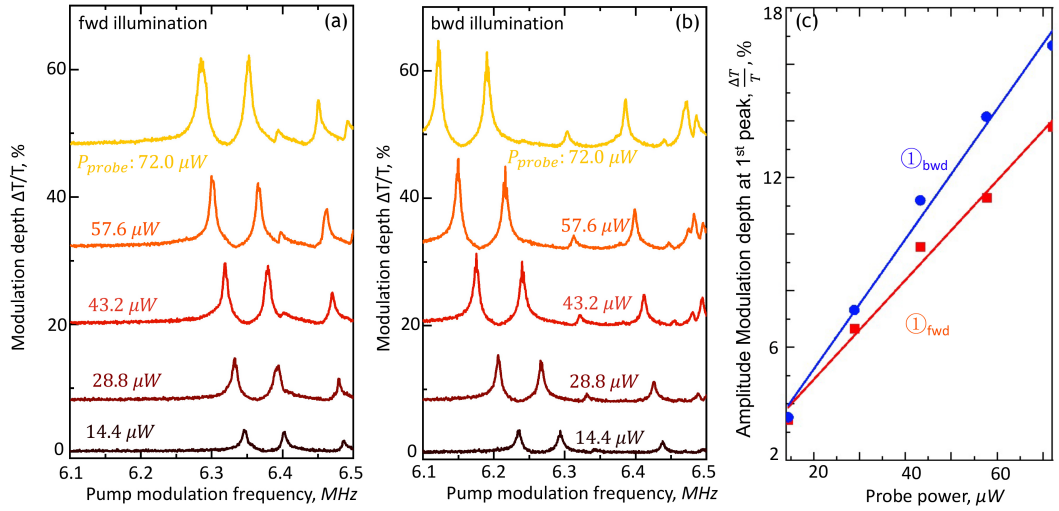

FIGURE 5.17: Modulation depth of transmitted probe light for different probe powers ranging from 14.4 μW to 72 μW at pump power P_{pump} =58.8 μW and wavelength λ_{pump} =1535 nm. (a)(b) Modulation depth of transmitted probe light as a function of pump modulation frequency for a group of probe power as labelled in the figure for forward (a) and backward (b) illumination. (c) Amplitude of modulation depth at the resonant peaks of beam type ① for forward and backward illumination as a function of probe power.

of modulation depth at eigenmode of beam type ① for forward and backward illumination as a function of probe power. And the data points in Fig. 5.17(c) can be nicely linear fitted, implying that the increase of modulation depth here originates from the contribution of temperature variation. It is noted that maximum asymmetry (around 16.3 %) on modulation depth of transmitted light can be observed at probe power of 72 μW, operating at around 6.1 MHz.

5.5 Conclusions

To summarize, we investigate the role of mechanical nonlinearity on transmission properties of nanomechanical metamaterials. Numerical modellings indicate that a forward-backward near-IR transmission difference of up to around 60% can be achieved at power of 24 mW with static displacement of beams in nanomechanical metamaterials. In the experimental aspect, it is found that resonant ponderomotive non-thermal optical forces can control the optical response of beams in nanomechanical metamaterial. Strong optical nonlinearity achieved via coupling of optical and mechanical resonances enables all-optical transmission modulation at μW power levels. Under opposing directions of illumination, the material and geometric asymmetry of the nanomechanical metamaterial changes the balance among thermal (absorption) and non-thermal (optical force) effects, giving rise to substantive directional asymmetry in its transmission properties. Specifically, transmission asymmetry of up to 16.3% can be observed at low pump power (58.8 μW) with operation frequency around 6.1 MHz.

Chapter 6

Optical magnetic response without metamaterials

In the course of numerically modelling optical forces in the nano-brick metamaterial and exploring the nature of optically resonances responsible for optical forces (see Section 5.3), I considered applying the methodology of multipole decomposition,which was introduced and extensively employed in work on toroidal metamaterials [80], [108], [109]. Furthermore, I took a step back from the complex high/low-index bilayer nanobrick/nanowire structures, to a simple single sub-wavelength thickness layer, because with this monolayer structure I could easily derive the analytical solution to verify the correction of numerically produced multipole decomposition outcomes in Section 5.3. Then, I proved that numerical and analytical results have an excellent agreement (see Fig. A.3). More importantly, I found that metamaterial structuring is not necessary to achieve optical magnetic response. Indeed, such a response is an essential characteristic of homogeneous dielectric thin films—Fabry–Pérot resonances, for example, depend on interference among electromagnetic multipoles including the magnetic dipole.

6.1 Introduction

The observation of a magnetic response at high (optical) frequencies was a fundamental step in electromagnetism, enabled by metamaterials—artificial media periodically structured on the subwavelength scale[110], [111]. This appeared to contradict the long-held idea that magnetization and permeability lose their meaning at high frequencies and that "optical magnetism" did not exist[112]. However, this (Landau–Lifshitz) argument does not hold in structured plasmonic metals and high refractive index dielectrics[113]. Historically, the rapid rise of the metamaterials research field was driven by opportunities arising through the realization of materials manifesting optical magnetism, which does not exist in nature. It is necessary for negative refraction and in turn for "superlenses"[5],certain forms of "cloaking"[114], and various beam-steering/wave-guiding applications. It is also of fundamental importance and increasing interest in the context of electromagnetic nonreciprocity and opto-magnetic devices[37], [115], [116].

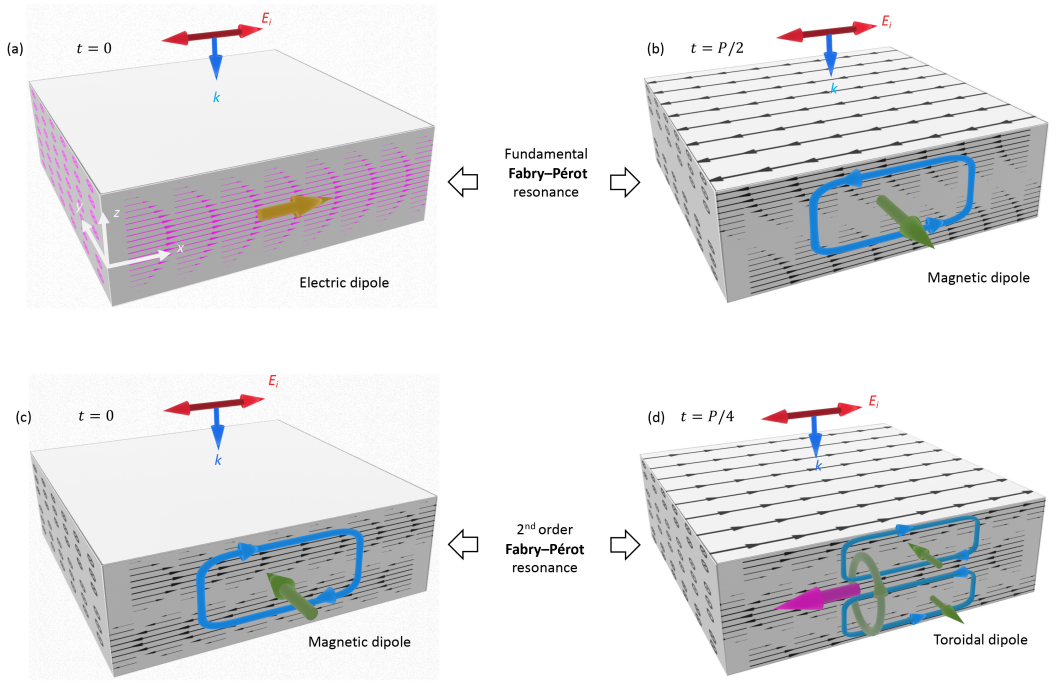

FIGURE 6.1: Electromagnetic multipoles induced in a thin dielectric film by a normally incident plane wave at the (a) and (b) fundamental and [(c) and (d)] second-order Fabry–Pérot resonance wavelengths at moments of time t separated by a half period (P/2) for the fundamental and a quarter-period (P/4) for the second-order resonance. Magenta arrows in (a) relate to the electric displacement field amplitude and direction; black arrows in (b)–(d) to the displacement current. Overlaid 3D arrows schematically show the significant multipoles in each case: electric, magnetic, and toroidal dipoles in gold, green, and purple; displacement and poloidal current loops in blue and green, respectively.

6.2 Results and discussion

In metamaterials comprising metallic split-ring metamolecules, the optical magnetic response is typically underpinned by oscillating conduction current loops induced by the electric component of the incident light field[110], [111], [117]. In dielectric metamaterials or individual nanoparticles, it is associated with loops of displacement current induced in the nanostructured dielectric, again by the incident electric field[118]–[120].We show here that an optical magnetic response is in fact a characteristic feature of homogeneous, unstructured dielectric layers of sub-wavelength thickness. Well-known thin film properties, such as Fabry–Pérot (FP) interference resonances, cannot be explained without the magnetic contribution. The vanishing of reflectivity at the fundamental FP resonance is a consequence of destructive interference among electric dipole (ED), magnetic dipole, and electric quadrupole (EQ) contributions. The second order FP resonance is associated with higher order multipoles: the electric octupole (EO), magnetic quadrupole (MQ), and toroidal dipole (TD) exhibit resonances at this point, while the electric dipole vanishes.

The multipolar nature of the optical response of a dielectric layer is a universal feature of thin films, and it is most pronounced in high refractive index media. Here,

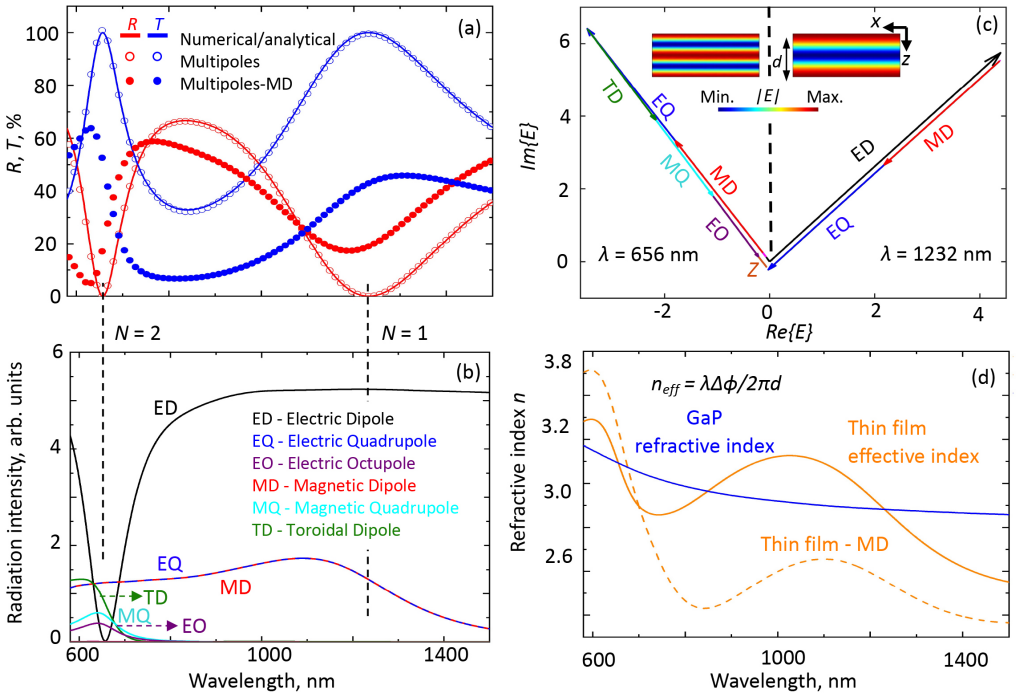

FIGURE 6.2: (a) Spectral dependence of transmission (T, blue) and reflection (R, red) of a 200 nm GaP film in vacuum at normal incidence. Solid lines are identically obtained by numerically solving Maxwell's equations or analytically. Hollow circles are derived from multipole scattering reconstructions. Solid circles are the same but excluding the magnetic dipole contribution. (b) Spectral dependence of light intensity radiated in the reflection direction by the six leading multipoles. (c) Vector plot of complex electric field multipole components at the 656 and 1232 nm FP resonant wavelengths. The insets show corresponding cross-sectional electric field distributions. (d) Dispersion of the GaP film's effective index ($\Delta\phi$ = phase delay in transmission) and GaP's bulk refractive index. The dashed line shows the film's effective index without accounting for the magnetic dipole contribution.

I numerically solve Maxwell's equations for light propagation through the layer (using COMSOL MultiPhysics) and evaluate the displacement currents induced by the incident wave, see Figs. 6.1(a) - (d). From there, I compute the different multipole contributions to light scattering , see Fig. 6.2(b), using the standard methodology employed in metamaterials research[80]. The accuracy of the multipole decomposition is verified by comparing reflection and transmission spectra calculated as the sum of the contribution from multipoles. Here, inclusion of multipole terms up to the magnetic octupole[121] is sufficient to describe the macroscopic optical properties of the film with accuracy better than 1 %. Our analysis shows that the optical properties of a subwavelength thickness dielectric layer are not solely of electric dipolar nature but formed by a combination of multipole excitations (shown in Fig. 6.2(b)). Indeed, under certain resonant conditions, the electric dipolar response vanishes. The magnetic dipolar contribution is prominent at all wavelengths (resonant or otherwise), and its omission leads to significant errors (exceeding 50%) in the reconstruction of reflection and transmission spectra of the layer, as illustrated in Fig. 6.2(a).

FP resonances are observed when the optical thickness of a layer is equal to an

integer number N of standing wave periods: $N\lambda/2 = n(\lambda)d$, where d is the physical thickness of the layer and $n(\lambda)$ is its wavelength-dependent refractive index. Here, I consider a 200 nm thick GaP layer that presents FP resonances in the visible to near-IR spectral range, at 1232 nm (N = 1) and 656 nm (N = 2), where transmissivity approaches unity and reflectivity vanishes [Fig. 6.2(a)].

At the fundamental (N = 1) resonance, the response is dominated by electric dipole (ED) scattering, with magnetic dipole (MD) and electric quadrupole (EQ) contributions (Fig. 6.2(b)). The induced ED arises from strong in-phase displacement fields $\vec{D} = \epsilon\vec{E}$, where ϵ is the dielectric permittivity and $\vec{E}$ is the electric field inside the dielectric. $\vec{D}$ and $\vec{E}$ are unidirectionally oriented across the film thickness [magenta arrows in Fig. 1(a)]. The induced MD emerges from oppositely directed displacement currents $\vec{J_D} = i\omega\epsilon_0(\epsilon-1)\vec{E}$ (black arrows in Fig. 6.1(b)) at the top/bottom of the layer, forming a magnetic moment current loop in the xz plane. The ED oscillates with a half period (P/2) phase difference from the MD/EQ, whereby their radiated fields interfere destructively. This is further illustrated in Fig. 6.2(c), which presents the real and imaginary parts of the multipolar fields scattered (reflected) in the backward ($+z$) direction. The MD and EQ contributions are each equal to around half that of the ED but oscillate in antiphase with the latter.

At the second ($N = 2$) FP resonance, ED emission vanishes but, alongside the MD and EQ, I observe contributions from higher multipoles including the electric octupole(EO), magnetic quadrupole(MQ), and toroidal dipole(TD), see Fig. 6.2(b). The induced MD again emerges from opposing displacement currents (black arrows in Fig. 6.1(c)) at the top/bottom of the layer, forming a magnetic moment current loop in the yz plane. Fields radiated by the TD exhibit a quarter cycle ($P/4$) phase difference with respect to the TD moment and are thus in antiphase with the MD. The MD and EQ emission components are again (as at $N = 1$) in-phase and of comparable amplitude, now being the two largest components. Reflectance is cancelled by their destructive interference with fields radiated by the EO, MQ and TD, as illustrated in Fig. 6.2(c) (here, the vector Z represent the collective contribution of still higher order terms).

In addition to numerical approach, multipole decomposition can also be analytically conducted. The six leading multipole moments can be expressed as(derivation details can be found in Appendix A:

ED moment p:

$$p = \frac{\epsilon_0(\epsilon-1)\Delta E_0 d^2}{ik}[(1+n)e^{i2kd} - 2e^{ikd} + (1-n)] \tag{6.1}$$

MD moment m:

$$\begin{aligned} m = \frac{\omega\epsilon_0(\epsilon-1)\Delta E_0 d^2}{4ck^2}&[-(2i+kd)(1+n)e^{i2kd} \\ &+ (i4n-2kd)e^{ikd} + (2i-kd)(1-n)] \end{aligned} \tag{6.2}$$

TD moment T:

$$T = \frac{i\omega\epsilon_0(\epsilon-1)\Delta E_0}{10c}\left\{-\frac{3d^4}{i4k}[(1+n)e^{i2kd}-2e^{ikd}+(1-n)]\right.$$
$$\left.+\frac{2d^2}{k^3}[-(i2+kd)(1+n)e^{i2kd}+(i4-2kdn)e^{ikd}-(1-n)(i2-kd)]\right\} \tag{6.3}$$

EQ moment $Q^{(e)}$:

$$Q^{(e)} = \frac{\epsilon_0(\epsilon-1)\Delta E_0 d^2}{i4k^2}[-(2i+kd)(1+n)e^{i2kd}$$
$$+(i4n-2kd)e^{ikd}+(2i-kd)(1-n)] \tag{6.4}$$

MQ moment $Q^{(m)}$:

$$Q^{(m)} = \frac{i\omega\epsilon_0(\epsilon-1)\Delta E_0}{3c}\left\{\frac{d^4}{i6k}\big[(1+n)e^{i2kd}-2e^{ikd}+(1-n)\big]\right.$$
$$\left.-\frac{d^2}{k^3}\big[-(i2+kd)(1+n)e^{i2kd}+(i4-2kdn)e^{ikd}-(1-n)(i2-kd)\big]\right\} \tag{6.5}$$

EO moment $O^{(e)}$:

$$O^{(e)} = \frac{\epsilon_0(\epsilon-1)\Delta E_0}{6}\left\{\frac{2d^4}{i15k}\big[(1+n)e^{i2kd}-2e^{ikd}+(1-n)\big]\right.$$
$$\left.-\frac{4d^2}{5k^3}\big[-(i2+kd)(1+n)e^{i2kd}+(i4-2kdn)e^{ikd}-(1-n)(i2-kd)\big]\right\} \tag{6.6}$$

where k is the wave number, E_0 is the amplitude of incident light, ω is the angular frequency, ϵ_0 and ϵ is permittivity of free-space and relative permittivity of GaP. By substituting these six multipole moments (eq.6.1 - eq.6.6) into eq. A.44, one could get multipole contributions to far-field light intensity radiated in the reflection direction like Fig. 6.2(c). I then compared numerical and analytical solution in Fig. A.3, found that they are in a very good agreement.

Fig. 6.2(d) shows the dispersion of the GaP film's effective refractive index, defined as $n_{eff} = \lambda\Delta\phi/2\pi d$, where $\Delta\phi$ is the phase delay in transmission. By virtue of interference between the electric and magnetic responses, this can be higher or lower than the material's volume refractive index. Here again, as for the reflectivity and transmission spectra in Fig. 6.2(a), the essential role of the magnetic component of optical response is clearly illustrated by the fact that omission of the MD from the multipolar reconstruction leads to significant errors in the value and dispersion of the thin film effective index. The effective enhancement/suppression of the index through multipolar interference in the present case resembles the mechanism whereby a negative refractive index is achieved in metamaterials via the simultaneous presence of (engineered) electric and magnetic responses. The regime of suppressed reflectivity may also be compared with the of (i) optical anapole metamaterials[122], [123], in which it derives from interference between electric and toroidal dipoles,

and (ii) Huygens metasurfaces, wherein it arises through interference of electric and magnetic responses[88], [124]. In thin unstructured dielectric layers, reflectivity suppression is achieved without lateral (metamaterials) structuring, while, nonetheless, being related to multipolar interference. We also note that the magnetic and generally multipolar nature of a dielectric film's response has much in common with the enhanced magnetic response observed in thin ($< \lambda$) films in a standing wave[125].

6.3 Conclusions

In conclusion, I would emphatically agree with Monticone with Alù[6]that "artificial optical magnetism ... represents a quintessential example of how new fundamental material properties, previously thought to be strictly unavailable, can truly be realized by engineered arrangement of elements at nanoscale," and have shown here that it can be achieved by simple confinement of a material in a sub-wavelength layer. The complex structure of multipole fields in a thin layer of dielectric can be exploited for coupling of electromagnetic radiation to matter through the excitation of high-order multipolar atomic transitions in constituent atoms, and for the exploitation of magnetic dipole transitions at optical frequencies, for instance, in rare earths as laser gain media[126] and quantum qubit applications[127].

Chapter 7

Conclusion

7.1 Summary

The combination of nanomechanics and metamaterials via thermal and optical forces represents a brand new approach to accessing novel optical properties and realizing remarkable functionalities. High-contrast directionally asymmetric transmission is a particularly interesting example both from the perspective of fundamental physics and potential applications. In this thesis, I developed reconfigurable metamaterials possess nanoscale metamolecules and pico-metres movement features offering a platform to investigate thermal behaviours of metamaterials and achieve transmission asymmetry.

The key achievements in this thesis include:

- The construction of a dedicated setup for investigation of thermal fluctuations and directional asymmetry of optical properties in nanomechanical metamaterials (Chapter 2)
- The development of sophisticated full EBL protocol to manufacture nanomechanical metamaterials with good geometry uniformity and high Q-factor resonances (Chapter 2)
- The first observation of thermal fluctuation of the optical properties of nanomechanical metamaterials. At room temperature the magnitude of metamaterial transmission and reflection fluctuations is broadly on the scale of $0.1 - 1\%$ at optical resonances, building a foundation for optimization the performance of nanomechanical metamaterials (Chapter 3).
- The first presentation on optical control of nanomechanical eigenfrequencies and Brownian motion in metamaterials. Specifically, eigenfrequencies of beams shift up to 3.6% and RMS displacement vary up to 4.3% with light intensity of $0.8\mu W/\mu m^2$, setting a basis for bolometric, mass and stress sensing applications. (Chapter 4).
- The first demonstration of asymmetric transmission in nanomechanical metamaterials, in which resonant excitation of optical and mechanical sub-systems create profound light-induced transmission asymmetry reaching 16% at μW power levels with operation frequency at around 6MHz. This makes it suitable for a range of laser technology and fibre telecom applications (Chapter 5).

- The first finding that a free-standing dielectric thin film is able to exhibit optical magnetic response. Fabry–Pérot resonances are formed by the interference of electromagnetic multipoles, including the magnetic dipole(Chapter 6).

7.2 Outlook

There is still plenty of room to improve in the experiment shown in this thesis as the experiments are mainly "proof-of-principle" demonstrated. Four main directions deserved to be explored in the future are listed as following:

- The EBL protocol I developed could potentially enable Ga^+ contamination-free samples with higher Q and it is a scalable manufacturing process. It is worthy to spend more time in the future to optimize it. The lift-off step, which play a key role in manufacturing desired high-quality sample, could be further improved by depositing thinner hardmask materials to avoid the connections built up by Si residuals between neighbouring beams in the following steps.

- For the asymmetric transmission part, it could possible to achieve even higher transmission asymmetry operating in a faster speed if the nanomechanical metamaterial sample fabricated by EBL process with high Q factor and good mechanical properties.

- For the thermal fluctuation part, currently the phenomena we observed is in the linear regime. It could be possible to explore nonlinear response of nanomechanical metamaterials driven by thermal forces.

- All of the mechanical modes studied in this thesis are fundamental out-of-plane modes, the in-plane motion between neighbouring beams could potentially deserved to be utilized to explore reconfigurable EIT effects.

Appendix A

Analytical solutions for multipole decomposition of dielectric slab

In this appendix, a step by step derivation of an analytical expression for multipole decomposition of dielectric slab is presented

A.1 Electric distribution inside dielectric film

Assuming that the incident light is propagating along positive direction of z axis with x-polarization, i.e. $\vec{E}(z) = \hat{x}E_0e^{-ik_0z}$, where $k_0 = \omega/c$ and ω is angular frequency in free space and E_0 is the incident field amplitude. The wave normally illuminate on a thin dielectric film, here we were using gallium phosphide (GaP) as an example, with thickness of d and refractive index n. Fig. A.1 (a) shows relevant layout, in which the coordinate origin is set in the centre of the film, and there are two interfaces ($A\&B$) between dielectric and air. If we denote by E_2, the amplitude of electric field of the wave travelling in the direction of incident light ($+z$ direction) at interface A and by E_3, that of the negative-going wave at the same interface, the electric field inside of dielectric film can be written as the superposition of these two travelling waves with wave number $k = nk_0$:

$$E_d(z) = E_2e^{-ik(z+d/2)} + E_3e^{ik(z+d/2)} \tag{A.1}$$

Furthermore, we denote reflected electric amplitude E_1 and transmitted electric field E_6, the positive and negative going wave amplitude in the interface B as E_4 and E_5. According to interface conditions for electromagnetic fields,
At interface A:

$$E_0 + E_1 = E_2 + E_3 \tag{A.2}$$

$$E_0 - E_1 = n(E_2 - E_3) \tag{A.3}$$

At interface B:

$$E_4 + E_5 = E_6 \tag{A.4}$$

$$n(E_4 - E_5) = E_6 \tag{A.5}$$

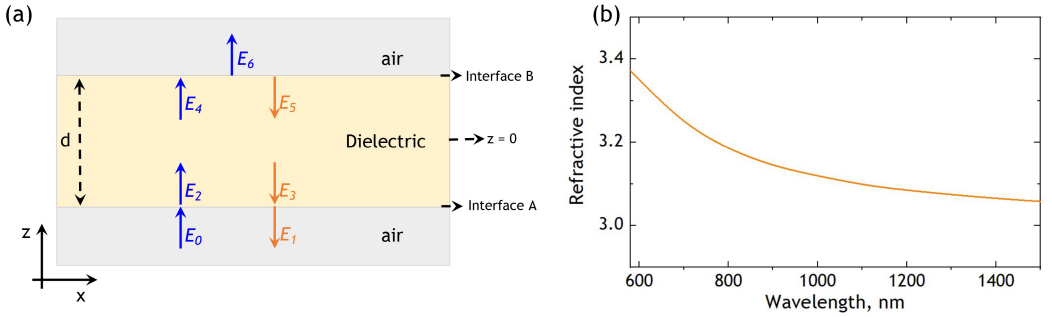

FIGURE A.1: Basic information of investigated dielectric thin film (a)Sketch of layout indicating relevant parameters. E_0 : incident electric field; E_α : reflected and transmitted electric field($\alpha : 1 \rightarrow 6$); d: thickness of dielectric film. The coordinate origin is selected in the centre of film and incident light is sent along $+z$ direction with x - polarization. (b) Refractive index dispersion of dielectric film(GaP).

Also,

$$E_4 = E_2 e^{-ikd} \tag{A.6}$$

$$E_5 = E_3 e^{ikd} \tag{A.7}$$

The electric field at the interface A can be solved through equation (2)-(7) as

$$E_2 = (n+1)e^{i2kd}\Delta E_0 \tag{A.8}$$

$$E_3 = (n-1)\Delta E_0 \tag{A.9}$$

where Δ can be expressed as

$$\Delta = \frac{2}{(1+n)^2 e^{i2kd} - (1-n)^2} \tag{A.10}$$

By substituting eq.A.8 and A.9 into eq.A.1, the electric field inside dielectric film $E_d(z)$ then can be written as

$$E_d(z) = (n+1)e^{i2kd}\Delta e^{-ik(z+d/2)}E_0 + (n-1)\Delta e^{ik(z+d/2)}E_0 \tag{A.11}$$

if we denote

$$V(z) = (n+1)e^{i2kd}e^{-ik(z+d/2)} + (n-1)e^{ik(z+d/2)} \tag{A.12}$$

$E_d(z)$ can be simplified as

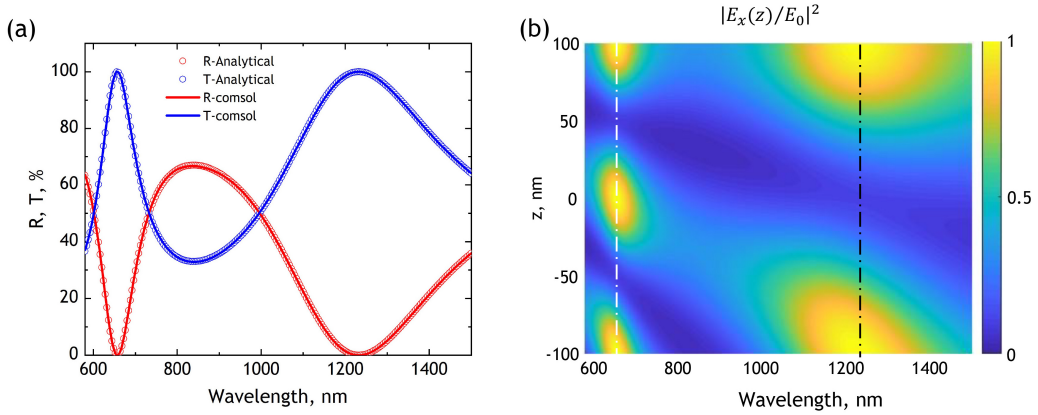

FIGURE A.2: Optical properties of dielectric films. (a) Reflection and transmission spectrum from COMSOL calculations and analytical solutions. (b) Normalized electric intensity distribution along z direction at different wavelength, black and white dashed lines depict the first and second Fabry-Pèrot resonance (data from analytical solutions).

$$E_d(z) = \Delta V(z) E_0 \tag{A.13}$$

from which the reflectance from dielectric film can be written as

$$\begin{aligned} \mathbf{R} &= \left|\frac{E_1}{E_0}\right|^2 = \left|\frac{E_2 + E_3 - E_0}{E_0}\right|^2 \\ &= \left|(n+1)e^{i2kd}\Delta + (n-1)\Delta - 1\right|^2 \end{aligned} \tag{A.14}$$

and transmittance can be expressed as

$$\begin{aligned} \mathbf{T} &= \left|\frac{E_6}{E_0}\right|^2 = \left|\frac{E_4 + E_5}{E_0}\right|^2 = \left|\frac{E_2 e^{-ikd} + E_3 e^{ikd}}{E_0}\right|^2 \\ &= \left|(n+1)e^{i2kd}\Delta e^{-ikd} + (n-1)\Delta e^{ikd}\right|^2 = 4\left|ne^{ikd}\Delta\right|^2 \end{aligned} \tag{A.15}$$

By applying the refractive index dispersion (see Fig. A.1(b)) of GaP into eq.A.14 and eq.A.15, the reflection and transmission spectrum can be found in Fig. A.2(a), where they match the simulated reflectance and transmittance very well. Also, based on eq.A.13, the normalized electric field intensity distribution $|E_d(z)/E_0|^2$ are drawn in Fig. A.2(b), in which first and second Fabry-Pèrot resonances can be observed.

A.2 Multipole decomposition for dielectric thin film

We can now define displacement current as: $\vec{J} = i\omega\epsilon 0(\epsilon - 1)\vec{E}_d$. As incident light is x - polarized, only $J_x(z)$ is non-vanishing. We have obtained the electric field distribution ($E_d(z)$) in eq.A.13, the x-component of displacement current $J_x(z)$ can

therefore be written as:

$$J_x(z) = i\omega\epsilon_0(\epsilon-1)E_d(z) = i\omega\epsilon 0(\epsilon-1)\Delta V(z)E_0 \tag{A.16}$$

As multipole moment need to be calculated in a volume, here we are using a GaP cubic with side length of d to drive multipole moment, and the coordinate center is still set in the centre of this cubic. Here, we derived the analytical expression of ED, MD, TD, EQ, MQ and EO.

A.2.1 Electric Dipole (ED)

The Electric dipole component p_α can be expressed as following:

$$p_\alpha = \frac{1}{i\omega}\int \mathrm{d}^3 r J_\alpha \tag{A.17}$$

As $Jy = Jz = 0$, only x-component of electric dipole p_x is non-vanishing, it can be written as

$$\begin{aligned} p_x = \frac{1}{i\omega}\int_{-\frac{d}{2}}^{\frac{d}{2}} J_x(z)\mathrm{d}z \int_{-\frac{d}{2}}^{\frac{d}{2}} \mathrm{d}x \int_{-\frac{d}{2}}^{\frac{d}{2}} \mathrm{d}y &= \frac{d^2}{i\omega}\int_{-\frac{d}{2}}^{\frac{d}{2}} i\omega\epsilon_0(\epsilon-1)\Delta V(z)E_0\mathrm{d}z \\ &= \epsilon_0(\epsilon-1)\Delta E_0 d^2 \int_{-\frac{d}{2}}^{\frac{d}{2}} V(z)\mathrm{d}z \end{aligned} \tag{A.18}$$

As integration $\int_{-\frac{d}{2}}^{\frac{d}{2}} V(z)\mathrm{d}z$ will be frequently reused in the following derivations, so this integration is written separately in following equation:

$$\begin{aligned} \int_{-\frac{d}{2}}^{\frac{d}{2}} V(z)\mathrm{d}z &= \int_{-\frac{d}{2}}^{\frac{d}{2}} [(n+1)e^{i2kd}e^{-ik(z+d/2)} + (n-1)e^{ik(z+d/2)}]\mathrm{d}z \\ &= \frac{1}{ik}[-(1+n)e^{i2kd}e^{-ik(z+d/2)} + (n-1)e^{ik(z+d/2)}] \,|_{-\frac{d}{2}}^{\frac{d}{2}} \\ &= \frac{(1+n)e^{i2kd} - 2e^{ikd} + (1-n)}{ik} \end{aligned} \tag{A.19}$$

By substituting eq.A.19 into eq.A.18, ED moment can be written as

$$p_x = \frac{\epsilon_0(\epsilon-1)\Delta E_0 d^2}{ik}[(1+n)e^{i2kd} - 2e^{ikd} + (1-n)] \tag{A.20}$$

A.2.2 Magnetic Dipole (MD)

The Magnetic dipole component m_α can be expressed as following:

$$m_\alpha = \frac{1}{2c}\int \mathrm{d}^3 r[\mathbf{r}\times\mathbf{J}]_\alpha r^2 \tag{A.21}$$

Only the y-component of the magnetic dipole m_y is non-vanishing.

$$\begin{aligned} m_y = \frac{1}{2c}\int_{-\frac{d}{2}}^{\frac{d}{2}} zJ_x(z)\mathrm{d}z \int_{-\frac{d}{2}}^{\frac{d}{2}} \mathrm{d}x \int_{-\frac{d}{2}}^{\frac{d}{2}} \mathrm{d}y &= \frac{d^2}{2c}\int_{-\frac{d}{2}}^{\frac{d}{2}} iz\omega\epsilon 0(\epsilon-1)\Delta V(z)E_0\mathrm{d}z \\ &= \frac{i\omega\epsilon_0(\epsilon-1)\Delta E_0 d^2}{2c}\int_{-\frac{d}{2}}^{\frac{d}{2}} zV(z)\mathrm{d}z \end{aligned} \tag{A.22}$$

Integration $\int_{-\frac{d}{2}}^{\frac{d}{2}} zV(z)\mathrm{d}z$ can be calculated as following:

$$\begin{aligned} \int_{-\frac{d}{2}}^{\frac{d}{2}} zV(z)\mathrm{d}z &= \int_{-\frac{d}{2}}^{\frac{d}{2}} z[(n+1)e^{i2kd}e^{-ik(z+d/2)} + (n-1)e^{ik(z+d/2)}]\mathrm{d}z \\ &= \int_{-\frac{d}{2}}^{\frac{d}{2}} z(n+1)e^{i2kd}e^{-ik(z+d/2)}\mathrm{d}z + \int_{-\frac{d}{2}}^{\frac{d}{2}} z(n-1)e^{ik(z+d/2)}\mathrm{d}z \\ &= (n+1)e^{i2kd}\int_{-\frac{d}{2}}^{\frac{d}{2}} (z+\frac{d}{2}-\frac{d}{2})e^{-ik(z+d/2)}\mathrm{d}(z+\frac{d}{2}) \\ &+ (n-1)\int_{-\frac{d}{2}}^{\frac{d}{2}} (z+\frac{d}{2}-\frac{d}{2})e^{-ik(z+d/2)}\mathrm{d}(z+\frac{d}{2}) \\ &= (n+1)e^{i2kd}\left\{\frac{1}{(-ik)^2}[-ik(z+\frac{d}{2})-1] + \frac{d}{i2k}\right\}e^{-ik(z+\frac{d}{2})}\,|_{-\frac{d}{2}}^{\frac{d}{2}} \\ &+ (n-1)\left\{\frac{1}{(ik)^2}[ik(z+\frac{d}{2})-1] - \frac{d}{i2k}\right\}e^{ik(z+\frac{d}{2})}\,|_{-\frac{d}{2}}^{\frac{d}{2}} \\ &= \frac{1}{i2k^2}[-(2i+kd)(1+n)e^{i2kd} + (i4n-2kd)e^{ikd} + (2i-kd)(1-n)] \end{aligned} \tag{A.23}$$

By substituting eq.A.23 into eq.A.22, MD moment can be written as:

$$\begin{aligned} m_y &= \frac{i\omega\epsilon_0(\epsilon-1)\Delta E_0 d^2}{2c}\frac{1}{i2k^2}[-(2i+kd)(1+n)e^{i2kd} + (i4n-2kd)e^{ikd} + (2i-kd)(1-n)] \\ &= \frac{\omega\epsilon_0(\epsilon-1)\Delta E_0 d^2}{4ck^2}[-(2i+kd)(1+n)e^{i2kd} + (i4n-2kd)e^{ikd} + (2i-kd)(1-n)] \end{aligned} \tag{A.24}$$

A.2.3 Toroidal Dipole (TD)

The toroidal dipole component T_α can be expressed as following:

$$T_\alpha = \frac{1}{10c}\int \mathrm{d}^3 r[\mathbf{r}\cdot\mathbf{J}r_\alpha - 2r^2 J_\alpha] \tag{A.25}$$

Only the x-component of toroidal dipole T_x is non-vanishing becasue $Jy = Jz = 0$ and T_x is given by

$$\begin{aligned} T_x &= \frac{1}{10c}\int_{-\frac{d}{2}}^{\frac{d}{2}}\int_{-\frac{d}{2}}^{\frac{d}{2}}\int_{-\frac{d}{2}}^{\frac{d}{2}} x^2 J_x(z) - 2(x^2+y^2+z^2)J_x(z)\mathrm{d}x\mathrm{d}y\mathrm{d}z \\ &= \frac{i\omega\epsilon_0(\epsilon-1)\Delta E_0}{10c}\int_{-\frac{d}{2}}^{\frac{d}{2}}\int_{-\frac{d}{2}}^{\frac{d}{2}}\int_{-\frac{d}{2}}^{\frac{d}{2}}(-x^2-2y^2-2z^2)V(z)\mathrm{d}x\mathrm{d}y\mathrm{d}z \end{aligned} \tag{A.26}$$

for the convenience of integration, eq.A.26 can be separated into 3 parts showing as following:

$$part1: \int_{-\frac{d}{2}}^{\frac{d}{2}} -x^2\mathrm{d}x\int_{-\frac{d}{2}}^{\frac{d}{2}}\mathrm{d}y\int_{-\frac{d}{2}}^{\frac{d}{2}} V(z)\mathrm{d}z \tag{A.27a}$$

$$part2: \int_{-\frac{d}{2}}^{\frac{d}{2}}\mathrm{d}x\int_{-\frac{d}{2}}^{\frac{d}{2}} -2y^2\mathrm{d}y\int_{-\frac{d}{2}}^{\frac{d}{2}} V(z)\mathrm{d}z \tag{A.27b}$$

$$part3: \int_{-\frac{d}{2}}^{\frac{d}{2}}\mathrm{d}x\int_{-\frac{d}{2}}^{\frac{d}{2}}\mathrm{d}y\int_{-\frac{d}{2}}^{\frac{d}{2}} -2z^2V(z)\mathrm{d}z \tag{A.27c}$$

part 1 and part2 are easy to be solved as we hav already known the integration of $\int_{-\frac{d}{2}}^{\frac{d}{2}} V(z)\mathrm{d}z$ in eq.A.19. Part1 can be written as:

$$\begin{aligned} \int_{-\frac{d}{2}}^{\frac{d}{2}} -x^2\mathrm{d}x\int_{-\frac{d}{2}}^{\frac{d}{2}}\mathrm{d}y\int_{-\frac{d}{2}}^{\frac{d}{2}} V(z)\mathrm{d}z &= \frac{-d}{3}x^3\Big|_{-\frac{d}{2}}^{\frac{d}{2}}\int_{-\frac{d}{2}}^{\frac{d}{2}} V(z)\mathrm{d}z \\ &= -\frac{d^4}{i12k}[(1+n)e^{i2kd} - 2e^{ikd} + (1-n)] \end{aligned} \tag{A.28}$$

Part2 can be written as:

$$\begin{aligned} \int_{-\frac{d}{2}}^{\frac{d}{2}}\mathrm{d}x\int_{-\frac{d}{2}}^{\frac{d}{2}} -2y^2\mathrm{d}y\int_{-\frac{d}{2}}^{\frac{d}{2}} V(z)\mathrm{d}z &= \frac{-2d}{3}y^3\Big|_{-\frac{d}{2}}^{\frac{d}{2}}\int_{-\frac{d}{2}}^{\frac{d}{2}} V(z)\mathrm{d}z \\ &= -\frac{d^4}{i6k}[(1+n)e^{i2kd} - 2e^{ikd} + (1-n)] \end{aligned} \tag{A.29}$$

Part3 is given as:

$$\begin{aligned}
&\int_{-\frac{d}{2}}^{\frac{d}{2}} \mathrm{d}x \int_{-\frac{d}{2}}^{\frac{d}{2}} \mathrm{d}y \int_{-\frac{d}{2}}^{\frac{d}{2}} -2z^2 V(z)\mathrm{d}z = 2d^2 \int_{-\frac{d}{2}}^{\frac{d}{2}} -z^2 V(z)\mathrm{d}z \\
&= 2d^2\big[z^2 \int_{-\frac{d}{2}}^{\frac{d}{2}} V(z)\mathrm{d}z + \int_{-\frac{d}{2}}^{\frac{d}{2}} 2z(\int V(z)\mathrm{d}z)\mathrm{d}z\big] \\
&= 2d^2[-z^2 \frac{-(1+n)e^{i2kd}e^{-ik(z+d/2)} + (n-1)e^{ik(z+d/2)}}{ik}]\Big|_{-\frac{d}{2}}^{\frac{d}{2}} \\
&+ 2d^2 \int_{-\frac{d}{2}}^{\frac{d}{2}} 2z(\int V(z)\mathrm{d}z)\mathrm{d}z \\
&= -\frac{d^4}{i2k}[(1+n)e^{i2kd} - 2e^{ikd} + (1-n)] + 2d^2 \int_{-\frac{d}{2}}^{\frac{d}{2}} 2z(\int V(z)\mathrm{d}z)\mathrm{d}z \qquad \text{(A.30)}
\end{aligned}$$

Here we isolate the last term in eq.A.30, e.g. $2d^2 \int_{-\frac{d}{2}}^{\frac{d}{2}} 2z(\int V(z)\mathrm{d}z)\mathrm{d}z$, and solve it separately.

$$\begin{aligned}
&2d^2 \int_{-\frac{d}{2}}^{\frac{d}{2}} 2z(\int V(z)\mathrm{d}z)\mathrm{d}z = \frac{4d^2}{ik} \int_{-\frac{d}{2}}^{\frac{d}{2}} z[-(1+n)e^{i2kd}e^{-ik(z+d/2)} + (n-1)e^{ik(z+d/2)}]\mathrm{d}z \\
&= \frac{2d^2}{k^3}\big[-(i2+kd)(1+n)e^{i2kd} + (i4-2kdn)e^{ikd} - (1-n)(i2-kd)\big] \qquad \text{(A.31)}
\end{aligned}$$

by substituting eq.A.28 - eq.A.31 into eq. A.26, the expression of T_x is

$$\begin{aligned}
T_x =& \frac{i\omega\epsilon_0(\epsilon-1)\Delta E_0}{10c}\Big\{-\frac{3d^4}{i4k}[(1+n)e^{i2kd} - 2e^{ikd} + (1-n)] \\
&+\frac{2d^2}{k^3}[-(i2+kd)(1+n)e^{i2kd} + (i4-2kdn)e^{ikd} - (1-n)(i2-kd)]\Big\} \qquad \text{(A.32)}
\end{aligned}$$

A.2.4 Electric Quadrupole (EQ)

The electric quadrupole component $Q_{\alpha\beta}^{(e)}$ can be expressed as following:

$$Q_{\alpha\beta}^{(e)} = \frac{1}{i2\omega}\int \mathrm{d}^3 r \left[r_\alpha J_\beta + r_\beta J_\alpha - \frac{2}{3}\delta_{\alpha\beta}(\mathbf{r}\cdot\mathbf{J})\right] \qquad \text{(A.33)}$$

Considering the condition $Jy = Jz = 0$ and also the symmetric interval $[-\frac{d}{2}, \frac{d}{2}]$,only $Q_{xz}^{(e)}$ and $Q_{zx}^{(e)}$ is non-vanishing, the value of these two terms is equal to each other, and it can be give by:

$$Q_{zx}^{(e)} = Q_{xz}^{(e)} = \frac{1}{i2\omega}\int_{-\frac{d}{2}}^{\frac{d}{2}}\mathrm{d}x\int_{-\frac{d}{2}}^{\frac{d}{2}}\mathrm{d}y\int_{-\frac{d}{2}}^{\frac{d}{2}} zJ_x(z)\mathrm{d}z$$
$$= \frac{\epsilon_0(\epsilon-1)\Delta E_0 d^2}{2}\int_{-\frac{d}{2}}^{\frac{d}{2}} zV(z)\mathrm{d}z \tag{A.34}$$

the solutions of last term in eq.A.34 $\int_{-\frac{d}{2}}^{\frac{d}{2}} zV(z)\mathrm{d}z$ can be found in eq. A.23, therefore, these $Q_{xz}^{(e)}$ can be written as

$$Q_{zx}^{(e)} = Q_{xz}^{(e)} = \frac{\epsilon_0(\epsilon-1)\Delta E_0 d^2}{2}\frac{1}{i2k^2}[-(2i+kd)(1+n)e^{i2kd}+$$
$$(i4n-2kd)e^{ikd}+(2i-kd)(1-n)]$$
$$= \frac{\epsilon_0(\epsilon-1)\Delta E_0 d^2}{i4k^2}[-(2i+kd)(1+n)e^{i2kd}+$$
$$(i4n-2kd)e^{ikd}+(2i-kd)(1-n)] \tag{A.35}$$

and the full expression of electric quadrupole is:

$$Q^{(e)} = \begin{pmatrix} 0 & 0 & Q_{xz}^{(e)} \\ 0 & 0 & 0 \\ Q_{zx}^{(e)} & 0 & 0 \end{pmatrix} \tag{A.36}$$

A.2.5 Magnetic Quadrupole (MQ)

The magnetic quadrupole component $Q_{\alpha\beta}^{(m)}$ can be expressed as following:

$$Q_{\alpha\beta}^{(m)} = \frac{1}{3c}\int \mathrm{d}^3r[\mathbf{r}\times\mathbf{J}]_\alpha + r_\beta + \{\alpha \leftrightarrow \beta\} \tag{A.37}$$

Because of $Jy = Jz = 0$ and also the symmetric interval $[-\frac{d}{2}, \frac{d}{2}]$,only $Q_{yz}^{(m)}$ and $Q_{zy}^{(m)}$ is non-vanishing, the value of these two terms is equal to each other, and it can be give by:

$$Q_{zy}^{(m)} = Q_{yz}^{(m)} = \frac{1}{3c}\int_{-\frac{d}{2}}^{\frac{d}{2}}\mathrm{d}x\int_{-\frac{d}{2}}^{\frac{d}{2}}\mathrm{d}y\int_{-\frac{d}{2}}^{\frac{d}{2}} z^2J_x(z)\mathrm{d} + \frac{1}{3c}\int_{-\frac{d}{2}}^{\frac{d}{2}}\mathrm{d}x\int_{-\frac{d}{2}}^{\frac{d}{2}} -y^2\mathrm{d}y\int_{-\frac{d}{2}}^{\frac{d}{2}} J_x(z)\mathrm{d}$$
$$= \frac{i\omega\epsilon_0(\epsilon-1)\Delta E_0}{3c}\Big[\int_{-\frac{d}{2}}^{\frac{d}{2}}\mathrm{d}x\int_{-\frac{d}{2}}^{\frac{d}{2}}\mathrm{d}y\int_{-\frac{d}{2}}^{\frac{d}{2}} z^2V(z)\mathrm{d}z+$$
$$\int_{-\frac{d}{2}}^{\frac{d}{2}}\mathrm{d}x\int_{-\frac{d}{2}}^{\frac{d}{2}} -y^2\mathrm{d}y\int_{-\frac{d}{2}}^{\frac{d}{2}} V(z)\mathrm{d}z\Big] \tag{A.38}$$

The first term is equal to $-\frac{1}{2}$eq.A.30 and the second term is equal to $\frac{1}{2}$eq.A.29. By substituting eq.A.30 and eq.A.29 into eq.A.38 , one can get the expression of $Q_{yz}^{(m)}$ and $Q_{zy}^{(m)}$ as

$$\begin{aligned} Q_{zy}^{(m)} = Q_{yz}^{(m)} = \frac{i\omega\epsilon_0(\epsilon-1)\Delta E_0}{3c}\Big\{ & \frac{d^4}{i6k}\big[(1+n)e^{i2kd} - 2e^{ikd} + (1-n)\big] \\ & - \frac{d^2}{k^3}\big[-(i2+kd)(1+n)e^{i2kd} + \\ & (i4-2kdn)e^{ikd} - (1-n)(i2-kd)\big]\Big\} \end{aligned} \tag{A.39}$$

and the full expression of electric quadrupole is:

$$Q^{(m)} = \begin{pmatrix} 0 & 0 & 0 \\ 0 & 0 & Q_{yz}^{(e)} \\ 0 & Q_{zy}^{(e)} & 0 \end{pmatrix} \tag{A.40}$$

A.2.6 Electric Octupole (EO)

The electric octupole component $O_{\alpha\beta\gamma}^{(e)}$ can be expressed as following:

$$\begin{aligned} Q_{\alpha\beta\gamma}^{(e)} = \frac{1}{i6\omega}\int \mathrm{d}^3 r\Big[& J_\alpha\Big(\frac{r_\beta r_\gamma}{3} - \frac{r^2}{5}\delta_{\beta\gamma}\Big) + r_\alpha\Big(\frac{J_\beta r_\gamma}{3} + \frac{r_\beta J_\gamma}{3} - \frac{2}{5}(\mathbf{r}\cdot\mathbf{J})\delta_{\beta\gamma}\Big) + \\ & \{\alpha \leftrightarrow \beta,\gamma\} + \{\alpha \leftrightarrow \gamma,\beta\}\Big] \end{aligned} \tag{A.41}$$

Considering the condition $Jy = Jz = 0$ and also the symmetric interval $[-\frac{d}{2}, \frac{d}{2}]$,only $O_{xzz}^{(e)}$ is non-vanishing, simplified expression of xzz component of EO moment can be give by:

$$\begin{aligned} O_{xzz}^{(e)} &= \frac{1}{i6\omega}\int_{-\frac{d}{2}}^{\frac{d}{2}}\int_{-\frac{d}{2}}^{\frac{d}{2}}\int_{-\frac{d}{2}}^{\frac{d}{2}}\Big(\frac{4z^2}{5} - \frac{3x^2}{5} - \frac{y^2}{5}\Big)J_x(z)\mathrm{d}x\mathrm{d}y\mathrm{d}z \\ &= \frac{\epsilon_0(\epsilon-1)\Delta E_0}{6}\int_{-\frac{d}{2}}^{\frac{d}{2}}\Big(\frac{4z^2}{5} - \frac{3x^2}{5} - \frac{y^2}{5}\Big)V(z)\mathrm{d}x\mathrm{d}y\mathrm{d}z \end{aligned} \tag{A.42}$$

By substituting eq.A.28, eq.A.29 and eq.A.30 into eq.A.42 , one can get the expression of $O_{xzz}^{(e)}$ as

$$\begin{aligned} O_{xzz}^{(e)} = \frac{\epsilon_0(\epsilon-1)\Delta E_0}{6}\Big\{ & \frac{2d^4}{i15k}\big[(1+n)e^{i2kd} - 2e^{ikd} + (1-n)\big] \\ & - \frac{4d^2}{5k^3}\big[-(i2+kd)(1+n)e^{i2kd} + (i4-2kdn)e^{ikd} - (1-n)(i2-kd)\big]\Big\} \end{aligned} \tag{A.43}$$

A.3 Far-field radiation intensity contributed from multipoles

The six leading contributions to far-field light intensity radiated in the reflection direction can be calculated as:

$$I_{ED} = \left| \frac{\mu_0 c^2}{2d^2} (-ikp_x) \right|^2 \tag{A.44a}$$

$$I_{MD} = \left| \frac{\mu_0 c^2}{2d^2} (ikm_y) \right|^2 \tag{A.44b}$$

$$I_{TD} = \left| \frac{\mu_0 c^2}{2d^2} (-k^2 T_x) \right|^2 \tag{A.44c}$$

$$I_{EQ} = \left| \frac{\mu_0 c^2}{2d^2} (k^2 Q_{xz}^{(e)}) \right|^2 \tag{A.44d}$$

$$I_{MQ} = \left| \frac{\mu_0 c^2}{2d^2} (-\frac{k^2}{2} Q_{yz}^{(m)}) \right|^2 \tag{A.44e}$$

$$I_{EO} = \left| \frac{\mu_0 c^2}{2d^2} (ik^3 O_{xzz}^{(e)}) \right|^2 \tag{A.44f}$$

where μ_0 is the permeability of free space. Fig. A.3 shows that numerical and analytical values of the radiation intensity for the different multipoles and they are in a perfect agreement.

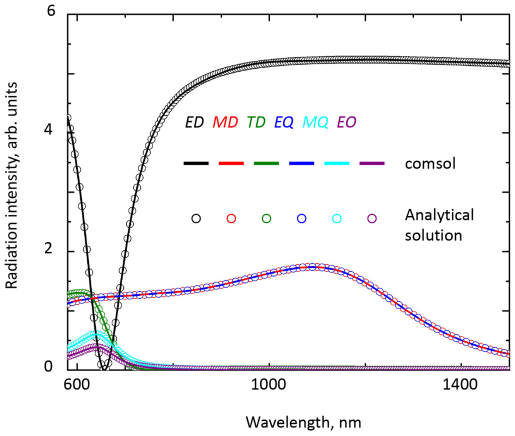

FIGURE A.3: Spectral dependences, obtained by numerically solving Maxwell's equations (solid lines) and analytically (open circles), of far-field radiation intensity contributions from the induced electric dipole (ED, black), magnetic dipole (MD, red), toroidal dipole (TD, olive), electric quadrupole (EQ, blue), magnetic quadrupole (MQ, cyan) and electric octupole (EO, magenta).

Appendix B

The role of light polarization on the performance of nanomechanical metamaterials

As the geometry of metamolecule in nanomechanical metamaterials utilized in this thesis is not spatially homogeneous, the polarization state of incident light could have an impact on the performance of the fabricated sample. Here, the influence polarization of incident light on the nanomechanical metamaterials is explored in this appendix both numerically and experimentally.

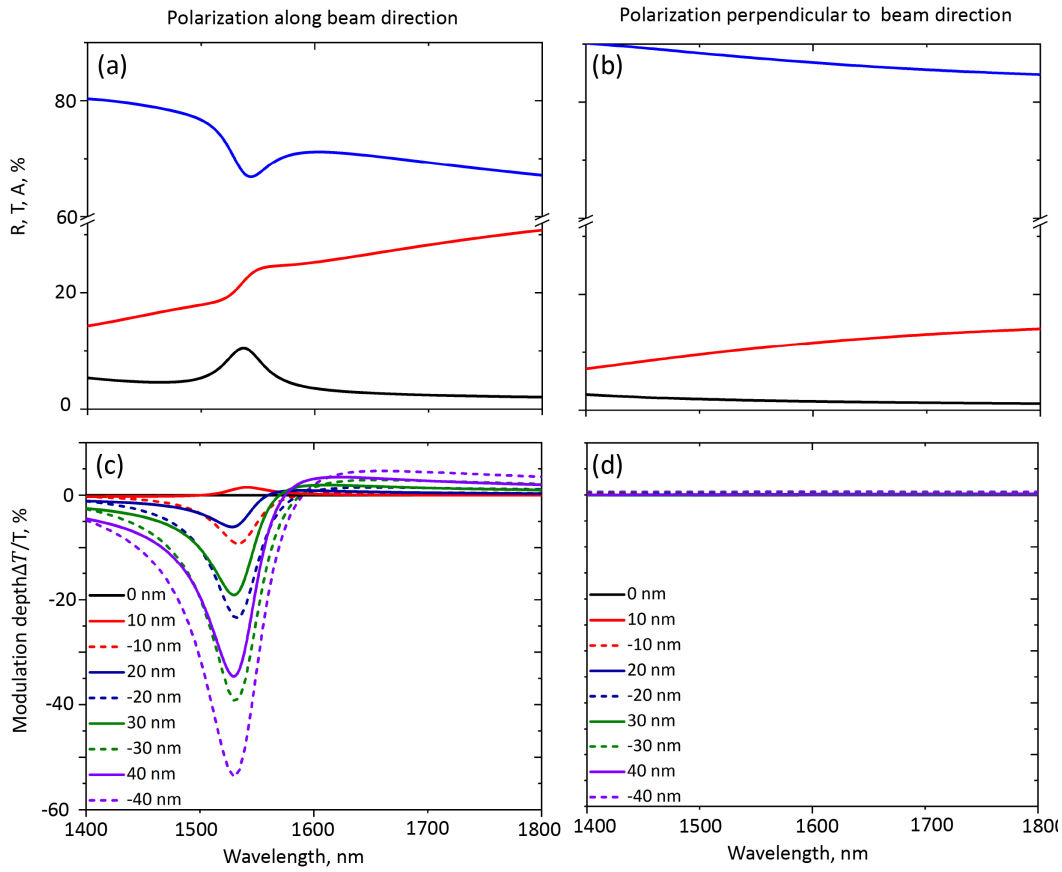

FIGURE B.1: Simulated linear properties of nanomechanical metamaterials illuminated by plane wave with different polarization states. (a) (b) Simulated reflection, transmission and absorption spectra of based on the size of dielectric sample utilized in chapter 3 for the polarization along(a) and perpendicular (b) to the beam direction. (c)(d) Modulation depth of transmitted light for the light polarization along (c) and perpendicular(d)to the beam direction.

Fig. B.1(a)(b) shows the simulated reflection, transmission and absorption spectra based on the dimensions of sample utilized in chapter 3 for the light polarization along and perpendicular to the beam direction. One could only see the resonance around the laser wavelength(1550 nm) for the light polarization along the beam direction(Fig. B.1(a)) , because that is what we designed for. And all of three curves for the orthogonal polarization is nearly flat(Fig. B.1(b)). I then investigate the modulation behaviour of the nanomechanical metamaterial induced by relative displacement between neighbouring beams in Fig. B.1(c)(d). One could see that there is pronounced modulation depth observed near the resonance in Fig. B.1(c), and this modulation behaviour gradually disappeared when the wavelength moving away from the resonance. While there is no obvious modulation behaviour observed in Fig. B.1(c) where the light polarization is perpendicular to beams.

In the experiment, amplitude spectral density spectra of this sample is measured (see Fig. B.2)for incident light with polarization along and perpendicular to the beams. one could see that there is no eigenmodes observable in the spectra for the situation where light perpendicular to beams (black curve). However, multipole peaks belong to the fundamental out-of-plane mode of different beams can be found when the light polarization is along the beam direction(red curve). Therefore, the polarization states of light need to be fine controlled in order to optically excite the mechanical modes efficiently.

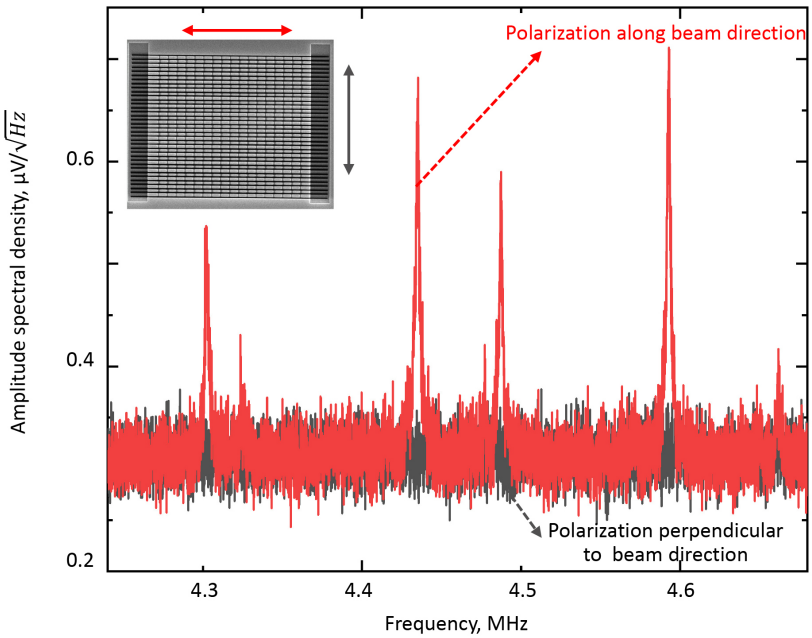

FIGURE B.2: Measured amplitude spectral density of all-dielectric nanomechanical metamaterials with incident laser polarization along (red curve) and perpendicular(black curve) to the beam direction with incident power of 19.6 μW. The inset shows relative orientation between sample and two different polarization states.

Appendix C

Influences of air damping on thermal motions in nanomechanical metamaterials

In the chapter 2, a vacuum chamber is designed and utilized in the apparatus to reduce the impact from air damping on the components of nanomechanical metamaterials. A forced mechanical oscillator with damping can be utilized to analytical investigate the influence from air damping on the motion of beams. The dynamic equation of motion of a oscillator with mass m can be written as:

$$\ddot{z} + 2n_c\dot{z} + \Omega z = \frac{F_0 e^{i\omega t}}{m} \tag{C.1}$$

where $\Omega = \sqrt{\frac{k}{m}}$ is the natural eigenfrequency of oscillator, k is the spring constant, $n_c = \frac{\mu}{2m}$ is the coefficient of damping and damping ratio is define as $\xi = \frac{n_c}{\Omega}$. The external driving stimuli is defined as a harmonic force $F_0 e^{i\omega t}$. The analytical solution of eq. C.1 can be expressed as:

$$|z| = \frac{F_0/k}{\sqrt{\left(1 - (\frac{\omega}{\Omega})^2\right)^2 + 4\xi^2(\frac{\omega}{\Omega})^2}} \tag{C.2}$$

and the resonant frequency ω_r can be obtained when eq. C.2 have the maximum and it can be given as:

$$\omega_r = \Omega\sqrt{1 - 2\xi} \tag{C.3}$$

The quality factor Q can be written as:

$$Q = \frac{\sqrt{1 - 2\xi^2}}{2\xi} \tag{C.4}$$

From eq. C.3 and C.4, one can see that the eigenfrequency of the system slightly move to lower frequency range and the quality factor tends to be decreased with the increase of the damping ξ.

In our experiment, different air pressure play a similar role on the beams like damping ratio on the classic mechanical oscillators described above. Fig. C.1 shows

the amplitude spectra density for different pressure levels. one could see that the eigenfrequency of nanomechanical metamaterials blue-shifted to lower frequency and the Q-factor slightly changed when the pressure increases from $4.6 \times 10^{-3} mbar$ to $1.92 \times 10^{-3} mbar$, which matched the anlytical prediction in eq. C.3 and C.4 well. The amplitude of peaks also decreased with the increase of air pressure. Furthermore, when the pressure increase to near to the 1 atm level, the peaks completely disappeared. This gives a clear clue that why a vacuum chamber is necessary in the measurement.

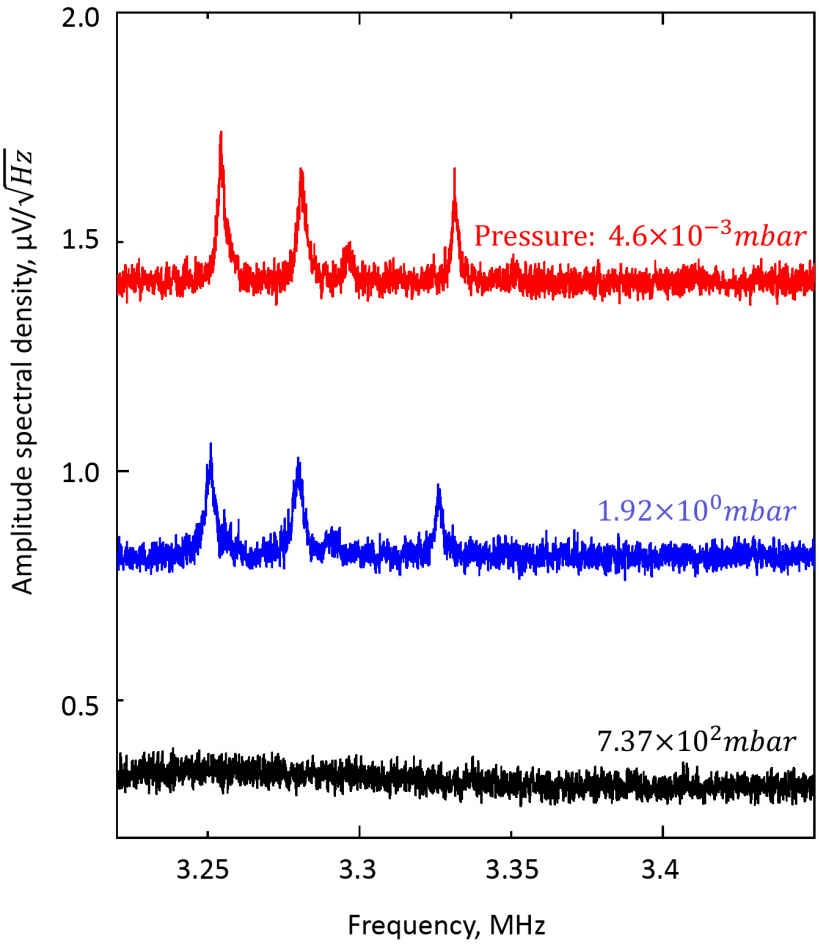

FIGURE C.1: Measured amplitude spectral density of nanomechanical metamaterials with different pressures in the vacuum chamber

Appendix D

Parametric sweep of nanomechanical metamaterials

In Fig. 5.10, the length of the brick has been swept, and the parameter selected for the simulation of asymmetric transmission is nearly at the optimum length range at the given thickness of Si and Si_3N_4. Here in this appendix, the thickness of Si and Si_3N_4 is swept for giving more information on dimension optimization.

Fig. D.1(c) and (d) gives the transmission spectrum and relative optical forces between neighbouring beams dispersion for different thickness of Si. It can be see from Fig. D.1(c) that the resonant wavelengths are red-shifted and the transmittance goes down when Si layer increase from 55 nm to 145 nm. The forces dispersion (Fig. D.1(d)) also moves to longer wavelength, but the amplitude of forces are gradually decreased due to the decrease of the Q-factor of transmission spectrum.

In terms of the influence from thickness of Si_3N_4 on the optical forces and transmission spectrum, the increased thickness (from 185 nm to 400 nm)of Si_3N_4 moves the resonant to the long wavelength range (see D.2(c)) , similar to the trend observed in D.1(c) as both the increase of the thickness of Si and Si_3N_4 can be treat as the increase of the effective refractive index, In the mean time, the maximum optical forces go down slowly.

In Fig. 5.10 and also the two figures shown in this appendix, the length and thickness of structures are swept for optimization of nanomechanical metamaterials.

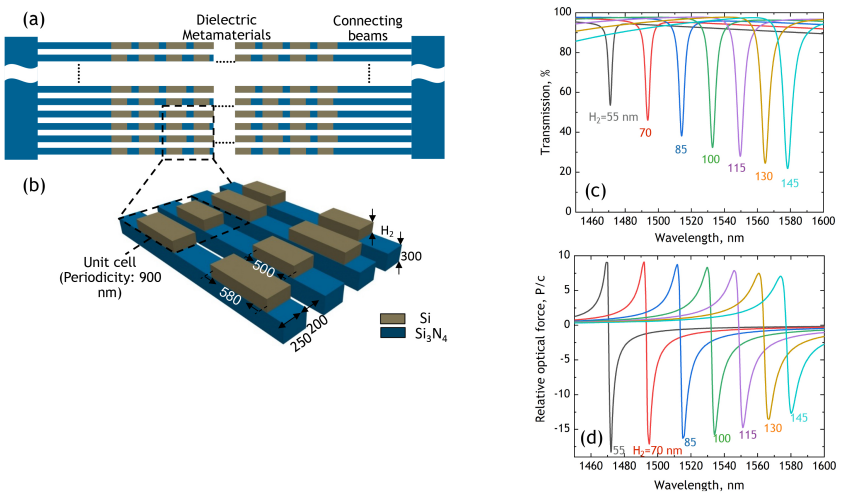

FIGURE D.1: (a)The overview schematics of studied nanomechanical metamaterials, (b) zoom-in image with dimensional information annotated, (c) the transmission spectrum for different thickness of Si: H_2, (d) optical forces dispersion for different H_2

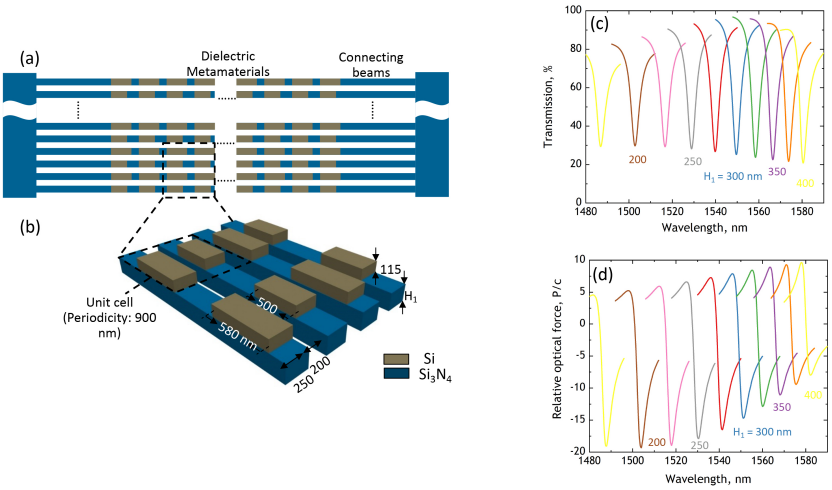

FIGURE D.2: (a)The overview schematics of studied nanomechanical metamaterials, (b) zoom-in image with dimensional information annotated, (c) the transmission spectrum for different thickness of Si_2N_4: H_1, (d) optical forces dispersion for different H_1

Apart from these three parameters, there are still others can be further optimized, like the size of metamolecule, the gap between two beams and so on. It is easy to optimize one parameters to achieve the best performance of the system, but this kind of optimization usually just a local optimized solution. It is a challenge task to gain a global optimum, to achieve so one must consider all the dimensions as variable and also the practical fabrication conditions need to be taken into consideration, imply the difference between different elements must can be recognized by manufacturing machine and so on. All of these require massive computational resources and it is very time-consuming. Artificial intelligence could potentially do the global optimization for a large group of variables and speed up the design process.

Appendix E

Fabrication and characterization of a nanowires sample with different thickness

In the Section 5.3.1, the design based on nanowires with different thickness was proposed. Here in this appendix, a fabricated nanowire sample with different thickness can be found in Fig. E.1(a)(b). This asymmetric nanowire (different height) sample

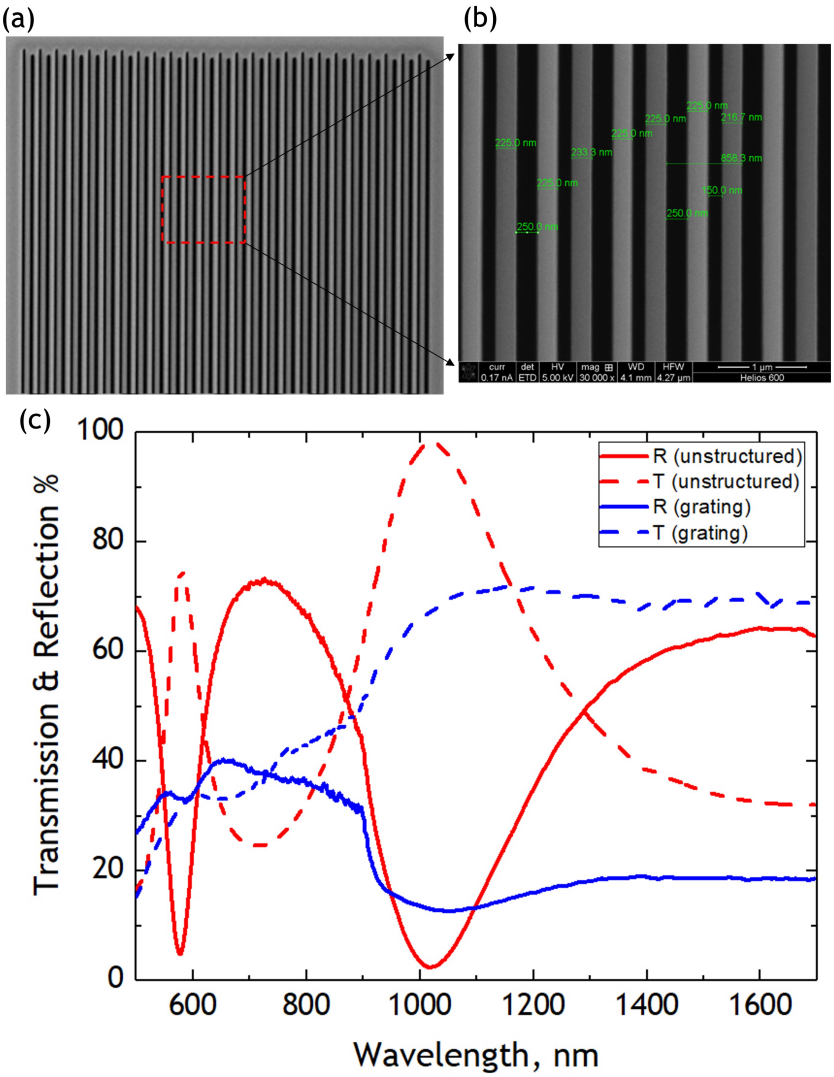

FIGURE E.1: (a) The SEM image of nanowire sample. The thickness of dark type beam is 150 nm, bright type beam is 200 nm (b) Enlarged image for a square area (indicates by red dash square), the dimensional details are marked on the image. (c) the transmission and reflection spectrum of nanowire sample and unstructured area.

is fabricated based on Si ($50nm$) and Si_3N_4 ($200nm$) bilayer membrane via focus ion beam method. Fig. E.1(a) shows SEM image of fabricated sample. Dark one indicates thin beam with thickness of $150nm$, while bright one indicates thick beam with thickness of $200nm$. Fig. E.1(b) gives the zoom-in view of black square area and dimension details are marked in this image. It can be seen that most of beams have width around $225nm$ separated with around $250nm$ width gap. The characterization results are shown in Fig. E.1(c), where transmission and reflection spectra were measured for unstructured area (red dash and solid lines) and our sample (blue dash and solid lines). For unstructured areas(red lines), we can see two resonance appeared at around $577nm$ and $1014nm$ because of Fabry-Perot cavity consisting of Si and Si_3N_4 membrane. However, there is no expected resonances in the near infrared are observed. We think that the reason is because of the loss induced by gallium ion contamination. As we mentioned, if the loss is to high, such as $\kappa = 0.1$, the resonance will disappear, see Fig. 5.5. In terms of the solutions of $Ga+$ contamination, one could either explore a structure that is not as sensitive as this type of design or use EBL method to fabricated the sample to mitigate Ga^+ contamination.

Appendix F

Thermal motion behaviours of the nanomechanical metamaterial sample for measuring asymmetric transmission

As mentioned in Chapter 3 and 4 that thermal fluctuations of the transmission of nanomechanical photonic metamaterials are capable of giving information on eigenfrequencies and damping of the mechanical modes[96]. In this appendix, the mechanical properties of the sample utilized in Chapter 5 is characterized via thermal fluctuation experiment, in which the setup is similar to Fig. 4.2(a), but here laser wavelength is selected as 1535 nm, rather than 1550 nm (See setup in Fig. F.1(a)), as the absorption peak appears at 1535 nm(Fig. 5.11(b)), giving rise to larger thermal fluctuation on transmitted signal.

Fig. F.1(b) show an example of amplitude spectral density (ASD) at incident laser power of 39.2 μW with backward illumination (incident from Si_3N_4 side). There are two thermal peaks observed in the ASD spectra, which associating with the fundamental out-of-plane modes of a pair of individual beams – one narrow type ① and one wide type ② beams as indicated in the inset of Fig. 5.11(a). And this attribution is confirmed through computational modelling. Beam displacement ASD can be expressed as eq. 4.1 and experimental data can thus be calibrated – the vertical scale in Fig. F.1(b) converted from signal measured in μV to nanowire displacement in picometres, by fitting Eq. 4.1 to the data, shown in the magenta curves of fitted data. The fitted parameters for each of the thermal peaks with co-optimized values of m_{eff}, f_0 and Q can be found in the inset of Fig. F.1(b). where the eigenfrequencies of these two fundamental modes are at f_0=6.298 MHz and 6.341 MHz, and effective mass for these two type of beams ① and ②, m_{eff} =1.37 and 2.02 pg. The Root mean square (RMS) displacement can then be evaluated as the square root of an integral of power spectral density (ASD^2) over frequency shown in eq. 4.2, giving RMS displacement around 41.6 pm and 35.0 pm for type ① and ②, respectively. The simulated model profile of these mode can also be found in the inset of Fig. F.1(b). Furthermore, the power depencence measurements are conducted for forward and backward illumination in Fig. F.1(d) and (e) to calibrate our characterization system, which is the same measurement process like I conduct in Chapter 4. There are two main peaks linking to the out-of-plane modes of two type of beams ① and ② in both forward (Fig. F.1(d)) and backward (Fig. F.1(e)) illumination and that is similar to what I observed in Chapter 4. Both of these two eigenmodes are red-shifted with the increase of incident pump power for both

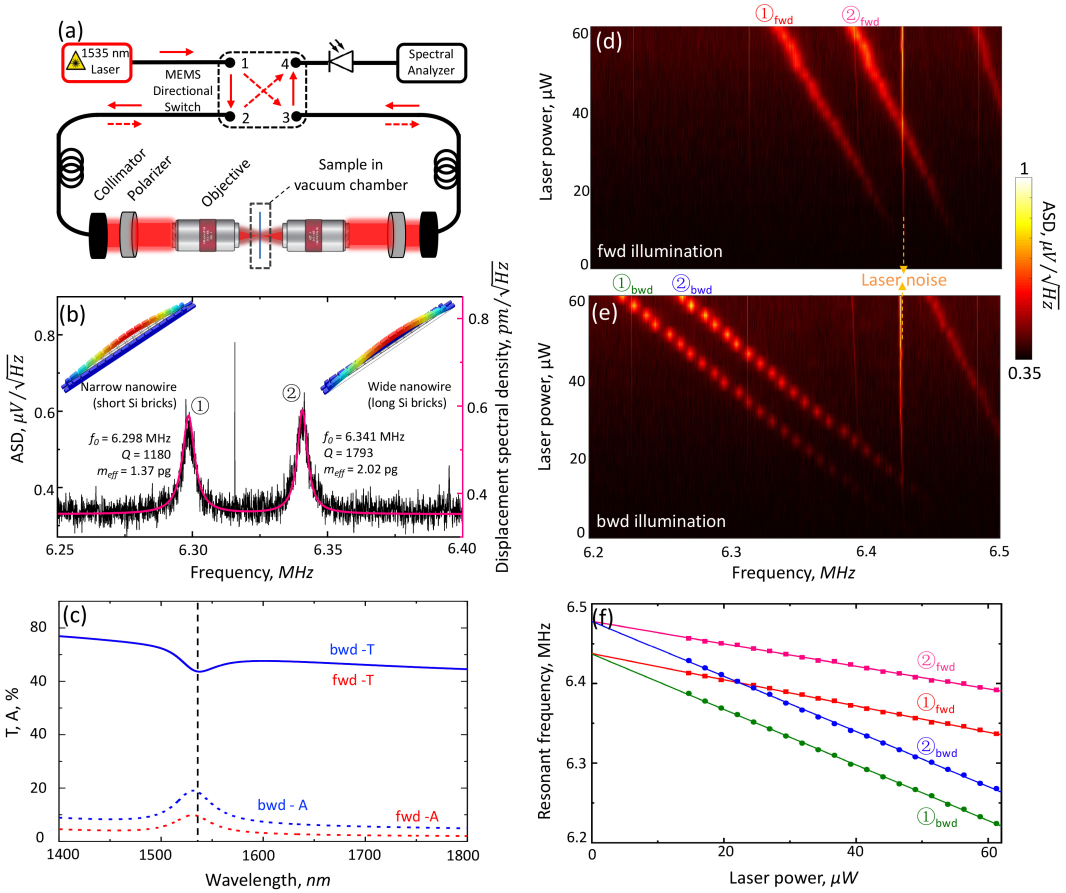

FIGURE F.1: Identification of fundamental mechanical out-of-plane modes of the nanomechanical metamaterials via thermal motion measurement. (a) Schematic of experimental setup for recording amplitude spectral density (ASD) of metamaterial transmission, it is identical to the setup in the Fig. 4.2(a), except the laser wavelength here is tuned to 1535 nm, where absorption of sample is maximized, giving better signal to noise ratio in the measurement. (b) Typical measurement of optical transmission ASD[for light incident from bwd side at a power level of $39.2\mu W$], showing a pair of peaks associated with the mechanical resonances of two individual nanowires within the array: ①/② a narrower/wider wire decorated with shorter/longer Si bricks. The overlaid magenta curve and calibrated displacement spectral density scale [to the right-hand side] are obtained by fitting Eq. 4.1 to the experimental data. Derived values of f_0, Q and m_{eff} are shown inset. Numerically simulated mode profile of the out-of-plane mechanical mode of these two types of nanowire also shown in the inset. (c) Simulated transmission and absorption spectra for fwd and bwd illumination, in which laser wavelength utilized in this experiment annotated with a black dashed line. (d)(e) Mapping for transmission amplitude spectral density for a range of laser power levels, showing peaks ① and ②as assigned in (b), for opposing directions of light propagation through the sample – (d) forward and (e) backward illumination. (f)Solid circles shows resonant frequency evaluated from (d) and (e), assigned to type ①/② nanowires for forward and backward illumination, while solid lines show the fitting results of these four group of data.

forward and backward illumination because tensil stress inside of beams altered by increased temperature induced by photo-thermal effects, which determined by the absorption. In Fig. F.1(f), I evaluated the eigen-frequency fromFig. F.1(d) and (e). One could found that the shifting rate of eigenfrequency for backward illumination is faster than that for forward illumination, implying that the absorption coefficient

of backward illumination direction is larger than that of forward direction, giving more temperature rise for the same input laser power level, this assumption is verified by the simulated absorption spectra in Fig. F.1(c). However, these eigenfrequencies differences from different illumination direction tend to gradually disappear with the decrease of laser power. And in the end, the thermal peaks are expecting converge to same frequency for opposite illuminations when laser power declines to zero if the setup is symmetric and in a good stability during the measurement process. It can be seen from Fig. F.1(c) that the eigenfrequencies of both these two fundamental eigenmodes for forward and backward illuminations merge together (at 6.437 MHz and 6.478 MHz for nanowire type ① and ②, respectively) at zero power, implying a good symmetry of the current experiment setup.

Appendix G

Thermal modulation tails of the nanomechanical metamaterials sample for measuring asymmetric transmission

Aforementioned in Chapter 5, the optical forces play a dominant role in modulating transmitted light at relative high natural eigenfrequencies (around 6MHz) of nanomechanical metamaterials, because a slightly change of optical forces, by varying the pump laser wavelength, could produce a significant change of modulation amplitude as shown in Fig. 5.15. It would be interesting to check the modulation behaviour of transmitted light at low frequency range, where thermal forces dominant.

Fig. G.1 shows that optical pump could lead to observable modulation of the metamaterials's transmission at low modulation frequency (below 500 kHz), which is far away from the eigenfrequencies of beams in nanomechanical metamaterials. For the pump power of 24.5 μW, a modulation amplitude of around 3 % is observed at 30 kHz modulation. This is a relative large effects as the interaction length of light and metamaterials is only around one fifth of the probe wavelength. These low frequency components of nonlinear response have a thermal nature and drops with increasing modulation frequency, fading at a few 100s of kHz. The photothermal induced heating of the beams is balanced by heat conduction along the metamaterial beams and the average temperature within beams can rise up to 10s of Kelvin from room temperature according to the estimation from frequency shifts (see Fig. F.1(f)). The bending of beams in nanomechanical metamaterials due to the thermal expansion coefficient difference of Si and Si_3N_4 create the modulation

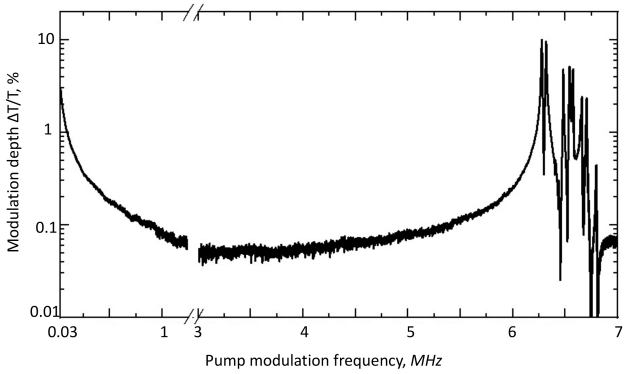

FIGURE G.1: Thermal tail of the nanomechanical metamaterials at a wide frequency range(30 KHz to 7 MHz) at pump power of 24.5 μW, pump and probe wavelength is 1535nm and 1540nm, respectively.

of the transmitted light. Optical forces gradually become the main driven source of the bending of beams when the pump frequency close to the eigenfrequencies of nanomechanical metamaterials.

List of Publications

Articles

1. **J. Li**, K. F. MacDonald, and N. I. Zheludev, *Asymmetric response of nano-opto-mechnical photonic metamaterial*[In preparation].

2. **J. Li**, K. F. MacDonald, and N. I. Zheludev, *Optical Control of Nanomechanical Brownian Motion Eigenfrequencies in Metamaterials*, Nano Letters, **22**(11),4301-4306(2022).

3. **J. Li**, D. Papas, T. Liu, J. Ou, E. Plum, K. F. MacDonald, and N. I. Zheludev, *Thermal fluctuations of the optical properties of nanomechanical photonic metamaterials*, Advanced Optical Materials, **10**(5), 2101591(2021).

4. **J. Li**, N. Papasimakis, K. F. MacDonald, and N. I. Zheludev, *Optical magnetic response without metamaterials*, APL Photonics, **6**(7), 071303(2021).

5. **J. Li**, B. Gholipour, D. Piccinotti, K. F. MacDonald, and N. I. Zheludev, *Ultraviolet hollow-core waveguides with sub-unitary index chalcogenide cladding*, Optical Material Express,**10**(9), 2254-2261(2020).

Conference contributions

1. **J. Li**, K. F. MacDonald and N. I. Zheludev, *Reconfiguring Photonic Metamaterials with the Pressure of Light*, CLEO 2022, California, 15-20 May, 2022.

2. **J. Li**, K. F. MacDonald and N. I. Zheludev, *Reconfiguring Metamaterials with the Pressure of Light*, Nanometa 2022, Seefeld, 28-31 Mar, 2022.

3. **J. Li**, T. Liu; K. F. MacDonald, J. Y. Ou, D. Papas, E. Plum, and N. I. Zheludev, *Flat Photonic Devices Based on Nanomechanical Metamaterials Driven by Light, Sound, Electric and Magnetic signals*, Optical Design and Fabrication Congress, Virtual Conference, 27 Jun - 1 Jul 2021.

4. **J. Li**, K. F. MacDonald and N. I. Zheludev, *Asymmetric Transmission in Nano-opto-mechanical Metamaterials at μW Power Levels*, CLEO/Europe-EQEC 2021 Virtual Meeting, 21 - 25 June 2021.

5. **J. Li**, N. Papasimakis, K. F. MacDonald, and N. I. Zheludev, *Optical Magnetism without Metamaterials*, CLEO/Europe-EQEC 2021 Virtual Meeting, 21 - 25 June 2021.

6. **J. Li**, K. F. MacDonald and N. I. Zheludev, *Transmission Asymmetry in Nano-opto-mechanical Metamaterials*, Photon 2020, Virtual conference, 1-4 Sep 2020.

7. **J. Li**, K. F. MacDonald and N. I. Zheludev, *Transmission Asymmetry in All-dielectric opto-mechanical Metamaterials*, Smart NanoMaterials 2020 Virtual Conference, 8-11 Dec 2020.

8. (poster)**J. Li**, K. F. MacDonald and N. I. Zheludev, *Transmission Asymmetry in Nano-opto-mechanical Metamaterials*, CLEO 2021 Virtual Conference, 9-14 May 2021.

9. (poster) **J. Li**, B. Gholipour, D. Piccinotti, K. F. MacDonald, and N. I. Zheludev, *Hollow-Core Waveguides With $n < 1$ Chalcogenide Cladding*, Nanometa 2019, Seefeld, Austria, 3 - 6 Jan 2019.

10. (poster)J. Y. Ou, D. Papas, T. Liu, **J. Li**, E. Plum, K. F. MacDonald, and N. I. Zheludev, *Thermal Fluctuations in the Optical Properties of Dielectric and Plasmonic Nanomechanical Metamaterials*, Nanometa 2022, Seefeld, Austria, 28-31 Mar 2022.

11. C. Rendón-Barraza, E. A. Chan, **J. Li**, T. Liu, K. F. MacDonald, J.Y. Ou, D. Papas, N. Papasimakis, E. Plum, T. Pu, G. Yuan, and N. I. Zheludev, *Picophotonics*, 15th International Congress on Artificial Materials for Novel Wave Phenomena, Virtual Meeting, 20-26 Sept 2021.

12. T. Liu, **J. Li,** D. Papas, J. Y. Ou, E. Plum, K. F. MacDonald, and N. I. Zheludev, *Metamaterial nanomachines driven by heat, sound, electric and magnetic fields, and light*, SPIE Optics & Photonics 2021, Virtual Conference, 1 - 5 Aug 2021.

13. J. Y. Ou, T. Liu, **J. Li**, D. Papas, E. Plum, K. F. MacDonald, and N. I. Zheludev, *Dynamics of nanomechanical metamaterials: Pico-vibrometry with light and electron beams*, META 2021, Virtual Conference, 20 - 23 July 2021.

14. E. Plum, D. Papas, **J. Li**, T. Liu, J. Y. Ou, Q. Zhang, G. Lan, K. F. MacDonald, and N. I. Zheludev, *Nanomechanical photonic metamaterials*, Materials for Humanity (MH21), Virtual Conference, 6-9 July 2021.

15. N. I. Zheludev, D. Papas, T. Liu, **J. Li,** Q. Zhang, J. Y. Ou, E. Plum, and K. F. MacDonald, Functional *Nanomechanical Metamaterials Driven by Light, Electromagnetic Forces and Sound*, CLEO 2020 Virtual Conference, 11-15 May 2020.

Bibliography

[1] M. Wuttig, H. Bhaskaran, and T. Taubner, "Phase-change materials for non-volatile photonic applications," *Nature Photonics*, vol. 11, no. 8, pp. 465–476, 2017.

[2] H. J. Caulfield and S. Dolev, "Why future supercomputing requires optics," *Nature Photonics*, vol. 4, no. 5, pp. 261–263, 2010.

[3] A. K. Sarychev and V. M. Shalaev, *Electrodynamics of Metamaterials*. World Scientific Publishing Co. Pte. Ltd., 2007.

[4] R. A. Shelby, D. R. Smith, and S. Schultz, "Experimental verification of a negative index of refraction," *Science*, vol. 292, no. 5514, pp. 77–79, 2001.

[5] J. B. Pendry, "Negative refraction makes a perfect lens," *Physical Review Letters*, vol. 85, no. 18, pp. 3966–3969, 2000.

[6] F. Monticone and A. Alù, "The quest for optical magnetism: From split-ring resonators to plasmonic nanoparticles and nanoclusters," *Journal of Materials Chemistry C*, vol. 2, no. 43, pp. 9059–9072, 2014.

[7] V. Savinov, V. A. Fedotov, S. M. Anlage, P. A. J. de Groot, and N. I. Zheludev, "Modulating sub-THz radiation with current in superconducting metamaterial," *Physical Review Letters*, vol. 109, no. 24, 2012.

[8] Z. L. Sámson, K. F. MacDonald, F. D. Angelis, B. Gholipour, K. Knight, C. C. Huang, E. D. Fabrizio, D. W. Hewak, and N. I. Zheludev, "Metamaterial electro-optic switch of nanoscale thickness," *Applied Physics Letters*, vol. 96, no. 14, p. 143 105, 2010.

[9] T. Driscoll, H.-T. Kim, B.-G. Chae, B.-J. Kim, Y.-W. Lee, N. M. Jokerst, S. Palit, D. R. Smith, M. D. Ventra, and D. N. Basov, "Memory metamaterials," *Science*, vol. 325, no. 5947, pp. 1518–1521, 2009.

[10] Q. Wang, E. T. F. Rogers, B. Gholipour, C.-M. Wang, G. Yuan, J. Teng, and N. I. Zheludev, "Optically reconfigurable metasurfaces and photonic devices based on phase change materials," *Nature Photonics*, vol. 10, no. 1, pp. 60–65, 2015.

[11] H. Tao, A. C. Strikwerda, K. Fan, W. J. Padilla, X. Zhang, and R. D. Averitt, "Reconfigurable terahertz metamaterials," *Physical Review Letters*, vol. 103, no. 14, p. 147 401, 2009.

[12] W. Zhang, A. Q. Liu, W. M. Zhu, E. P. Li, H. Tanoto, Q. Y. Wu, J. H. Teng, X. H. Zhang, M. L. J. Tsai, G. Q. Lo, and D. L. Kwong, "Micromachined switchable metamaterial with dual resonance," *Applied Physics Letters*, vol. 101, no. 15, p. 151 902, 2012.

[13] M. Lapine, I. V. Shadrivov, D. A. Powell, and Y. S. Kivshar, "Magnetoelastic metamaterials," *Nature Materials*, vol. 11, no. 1, pp. 30–33, 2011.

[14] N. I. Zheludev and E. Plum, "Reconfigurable nanomechanical photonic metamaterials," *Nature Nanotechnology*, vol. 11, no. 1, pp. 16–22, 2016.

[15] I. A. Ajia, J.-Y. Ou, N. J. Dinsdale, H. J. Singh, T. Chen-Sverre, T. Liu, N. I. Zheludev, and O. L. Muskens, "Gigahertz nano-optomechanical resonances in a dielectric SiC-membrane metasurface array," *Nano Letters*, vol. 21, no. 11, pp. 4563–4569, 2021.

[16] J.-Y. Ou, E. Plum, L. Jiang, and N. I. Zheludev, "Reconfigurable photonic metamaterials," in *CLEO:2011 - Laser Applications to Photonic Applications*, OSA, 2011.

[17] J.-Y. Ou, E. Plum, J. Zhang, and N. I. Zheludev, "An electromechanically reconfigurable plasmonic metamaterial operating in the near-infrared," *Nature Nanotechnology*, vol. 8, no. 4, pp. 252–255, 2013.

[18] J. Valente, J.-Y. Ou, E. Plum, I. J. Youngs, and N. I. Zheludev, "A magneto-electro-optical effect in a plasmonic nanowire material," *Nature Communications*, vol. 6, no. 1, p. 7021, 2015.

[19] J.-Y. Ou, E. Plum, J. Zhang, and N. I. Zheludev, "Giant nonlinearity of an optically reconfigurable plasmonic metamaterial," *Advanced Materials*, vol. 28, no. 4, pp. 729–733, 2015.

[20] C. L. Degen, M. Poggio, H. J. Mamin, and D. Rugar, "Nuclear spin relaxation induced by a mechanical resonator," *Physical Review Letters*, vol. 100, no. 13, p. 137 601, 2008.

[21] R. Thijssen, T. J. Kippenberg, A. Polman, and E. Verhagen, "Plasmomechanical resonators based on dimer nanoantennas," *Nano Letters*, vol. 15, no. 6, pp. 3971–3976, 2015.

[22] J. Molina, D. Ramos, E. Gil-Santos, J. E. Escobar, J. J. Ruz, J. Tamayo, Á. S. Paulo, and M. Calleja, "Optical transduction for vertical nanowire resonators," *Nano Letters*, vol. 20, no. 4, pp. 2359–2369, 2020.

[23] R. Thijssen, T. J. Kippenberg, A. Polman, and E. Verhagen, "Parallel transduction of nanomechanical motion using plasmonic resonators," *ACS Photonics*, vol. 1, no. 11, pp. 1181–1188, 2014.

[24] A. Einstein, "Über die von der molekularkinetischen theorie der wärme geforderte bewegung von in ruhenden flüssigkeiten suspendierten teilchen," *Annalen der Physik*, vol. 322, no. 8, pp. 549–560, 1905.

[25] G. E. Uhlenbeck and L. S. Ornstein, "On the theory of the brownian motion," *Physical Review*, vol. 36, no. 5, pp. 823–841, 1930.

[26] S. Chandrasekhar, "Stochastic problems in physics and astronomy," *Reviews of Modern Physics*, vol. 15, no. 1, pp. 1–89, 1943.

[27] G. I. González and P. R. Saulson, "Brownian motion of a mass suspended by an anelastic wire," *The Journal of the Acoustical Society of America*, vol. 96, no. 1, pp. 207–212, 1994.

[28] Y. Nagasaki, B. Gholipour, J.-Y. Ou, M. Tsuruta, E. Plum, K. F. MacDonald, J. Takahara, and N. I. Zheludev, "Optical bistability in shape-memory nanowire metamaterial array," *Applied Physics Letters*, vol. 113, no. 2, p. 021 105, 2018.

[29] A. Karvounis, J.-Y. Ou, W. Wu, K. F. MacDonald, and N. I. Zheludev, "Nano-optomechanical nonlinear dielectric metamaterials," *Applied Physics Letters*, vol. 107, no. 19, p. 191 110, 2015.

[30] J. Zhang, K. F. MacDonald, and N. I. Zheludev, "Nonlinear dielectric optomechanical metamaterials," *Light: Science & Applications*, vol. 2, no. 8, e96–e96, 2013.

[31] K. B. Gavan, J. van der Heijden, E. van der Drift, and H. van der Zant, "Resonance frequency behavior of silicon nitride cantilevers as a function of pressure in different gas environments," in *2009 IEEE Sensors*, IEEE, 2009.

[32] M. Aspelmeyer, T. J. Kippenberg, and F. Marquardt, *Cavity Optomechanics*. Springer Berlin Heidelberg, 2014.

[33] G. Meyer and N. M. Amer, "Novel optical approach to atomic force microscopy," *Applied Physics Letters*, vol. 53, no. 12, pp. 1045–1047, 1988.

[34] L. Bi, J. Hu, P. Jiang, D. H. Kim, G. F. Dionne, L. C. Kimerling, and C. A. Ross, "On-chip optical isolation in monolithically integrated non-reciprocal optical resonators," *Nature Photonics*, vol. 5, no. 12, pp. 758–762, 2011.

[35] L. Fan, J. Wang, L. T. Varghese, H. Shen, B. Niu, Y. Xuan, A. M. Weiner, and M. Qi, "An all-silicon passive optical diode," *Science*, vol. 335, no. 6067, pp. 447–450, 2012.

[36] F. Ruesink, M.-A. Miri, A. Alù, and E. Verhagen, "Nonreciprocity and magnetic-free isolation based on optomechanical interactions," *Nature Communications*, vol. 7, no. 1, p. 13 662, 2016.

[37] D. L. Sounas and A. Alù, "Non-reciprocal photonics based on time modulation," *Nature Photonics*, vol. 11, no. 12, pp. 774–783, 2017.

[38] L. J. Aplet and J. W. Carson, "A faraday effect optical isolator," *Applied Optics*, vol. 3, no. 4, p. 544, 1964.

[39] B. Peng, Ş. K. Özdemir, F. Lei, F. Monifi, M. Gianfreda, G. L. Long, S. Fan, F. Nori, C. M. Bender, and L. Yang, "Parity–time-symmetric whispering-gallery microcavities," *Nature Physics*, vol. 10, no. 5, pp. 394–398, 2014.

[40] N. Bender, S. Factor, J. D. Bodyfelt, H. Ramezani, D. N. Christodoulides, F. M. Ellis, and T. Kottos, "Observation of asymmetric transport in structures with active nonlinearities," *Physical Review Letters*, vol. 110, no. 23, p. 234 101, 2013.

[41] Y. Shi, Z. Yu, and S. Fan, "Limitations of nonlinear optical isolators due to dynamic reciprocity," *Nature Photonics*, vol. 9, no. 6, pp. 388–392, 2015.

[42] Z. Shen, Y.-L. Zhang, Y. Chen, C.-L. Zou, Y.-F. Xiao, X.-B. Zou, F.-W. Sun, G.-C. Guo, and C.-H. Dong, "Experimental realization of optomechanically induced non-reciprocity," *Nature Photonics*, vol. 10, no. 10, pp. 657–661, 2016.

[43] K. Fang, J. Luo, A. Metelmann, M. H. Matheny, F. Marquardt, A. A. Clerk, and O. Painter, "Generalized non-reciprocity in an optomechanical circuit via synthetic magnetism and reservoir engineering," *Nature Physics*, vol. 13, no. 5, pp. 465–471, 2017.

[44] M. Stolarek, D. Yavorskiy, R. Kotyński, C. J. Z. Rodríguez, J. Łusakowski, and T. Szoplik, "Asymmetric transmission of terahertz radiation through a double grating," *Optics Letters*, vol. 38, no. 6, p. 839, 2013.

[45] C. Wang, X.-L. Zhong, and Z.-Y. Li, "Linear and passive silicon optical isolator," *Scientific Reports*, vol. 2, no. 1, 2012.

[46] V. A. Fedotov, A. S. Schwanecke, N. I. Zheludev, V. V. Khardikov, and S. L. Prosvirnin, "Asymmetric transmission of light and enantiomerically sensitive plasmon resonance in planar chiral nanostructures," *Nano Letters*, vol. 7, no. 7, pp. 1996–1999, 2007.

[47] J. Xu, C. Cheng, M. Kang, J. Chen, Z. Zheng, Y.-X. Fan, and H.-T. Wang, "Unidirectional optical transmission in dual-metal gratings in the absence of anisotropic and nonlinear materials," *Optics Letters*, vol. 36, no. 10, p. 1905, 2011.

[48] V. Kuzmiak and A. A. Maradudin, "Asymmetric transmission of surface plasmon polaritons on planar gratings," *Physical Review A*, vol. 92, no. 5, 2015.

[49] A. Cicek, M. B. Yucel, O. A. Kaya, and B. Ulug, "Refraction-based photonic crystal diode," *Optics Letters*, vol. 37, no. 14, p. 2937, 2012.

[50] C. Lu, X. Hu, Y. Zhang, Z. Li, X. Xu, H. Yang, and Q. Gong, "Ultralow power all-optical diode in photonic crystal heterostructures with broken spatial inversion symmetry," *Applied Physics Letters*, vol. 99, no. 5, p. 051 107, 2011.

[51] V. A. Fedotov, P. L. Mladyonov, S. L. Prosvirnin, A. V. Rogacheva, Y. Chen, and N. I. Zheludev, "Asymmetric propagation of electromagnetic waves through a planar chiral structure," *Physical Review Letters*, vol. 97, no. 16, p. 167 401, 2006.

[52] C. Menzel, C. Helgert, C. Rockstuhl, E.-B. Kley, A. Tünnermann, T. Pertsch, and F. Lederer, "Asymmetric transmission of linearly polarized light at optical metamaterials," *Physical Review Letters*, vol. 104, no. 25, p. 253 902, 2010.

[53] J. Orloff, *Handbook of charged particle optics*. CRC press, 2017.

[54] A. N. Cleland, *Foundations of nanomechanics: from solid-state theory to device applications*. Springer Science & Business Media, 2013.

[55] W. Weaver Jr, S. P. Timoshenko, and D. H. Young, *Vibration problems in engineering*. John Wiley & Sons, 1991.

[56] S. Schmid, L. G. Villanueva, and M. L. Roukes, *Fundamentals of nanomechanical resonators*. Springer, 2016, vol. 49.

[57] R. B. Karabalin, L. G. Villanueva, M. H. Matheny, J. E. Sader, and M. L. Roukes, "Stress-induced variations in the stiffness of micro- and nanocantilever beams," *Physical Review Letters*, vol. 108, no. 23, p. 236 101, 2012.

[58] Y. T. Yang, C. Callegari, X. L. Feng, K. L. Ekinci, and M. L. Roukes, "Zeptogram-scale nanomechanical mass sensing," *Nano Letters*, vol. 6, no. 4, pp. 583–586, 2006.

[59] K. Jensen, K. Kim, and A. Zettl, "An atomic-resolution nanomechanical mass sensor," *Nature Nanotechnology*, vol. 3, no. 9, pp. 533–537, 2008.

[60] J. Chaste, A. Eichler, J. Moser, G. Ceballos, R. Rurali, and A. Bachtold, "A nanomechanical mass sensor with yoctogram resolution," *Nature Nanotechnology*, vol. 7, no. 5, pp. 301–304, 2012.

[61] X. C. Zhang, E. B. Myers, J. E. Sader, and M. L. Roukes, "Nanomechanical torsional resonators for frequency-shift infrared thermal sensing," *Nano Letters*, vol. 13, no. 4, pp. 1528–1534, 2013.

[62] E. Gavartin, P. Verlot, and T. J. Kippenberg, "A hybrid on-chip optomechanical transducer for ultrasensitive force measurements," *Nature Nanotechnology*, vol. 7, no. 8, pp. 509–514, 2012.

[63] D. Rugar, R. Budakian, H. J. Mamin, and B. W. Chui, "Single spin detection by magnetic resonance force microscopy," *Nature*, vol. 430, no. 6997, pp. 329–332, 2004.

[64] M. D. LaHaye, J. Suh, P. M. Echternach, K. C. Schwab, and M. L. Roukes, "Nanomechanical measurements of a superconducting qubit," *Nature*, vol. 459, no. 7249, pp. 960–964, 2009.

[65] B. Hauer, C. Doolin, K. Beach, and J. Davis, "A general procedure for thermomechanical calibration of nano/micro-mechanical resonators," *Annals of Physics*, vol. 339, pp. 181–207, 2013.

[66] M. Eichenfield, J. Chan, A. H. Safavi-Naeini, K. J. Vahala, and O. Painter, "Modeling dispersive coupling and losses of localized optical and mechanical modes in optomechanical crystals," *Optics Express*, vol. 17, no. 22, p. 20 078, 2009.

[67] A. K. Naik, M. S. Hanay, W. K. Hiebert, X. L. Feng, and M. L. Roukes, "Towards single-molecule nanomechanical mass spectrometry," *Nature Nanotechnology*, vol. 4, no. 7, pp. 445–450, 2009.

[68] M. P. Norton and D. G. Karczub, *Fundamentals of noise and vibration analysis for engineers*. Cambridge university press, 2003.

[69] W. T. Vetterling, W. H. Press, S. A. Teukolsky, and B. P. Flannery, *Numerical recipes: The Art of Scientific Computing*. Press Syndicate of the University of Cambridge, 1992.

[70] A. G. Krause, M. Winger, T. D. Blasius, Q. Lin, and O. Painter, "A high-resolution microchip optomechanical accelerometer," *Nature Photonics*, vol. 6, no. 11, pp. 768–772, 2012.

[71] M. J. Higgins, R. Proksch, J. E. Sader, M. Polcik, S. M. Endoo, J. P. Cleveland, and S. P. Jarvis, "Noninvasive determination of optical lever sensitivity in atomic force microscopy," *Review of Scientific Instruments*, vol. 77, no. 1, p. 013 701, 2006.

[72] Z. Ruan and S. Fan, "Temporal coupled-mode theory for fano resonance in light scattering by a single obstacle," *The Journal of Physical Chemistry C*, vol. 114, no. 16, pp. 7324–7329, 2009.

[73] S. Fan, W. Suh, and J. D. Joannopoulos, "Temporal coupled-mode theory for the fano resonance in optical resonators," *Journal of the Optical Society of America A*, vol. 20, no. 3, p. 569, 2003.

[74] A. B. Khanikaev, C. Wu, and G. Shvets, "Fano-resonant metamaterials and their applications," *Nanophotonics*, vol. 2, no. 4, pp. 247–264, 2013.

[75] J. D. Jackson, *Classical electrodynamics*. American Association of Physics Teachers, 1999.

[76] A. Chipouline, C. Simovski, and S. Tretyakov, "Basics of averaging of the maxwell equations for bulk materials," *Metamaterials*, vol. 6, no. 3-4, pp. 77–120, 2012.

[77] C. Craeye, "A fast impedance and pattern computation scheme for finite antenna arrays," *IEEE Transactions on Antennas and Propagation*, vol. 54, no. 10, pp. 3030–3034, 2006.

[78] W. B. Lu and T. J. Cui, "Efficient method for full-wave analysis of large-scale finite-sized periodic structures," *Journal of Electromagnetic Waves and Applications*, vol. 21, no. 14, pp. 2157–2168, 2007.

[79] A. L. Fructos, R. R. Boix, F. Mesa, and F. Medina, "An efficient approach for the computation of 2-d green's functions with 1-d and 2-d periodicities in homogeneous media," *IEEE Transactions on Antennas and Propagation*, vol. 56, no. 12, pp. 3733–3742, 2008.

[80] V. Savinov, V. A. Fedotov, and N. I. Zheludev, "Toroidal dipolar excitation and macroscopic electromagnetic properties of metamaterials," *Physical Review B*, vol. 89, no. 20, p. 205 112, 2014.

[81] S. K. Lamoreaux, "The casimir force: Background, experiments, and applications," *Reports on Progress in Physics*, vol. 68, no. 1, pp. 201–236, 2004.

[82] D. Ma and J. N. Munday, "Measurement of wavelength-dependent radiation pressure from photon reflection and absorption due to thin film interference," *Scientific Reports*, vol. 8, no. 1, p. 15 930, 2018.

[83] G. S. Agarwal, "Brownian motion of a quantum oscillator," *Physical Review A*, vol. 4, no. 2, pp. 739–747, 1971.

[84] M. Bückle, Y. S. Klaß, F. B. Nägele, R. Braive, and E. M. Weig, "Universal length dependence of tensile stress in nanomechanical string resonators," *Physical Review Applied*, vol. 15, no. 3, p. 034 063, 2021.

[85] M. Imboden and P. Mohanty, "Dissipation in nanoelectromechanical systems," *Physics Reports*, vol. 534, no. 3, pp. 89–146, Jan. 2014, ISSN: 03701573. DOI: 10.1016/j.physrep.2013.09.003.

[86] N. I. Zheludev and Y. S. Kivshar, "From metamaterials to metadevices," *Nature Materials*, vol. 11, no. 11, pp. 917–924, 2012.

[87] V. A. Fedotov, M. Rose, S. L. Prosvirnin, N. Papasimakis, and N. I. Zheludev, "Sharp trapped-mode resonances in planar metamaterials with a broken structural symmetry," *Physical Review Letters*, vol. 99, no. 14, p. 147 401, 2007.

[88] J. Zhang, K. F. MacDonald, and N. I. Zheludev, "Near-infrared trapped mode magnetic resonance in an all-dielectric metamaterial," *Optics Express*, vol. 21, no. 22, p. 26 721, 2013.

[89] Q. Zhang, E. Plum, J.-Y. Ou, H. Pi, J. Li, K. F. MacDonald, and N. I. Zheludev, "Electrogyration in metamaterials: Chirality and polarization rotatory power that depend on applied electric field," *Advanced Optical Materials*, vol. 9, no. 4, p. 2 001 826, 2020.

[90] A. Bokaian, "Natural frequencies of beams under tensile axial loads," *Journal of Sound and Vibration*, vol. 142, no. 3, pp. 481–498, 1990.

[91] A. Karvounis, B. Gholipour, K. F. MacDonald, and N. I. Zheludev, "Giant electro-optical effect through electrostriction in a nanomechanical metamaterial," *Advanced Materials*, vol. 31, no. 1, p. 1 804 801, 2018.

[92] P. X.-L. Feng, D. J. Young, and C. A. Zorman, "Mems/nems devices and applications," in *Springer Handbook of Nanotechnology*. Springer Berlin Heidelberg, 2017, pp. 395–429.

[93] D. V. Thourhout and J. Roels, "Optomechanical device actuation through the optical gradient force," *Nature Photonics*, vol. 4, no. 4, pp. 211–217, 2010.

[94] B. J. Eggleton, C. G. Poulton, P. T. Rakich, M. J. Steel, and G. Bahl, "Brillouin integrated photonics," *Nature Photonics*, vol. 13, no. 10, pp. 664–677, 2019.

[95] A. D. O'Connell, M. Hofheinz, M. Ansmann, R. C. Bialczak, M. Lenander, E. Lucero, M. Neeley, D. Sank, H. Wang, M. Weides, J. Wenner, J. M. Martinis, and A. N. Cleland, "Quantum ground state and single-phonon control of a mechanical resonator," *Nature*, vol. 464, no. 7289, pp. 697–703, 2010.

[96] J. Li, D. Papas, T. Liu, J.-Y. Ou, K. F. MacDonald, E. Plum, and N. I. Zheludev, "Thermal fluctuations of the optical properties of nanomechanical photonic metamaterials," *Advanced Optical Materials*, vol. 10, p. 2 101 591, 2022.

[97] S. Yamada, S. Schmid, T. Larsen, O. Hansen, and A. Boisen, "Photothermal infrared spectroscopy of airborne samples with mechanical string resonators," *Analytical Chemistry*, vol. 85, no. 21, pp. 10 531–10 535, 2013.

[98] L. Rayleigh, "On the magnetic rotation of light and the second law of thermodynamics," *Nature*, vol. 64, no. 1667, pp. 577–578, 1901.

[99] S. I. Vavilov and W. Lewschin, "The relation between fluorescence and phosphorescence in solid and liquid media," *Z. Phys*, vol. 35, pp. 920–936, 1926.

[100] C. Pfeiffer, C. Zhang, V. Ray, L. J. Guo, and A. Grbic, "High performance bianisotropic metasurfaces: Asymmetric transmission of light," *Physical Review Letters*, vol. 113, no. 2, p. 023 902, 2014.

[101] Y. Ling, L. Huang, W. Hong, T. Liu, Y. Sun, J. Luan, and G. Yuan, "Asymmetric optical transmission based on unidirectional excitation of surface plasmon polaritons in gradient metasurface," *Optics Express*, vol. 25, no. 12, p. 13 648, 2017.

[102] K. Chen, G. Ding, G. Hu, Z. Jin, J. Zhao, Y. Feng, T. Jiang, A. Alù, and C.-W. Qiu, "Directional janus metasurface," *Advanced Materials*, vol. 32, no. 2, p. 1 906 352, 2019.

[103] V. Savinov and N. I. Zheludev, "High-quality metamaterial dispersive grating on the facet of an optical fiber," *Applied Physics Letters*, vol. 111, no. 9, p. 091 106, 2017.

[104] Y. Yang, I. I. Kravchenko, D. P. Briggs, and J. Valentine, "All-dielectric metasurface analogue of electromagnetically induced transparency," *Nature Communications*, vol. 5, no. 1, p. 5753, 2014.

[105] C. Wu, N. Arju, G. Kelp, J. A. Fan, J. Dominguez, E. Gonzales, E. Tutuc, I. Brener, and G. Shvets, "Spectrally selective chiral silicon metasurfaces based on infrared fano resonances," *Nature Communications*, vol. 5, no. 1, p. 3892, 2014.

[106] K. Koshelev, S. Lepeshov, M. Liu, A. Bogdanov, and Y. Kivshar, "Asymmetric metasurfaces with high-q resonances governed by bound states in the continuum," *Physical Review Letters*, vol. 121, no. 19, p. 193 903, 2018.

[107] Z. Liu, Y. Xu, Y. Lin, J. Xiang, T. Feng, Q. Cao, J. Li, S. Lan, and J. Liu, "High-q quasibound states in the continuum for nonlinear metasurfaces," *Physical Review Letters*, vol. 123, no. 25, p. 253 901, 2019.

[108] N. Papasimakis, V. A. Fedotov, V. Savinov, T. A. Raybould, and N. I. Zheludev, "Electromagnetic toroidal excitations in matter and free space," *Nature Materials*, vol. 15, no. 3, pp. 263–271, Mar. 2016, ISSN: 1476-1122, 1476-4660. DOI: 10.1038/nmat4563.

[109] T. Kaelberer, V. A. Fedotov, N. Papasimakis, D. P. Tsai, and N. I. Zheludev, "Toroidal Dipolar Response in a Metamaterial," *Science*, vol. 330, no. 6010, pp. 1510–1512, Dec. 2010, ISSN: 0036-8075, 1095-9203. DOI: 10.1126/science.1197172.

[110] D. R. Smith, W. J. Padilla, D. C. Vier, S. C. Nemat-Nasser, and S. Schultz, "Composite medium with simultaneously negative permeability and permittivity," *Physical Review Letters*, vol. 84, no. 18, pp. 4184–4187, 2000.

[111] C. M. Soukoulis, S. Linden, and M. Wegener, "Negative refractive index at optical wavelengths," *Science*, vol. 315, no. 5808, pp. 47–49, 2007.

[112] L. D. Landau and E. M. Lifshitz, *Electrodynamics of Continuous Media*. Pergamon Press, 1984.

[113] R. Merlin, "Metamaterials and the landau–lifshitz permeability argument: Large permittivity begets high-frequency magnetism," *Proceedings of the National Academy of Sciences*, vol. 106, no. 6, pp. 1693–1698, 2009.

[114] D. Schurig, J. J. Mock, B. J. Justice, S. A. Cummer, J. B. Pendry, A. F. Starr, and D. R. Smith, "Metamaterial electromagnetic cloak at microwave frequencies," *Science*, vol. 314, no. 5801, pp. 977–980, 2006.

[115] C. Caloz, A. Alù, S. Tretyakov, D. Sounas, K. Achouri, and Z.-L. Deck-Léger, "Electromagnetic nonreciprocity," *Physical Review Applied*, vol. 10, no. 4, p. 047 001, 2018.

[116] N. Maccaferri, "Coupling phenomena and collective effects in resonant meta-atoms supporting both plasmonic and (opto-)magnetic functionalities: An overview on properties and applications," *Journal of the Optical Society of America B*, vol. 36, no. 7, E112–E131, 2019.

[117] J. Pendry, A. Holden, D. Robbins, and W. Stewart, "Magnetism from conductors and enhanced nonlinear phenomena," *IEEE Transactions on Microwave Theory and Techniques*, vol. 47, no. 11, pp. 2075–2084, 1999.

[118] A. I. Kuznetsov, A. E. Miroshnichenko, Y. H. Fu, J. Zhang, and B. Luk'yanchuk, "Magnetic light," *Scientific Reports*, vol. 2, no. 1, p. 492, 2012.

[119] S. Jahani and Z. Jacob, "All-dielectric metamaterials," *Nature Nanotechnology*, vol. 11, no. 1, pp. 23–36, 2016.

[120] M. Decker and I. Staude, "Resonant dielectric nanostructures: A low-loss platform for functional nanophotonics," *Journal of Optics*, vol. 18, no. 10, p. 103 001, 2016.

[121] E. E. Radescu and G. Vaman, "Toroid moments in the momentum and angular momentum loss by a radiating arbitrary source," *Physical Review E*, vol. 65, no. 3, p. 035 601, 2002.

[122] V. A. Fedotov, A. V. Rogacheva, V. Savinov, D. P. Tsai, and N. I. Zheludev, "Resonant transparency and non-trivial non-radiating excitations in toroidal metamaterials," *Scientific Reports*, vol. 3, no. 1, p. 2967, 2013.

[123] P. C. Wu, C. Y. Liao, V. Savinov, T. L. Chung, W. T. Chen, Y.-W. Huang, P. R. Wu, Y.-H. Chen, A.-Q. Liu, N. I. Zheludev, and D. P. Tsai, "Optical anapole metamaterial," *ACS Nano*, vol. 12, no. 2, pp. 1920–1927, 2018.

[124] C. Pfeiffer and A. Grbic, "Metamaterial huygens' surfaces: Tailoring wave fronts with reflectionless sheets," *Physical Review Letters*, vol. 110, no. 19, p. 197 401, 2013.

[125] X. Fang, M. L. Tseng, D. P. Tsai, and N. I. Zheludev, "Coherent excitation-selective spectroscopy of multipole resonances," *Physical Review Applied*, vol. 5, no. 1, p. 014 010, 2016.

[126] D. Smirnova and Y. S. Kivshar, "Multipolar nonlinear nanophotonics," *Optica*, vol. 3, no. 11, p. 1241, 2016.

[127] A. G. Curto, T. H. Taminiau, G. Volpe, M. P. Kreuzer, R. Quidant, and N. F. van Hulst, "Multipolar radiation of quantum emitters with nanowire optical antennas," *Nature Communications*, vol. 4, no. 1, p. 1750, 2013.